Spring 2014

Coupled computational fluid dynamics/multibody dynamics method with application to wind turbine simulations

Yuwei Li
University of Iowa

COUPLED COMPUTATIONAL FLUID DYNAMICS/MULTIBODY DYNAMICS METHOD WITH APPLICATION TO WIND TURBINE SIMULATIONS

by

Yuwei Li

A thesis submitted in partial fulfillment
of the requirements for the Doctor of
Philosophy degree in Mechanical Engineering
in the Graduate College of
The University of Iowa

May 2014

Thesis Supervisor: Associate Professor Pablo M. Carrica

Graduate College
The University of Iowa
Iowa City, Iowa

CERTIFICATE OF APPROVAL

PH.D. THESIS

This is to certify that the Ph.D. thesis of

Yuwei Li

has been approved by the Examining Committee
for the thesis requirement for the Doctor of Philosophy
degree in Mechanical Engineering at the May 2014 graduation.

Thesis Committee: _____
Pablo M. Carrica, Thesis Supervisor

_____
P. Barry Butler

_____
Andrew Kusiak

_____
Kyung K. Choi

_____
James H.J. Buchholz

_____
Bill Prescott

To my family

ACKNOWLEDGMENTS

I would like to express my greatest appreciation to my advisor, Associate Professor Pablo M. Carrica, who has been continuously supporting me throughout my Ph.D. research with his knowledge, experience, enthusiasm and patience. I am grateful to him for his time, instrumental discussions and critique. Without his guidance and persistent help this thesis would not have been possible. I would also like to thank my committee members for their time and help, Professors P. Barry Butler, Andrew Kusiak, Kyung K. Choi, James H.J. Buchholz, and Dr. Bill Prescott. The help from Dr. Prescott with the code Virtual.Lab Motion is deeply appreciated.

I would like to acknowledge the help and constructive discussions from Dr. Alejandro M. Castro and Dr. Tariq Sinokrot. Another thank-you goes to my fellow students in IIHR - Hydroscience & Engineering, who had shared their precious time with me.

I am grateful to have my beloved fiancée Dan to accompany me, who makes my life meaningful and wonderful.

I am indebted to my parents for their love and support for everything I do.

This research was supported by IAWIND under project "Tool Development for Direct Simulation of Interaction between Aerodynamic and Gearbox Loads" and the National Science Foundation under project "Simulation Based Design for Deep Water Offshore Wind Turbines Including Wave loads and Motions".

ABSTRACT

A high fidelity approach coupling the computational fluid dynamics method (CFD) and multi-body dynamics method (MBD) is presented for aero-servo-elastic wind turbine simulations. The approach uses the incompressible CFD dynamic overset code CFDShip-Iowa v4.5 to compute the aerodynamics, coupled with the MBD code Virtual.Lab Motion to predict the motion responses to the aerodynamic loads. The IEC 61400-1 ed. 3 recommended Mann wind turbulence model was implemented in this thesis into the code CFDShip-Iowa v4.5 as boundary and initial conditions, and used as the explicit wind turbulence for CFD simulations. A drivetrain model with control systems was implemented in the CFD/MBD framework for investigation of drivetrain dynamics. The tool and methodology developed in this thesis are unique, being the first time with complete wind turbine simulations including CFD of the rotor/tower aerodynamics, elastic blades, gearbox dynamics and feedback control systems in turbulent winds.

Dynamic overset CFD simulations were performed with the benchmark experiment UAE phase VI to demonstrate capabilities of the code for wind turbine aerodynamics. The complete turbine geometry was modeled, including blades and approximate geometries for hub, nacelle and tower. Unsteady Reynolds-Averaged Navier-Stokes (URANS) and Detached Eddy Simulation (DES) turbulence models were used in the simulations. Results for both variable wind speed at constant blade pitch angle and variable blade pitch angle at fixed wind speed show that the CFD predictions match the experimental data consistently well, including the general trends for power and thrust, sectional normal force coefficients and pressure coefficients at different sections along the blade.

The implemented Mann wind turbulence model was validated both theoretically and statistically by comparing the generated stationary wind turbulent field with the

theoretical one-point spectrum for the three components of the velocity fluctuations, and by comparing the expected statistics from the simulated turbulent field by CFD with the explicit wind turbulence inlet boundary from the Mann model.

The proposed coupled CFD/MBD approach was applied to the conceptual NREL 5MW offshore wind turbine. Extensive simulations were performed in an increasing level of complexity to investigate the aerodynamic predictions, turbine performance, elastic blades, wind shear and atmospheric wind turbulence. Comparisons against the publicly available OC3 simulation results show good agreements between the CFD/MBD approach and the OC3 participants in time and frequency domains. Wind turbulence/turbine interaction was examined for the wake flow to analyze the influence of turbulent wind on wake diffusion.

The Gearbox Reliability Collaborative project gearbox was up-scaled in size and added to the NREL 5MW turbine with the purpose of demonstrating drivetrain dynamics. Generator torque and blade pitch controllers were implemented to simulate realistic operational conditions of commercial wind turbines. Interactions between wind turbulence, rotor aerodynamics, elastic blades, drivetrain dynamics at the gear-level and servo-control dynamics were studied, showing the potential of the methodology to study complex aerodynamic/mechanic systems.

TABLE OF CONTENTS

LIST OF TABLES

Table

LIST OF FIGURES

Figure

CHAPTER 1

INTRODUCTION

1.1 Overview

Wind energy has shown great potential and increased deployment over the past decades to become major source of electric energy. The generation potential of wind power on land and near off-shore is estimated at 72 TW, over five times the world's current power use in all forms (Archer and Jacobson 2005). The newly installed capacity for global wind power in 2012 was reported at nearly 45 GW with an investment of about € 56 billion, an annual growth of about 10%, while the cumulative was 282.5 GW of installed wind power globally at the end of 2012. It is projected that the total installed capacity by the end of 2017 will be about 536 GW (Global Wind Energy Council 2013).

Current design trends favor larger turbines, which tend to be more cost-effective. However, this results in more complex turbine systems with more demanding structural constraints. These large turbines, with rotor areas equivalent to 3 to 4 football fields, expose the wind turbine to high wind shear and turbulence. The long and slender blades are subject to large amplitude changes in wind loads, causing reliability issues due to fatigue. Variable-speed, variable-pitch and yaw control are needed for the turbine system to achieve best performance. High tip speeds due to the long blades introduce noise and environmental impacts. Challenges increase when several wind turbines are operated as wind farms, with stronger velocity gradients and fluctuations caused by momentum deficits and wake turbulence of upwind turbines. The above-mentioned issues tend to be relieved when operating offshore, where the turbines are exposed to higher, more constant wind speeds and less turbulence. However, other problems arise, including waves and platform stability.

Maintenance cost is another critical factor influencing wind turbine design, especially for offshore farms with expensive accessibility. Of all components in a turbine,

gearbox, drive train and generator contribute most to downtime, while rotor hub and blades are the next critical factors (Faulstich et al. 2008; Spinato et al. 2009). Wind gust and turbulence are critical factors for gearbox failure, leading to shaft misalignment of the drivetrain and non-torque loads of the internal gear components.

Development of methodologies and techniques capable of modeling the interaction between realistic wind loads and the structural components is the most promising way to improve designs that will better perform in complex operational environments. This thesis is a first attempt to develop a tool combining aerodynamics, elasticity, drivetrain dynamics and wind simulations.

1.2 Literature Review of Aerodynamics Methods

Methods of various levels of complexity have been developed to predict the aerodynamic behavior of a wind turbine rotor.

Being computationally cheap and highly efficient, blade element momentum methods (BEM) have been very popular for engineering design, provided that good airfoil data are available for lift and drag coefficients as a function of angle of attack and Reynolds number (Glauert 1963). Several models were developed based on BEM and their performance was improved by introducing new models as accounting for dynamic stall, dynamic wake, and tip losses (Snel and Schepers 1993; Leishman and Beddoes 1989; Shen et al. 2005). However, BEM models are greatly influenced by the choice of airfoil data and dependent on empirical corrections, limiting their use, especially for off-design conditions.

To obtain more physical details and still retain high computational efficiency, 3D inviscid aerodynamic models were introduced, including lifting line (Whale et al. 1999), panel methods (Hess 1975), vortex lattice methods (Landahl and Stark 1968), and Boundary Integral Equation (BIEM) (Preuss et al. 1980) methods. Though airfoil

coefficients are not needed in these methods, issues arise because potential flow methods cannot handle viscous effects and separation.

The next level of complexity is to solve the Reynolds-Averaged Navier-Stokes (RANS) equations with some turbulence model. The Baldwin-Lomax zero equation model (Baldwin and Lomax 1978) and the two-equation $k-\varepsilon$ model (Launder and Spalding 1974) are popular regardless of their problems in reproducing the stall characteristics of airfoils and rotor blades (Haase 1997). The $k-\omega/\,k-\varepsilon$ SST model (Menter 1994) is widely used for wind turbine simulations (Sørensen et al. 2002) for its capability in simulating attached and lightly separated airfoil flows. For massive separated flows, it is better to use the more advanced and costly Detached Eddy Simulation (DES) approach that combines large eddy simulation (LES) in the separated regions and RANS inside boundary layers. This gives DES the ability to better resolve flow separation and the stall of an airfoil (Johansen et al. 2002). Though the cost of these approaches is significantly higher than any of the previously mentioned simpler methods, advances in computer technology are making possible to handle large, dynamic problems with parallel platforms.

Several authors have performed CFD computations of wind turbines with a variety of methods. The generalized actuator disc method combines the BEM method and the Navier-Stokes (N-S) equations, representing the blade geometries by surface forces that act upon the incoming flow. This method has been applied to study turbines (Mikkelsen 2003), turbine wakes (Sørensen et al. 1998; Ivanell et al. 2007) and wind farms (Sørensen et al. 2007). The method was improved by the more sophisticated actuator line (Sørensen and Shen 2002) and actuator surface (Shen et al. 2007, 2009) approaches. On the other hand, some researchers directly modeled the rotor by constructing body-fitted grids. Sezer-Uzol and Long (2006) computed the NREL Phase VI turbine at different wind speeds and yaw angles using the finite volume flow solver PUMA2 with rotating unstructured tetrahedral grids, showing good agreement with

experiments, but the inviscid nature of the code resulted in limited ability to predict situations where massive flow separation occurs. Potsdam and Mavriplis (2009) used the unstructured multi-grid RANS code NSU3D to predict the aerodynamics of an isolated wind turbine rotor, and the results were compared with both experiments and predictions with the code Overflow. Sørensen et al. (2002) studied 3-D aerodynamic effects as a function of wind speeds using the multi-block, finite volume, incompressible RANS flow solver EllipSys3D with a rotor-only configuration. Good qualitative and quantitative agreement with experimental measurements evidenced the advantages of CFD approaches for wind turbine simulations. Duque et al. (2003) performed computations of the NREL Phase VI turbine with the NASA compressible RANS flow solver Overflow-D, based on a finite differences approach and overset grid (Buning et al. 1991). The authors compared the results of Overflow-D and the lifting line code CAMRAD II with the experiments, and extensively discussed the aerodynamic performance of the wind turbine. Hsu et al. (2013) used a finite element based Arbitrary-Lagrange-Eulerian (ALE) method CFD code to simulate the NREL Phase VI wind turbine in a wide range of wind velocities with rotor-only configuration, and the full wind turbine through sliding-interface method. Bazilevs et al. (2011) studied the rotor of the NREL 5 MW baseline wind turbine using both a finite element approach and a NURB-based (Non-Uniform Rational B-splines) approach for the geometry, which has the potential for coupled aerodynamic/structural analysis.

1.3 Literature Review of Elasticity Methods

There are three main approaches for structural modeling of wind turbines: modal shape functions, finite element methods (FEM) and multi-body dynamics simulation (MBD). All these approaches use loads from aerodynamic computations to predict the elastic response.

The modal shape functions approach with generalized coordinates is widely used for structural modeling due to computational efficiency and good approximation of the responses of the system in low frequencies. These are achieved by reducing the system's degrees-of-freedom (DOF) to a relatively small number and using the linear combination of a few but physically realistic basic functions that correspond to the eigenmodes with the lowest eigenfrequencies. Øye (1996) simulated a turbine with the commercially available and widely used aero-elastic simulation tool FLEX with only the first 3 or 4 eigenmodes of the blades, and the results were in good agreement with measurements.

The more advanced but computationally expensive FEM approach is widely adopted by aero-elastic code developers (Schepers et al. 2002), as FEM allows for more complex blade deformations, which are common for large-scale wind turbines. The long and slender blade justifies the use of beam theory in the structural modeling, with the classic beam theory for small deformations or second-order non-linear beam theory for large deformations. Petersen (1996) developed an aero-elastic code (HAWC) based on FEM with the Timoshenko beam element. Simulation results were in good agreement with measurements of the three-bladed, stall regulated 500 KW NTK-500/37 wind turbine. Fuglsang et al. (2002) applied the Risø research code HAWC for the BONUS 1 MW wind turbine and the ECN research code PHATAS (Lindenburg and Schepers 1996) for the WM 600 wind turbine with the site-specific consideration as to find the optimization of minimal cost of energy.

The interaction dynamics between components of the turbine system in large-scale become important. This involves different body motions for each component of the turbine system, in which the components are combined with connections where loads and displacements are communicated from one component to the other (Hansen et al. 2006). The multi-body dynamics simulation approach (Pfeiffer 1996; Bauchau 1998; Bauchau and Hodges 1999) is thus adopted by most of the simulation tools for comprehensive wind turbine analysis, including FAST, ADAMS, Bladed Multibody and HAWC2 from

the first international project "Offshore Code Comparison Collaboration" (OC3) (Jonkman and Musial 2010) dedicated to verification of simulation tools for wind turbines.

The MBD approach has been applied and improved for wind turbine simulations in a variety of fields. Lee et al. (2002) conducted a structural dynamic analysis of a two-bladed horizontal axis wind turbine accounting for flexible blades, tower, yaw and teetering using both rigid-body and flexible-body representations, in which the flexible-body was modeled with a non-linear beam finite element, showing a simple, efficient and accurate modeling for the dynamic characteristics of the turbine system. Larsen et al. (2005) applied the MBD-based code HAWC2 to investigate the effects of tower dynamics, hydrodynamics and nonlinear soil properties to a typical 2 MW offshore turbine mounting on a monopile foundation in terms of the changes in frequency, mode shapes and damping. Heege et al. (2007) applied the non-linear FEM in the multi-body system through a mixed variational formulation to evaluate the fatigue loads of the wind turbine power trains.

1.4 Literature Review of Aero-elastic Coupling

Computation of the structural responses of a wind turbine system depends on the aerodynamic loads, which are also dependent on the structural dynamics, resulting in a strong aero-elastic coupling.

Coupling BEM and MBD perhaps is the most widely adopted approach for wind turbine aero-elastic simulations to date, allowing efficient and good predictions for rotor aerodynamics and non-linear structural responses. These include the two primary design codes applied by the U.S. wind industry, AeroDyn/FAST and AeroDyn/ADAMS. Passon et al. (2007) presents benchmark simulations with the NREL 5MW offshore wind turbine within OC3 project. Comparison for the simulation results in general agrees well for both the aerodynamic performance and blade deflection. However, limits from the

aerodynamic predictions restrict the accuracy of BEM/MBD applications. CFD is a more advanced aerodynamic predictor and provides a better solution, with less modeled inputs and the ability to predict the turbine wake.

Most efforts to couple CFD and computational structural dynamics (CSD) solvers have been reported in the rotorcraft community. Examples are the coupled overset CFD solver Overflow-D and the flexible multi-body dynamics code DYMORE (Bauchau et al. 2001), and coupled unsteady RANS unstructured grid solver FUN3D and the rotorcraft computational structural dynamics code CAMRAD II (Biedron and Lee-Rausch 2008), showing computations over wide range of flight conditions. However, only limited research has been reported to date with CFD/CSD coupling for wind turbine simulations. Bazilevs et al. (2011) proposed a fluid-structure interaction (FSI) procedure for wind turbine simulations using a FEM based CFD solver and a structural solver based on the isogeometric rotation-free Kirchohoff-Love composite shell and the bending strip method. The coupled approach was applied to both rotor-only (Bazilevs et al. 2012) and the full turbine configuration including tower and nacelle (Hsu and Bazilevs 2012) for the NREL 5MW baseline wind turbine, showing a good combination of accuracy and efficiency.

1.5 Literature Review of Atmospheric Wind Turbulence

Wind turbines are often exposed to complex wind conditions in which atmospheric wind turbulence dominates, causing critical issues of large blade deformations and loadings. A realistic transient turbulent wind field is important for wind turbine simulations.

In general, the most "correct" and accurate way to simulate the turbulent field is to solve the Navier-Stokes equations directly by Direct Numerical Simulations (DNS) to resolve the turbulent fluctuations. However, the computational cost is enormously expensive and not possible for engineering application at this moment due to the large

span of turbulent scales. Another accurate but less expensive method is Large Eddy Simulation (LES), which is an approximate solution to the N-S equations where the smallest scales are not solved directly but modeled (Smirnov et al. 2001; Klein et al. 2003). One advanced atmospheric turbulent model was proposed by Bechmann (2006). Based on LES and incorporated in the CFD code EllipSys3D, the model provides improved representation of the anisotropy of the atmospheric turbulence. Yet, LES still requires large computational resources and is not yet practical for engineering use.

Currently the most adopted models for wind turbulence simulations are based on the construction of spectral tensors such as the Sandia model (Veers 1988) and the Mann wind turbulence model (Mann 1994, 1998). Mann's model is capable of simulating all three velocity components of a 3D incompressible turbulence field. Most of the aerodynamic codes capable of including wind turbulence are based on BEM, and thus interaction between wind turbines and the turbulent field cannot be predicted. In this respect, CFD provides a good methodology to simulate turbulence/turbine interaction.

Most CFD applications focus on the generation of the wind turbulent field without the turbine. To the author's best knowledge, the only research work reported for CFD simulations of a resolved wind turbine in wind turbulence was performed by Troldborg et al. (2007), who used Mann's model. The turbulent velocity field was introduced via body forces in the momentum equation. However, the presence of the turbine was modeled using the actuator line method, and therefore the geometry of the turbine was not considered.

1.6 Objectives and Approach

The main objective of this thesis is to develop a simulation tool capable of accurately predicting the aero-servo-elastic behavior of wind turbines under complex operational environments, including realistic transient wind turbulence and wind shear, and dynamics of the rotor-shaft-gearbox-generator.

This is made possible by a high fidelity approach that couples an overset dynamics CFD solver to predict the aerodynamics of the turbine in motion, and a MBD solver to predict the motions of the turbine system under the aerodynamic loads.

The incompressible CFD code CFDShip-Iowa v4.5 is used as the flow solver. CFDShip-Iowa v4.5 is a finite difference, unsteady Reynolds-Averaged Navier-Stokes (URANS) or Detached Eddy Simulation (DES) solver. It uses structured multi-block grids and body-fitted curvilinear grids with overset capabilities to accommodate complex geometries and motions. The IEC 61400-1 ed. 3 recommended Mann wind turbulence model is used as to add explicit turbulence, and was implemented in this thesis into the code as inlet boundary and initial conditions.

The multi-body dynamics simulation (MBD) code Virtual.Lab Motion from LMS International is used as the motion solver. Virtual.Lab Motion is based on a generalized Cartesian coordinate system and Euler parameters to formulate the equations of motion. The code has the capability to simulate realistic motions of complex mechanical system such as vehicles and powertrains.

1.7 Outline

The structure of this thesis is organized as follows:

In chapter 2, methodologies used by the MBD code Virtual.Lab Motion and the overset CFD code CFDShip-Iowa v4.5 are discussed in detail. The coupling strategy is then introduced, including the proposed solutions for non-matching discretization and computational time step between the two codes. Finally, a section is dedicated to explain the mathematical theory and implementation of the Mann wind turbulence model for CFD simulations.

In chapter 3, simulations of the 2-bladed stall-regulated onshore wind turbine NREL Phase VI using the overset CFD code are presented. The simulations are performed in an inertial frame of reference with the rotor consisting of the blades and

hub. The geometry of the tower and nacelle are approximate but included in the computation. Extensive comparisons against the experimental results were conducted to validate the capabilities of the code for aerodynamic predictions.

In chapter 4, the proposed coupled approach for wind turbine aero-elastic simulations was applied to the conceptual NREL 5MW offshore wind turbine. Simulations were performed with incremental levels of complexity to properly validate the capabilities of the approach for aero-elastic predictions of the turbine with rigid and flexible blades operating with or without atmospheric wind turbulence.

In chapter 5, dynamic modeling of wind turbine with drivetrain was investigated by introducing a drivetrain model with 3 levels of complexity. This allows for the implementation of wind turbine control systems and provides insight of the drivetrain dynamics at the gear-level for the turbine in turbulent winds with flexible blades, making it a promising and unique tool for wind turbine design and application.

Finally, chapter 6 summarizes the conclusions and proposes future work.

CHAPTER 2

COMPUTATIONAL METHODS

In this chapter, details for the structural solver, flow solver, coupling of the flow and structural solver, as well as the explicit wind turbulence model are discussed in order, covering their mathematical foundations and numerical implementations.

2.1 Structural Solver

The multi-body dynamics simulation (MBD) code Virtual.Lab Motion (Prescott 1999; LMS International 2013), from LMS international, is used in simulating the structural dynamics for the turbine. Virtual.Lab Motion uses a set of generalized coordinates that are based on a generalized Cartesian coordinate system (X, Y, Z) and Euler parameters (e_0, e_1, e_2, e_3) to formulate the equations of motion (Haug 1989). The multi-body system consists of interconnected bodies that can be rigid or flexible, each of which may have translational and rotational displacements. The bodies are connected by force and joint elements that describe their dynamic and kinematic constraints. The code has the capability to simulate realistic motions of complex mechanical system such as vehicles and powertrains.

2.1.1 Governing Equations

The motion of constrained bodies in the MBD code are described by a set of differential-algebraic equations (DAEs) that consist of the differential equations of motion and a set of algebraic constraint equations

$$\boldsymbol{\phi}(\mathbf{q}, \mathrm{t}) = 0 \tag{2.1}$$

$$\boldsymbol{M}^i \ddot{\mathbf{q}}^i + \boldsymbol{\phi}_{\boldsymbol{q}_i}^T \boldsymbol{\lambda} = \boldsymbol{Q}_v^i + \boldsymbol{Q}_e^i \tag{2.2}$$

where $\mathbf{q} = [\mathbf{q}^1\ \mathbf{q}^2 \ldots \mathbf{q}^n]^T$ is the vector of the generalized coordinates that consists of the translational and rotational coordinates of each body in the system measured in the global frame and n is the number of bodies in the system. $\boldsymbol{\phi}$ is a set of kinematic constraints,

$\boldsymbol{\phi}_{q_i}^T$ is the Jacobian of the vector of constraints $\boldsymbol{\phi}$ with respect to the generalized coordinates of body i, and $\boldsymbol{\lambda}$ is the vector of the Lagrange multipliers for the constraints. $\boldsymbol{M}^i$ is the mass matrix of the body i, $\boldsymbol{Q}_v^i$ is the quadratic velocity vector used to describe Coriolis and centrifugal terms, obtained by the partial derivatives of the kinetic energy of the body with respect to time t and the generalized coordinates $\mathbf{q}$; $\boldsymbol{Q}_e^i$ is the vector of the external forces applied on the body i.

In order to solve the set of DAEs (Eqs. (2.1) and (2.2)), Eq. (2.1) is modified by taking the second partial derivative with respect to time t

$$\boldsymbol{\phi}_{\boldsymbol{q}}\ddot{\boldsymbol{q}} = -\boldsymbol{\phi}_{tt} - \left(\boldsymbol{\phi}_{\boldsymbol{q}}\dot{\boldsymbol{q}}\right)_{\boldsymbol{q}}\dot{\boldsymbol{q}} - 2\boldsymbol{\phi}_{\boldsymbol{q}t}\dot{\boldsymbol{q}} = \gamma \tag{2.3}$$

where subscript $\boldsymbol{q}$ and t denote their partial derivative, respectively.

The DAEs can then be written in matrix form by combining Eqs. (2.2) and (2.3) as

$$\begin{bmatrix} \boldsymbol{M} & \boldsymbol{\phi}_{\boldsymbol{q}}^T \\ \boldsymbol{\phi}_{\boldsymbol{q}} & 0 \end{bmatrix} \begin{bmatrix} \ddot{\boldsymbol{q}} \\ \boldsymbol{\lambda} \end{bmatrix} = \begin{bmatrix} \boldsymbol{Q}_v + \boldsymbol{Q}_e \\ \gamma \end{bmatrix} \tag{2.4}$$

where $\boldsymbol{Q}_e$ contains the external loads and is where the wind loads are added.

2.1.2 Numerical Methods

A numerical integration method is used to solve the DAEs for the generalized accelerations $\ddot{\boldsymbol{q}}$ and Lagrange multipliers $\boldsymbol{\lambda}$, and the generalized velocities and coordinates of the system are then obtained by integration of the accelerations forwards in time (Prescott 1999). Results are expressed in terms of a set of position, velocity, acceleration and reaction forces for each body in the system. Both explicit and implicit integrations can be performed, where the explicit integrator is based on the Adams-Bashforth-Moulton method (Shampine and Gordon 1975) and the implicit integrator is based on backward-difference formula (Brenan et al. 1989).

2.2 Flow Solver

The incompressible CFD code CFDShip-Iowa v4.5 is used as the flow solver for the turbine simulations. CFDShip-Iowa v4.5 is a finite difference, unsteady Reynolds-Averaged Navier-Stokes (URANS) or Detached Eddy Simulation (DES) solver. It uses structured multi-block grids and body-fitted curvilinear grids with overset capabilities to accommodate complex geometries and motions. Both single-phase and two-phase (air/water) flow problems can be considered. The air/water problem is addressed by using a semi-coupled method (Huang et al. 2008) where the water flow is decoupled from the air solution, but the air flow uses the unsteady water flow as an moving immersed boundary condition, providing an excellent approximation to the airflow and forces on large-scale objects like ships or floating structures. The free surface is modeled with an unsteady single-phase level set capturing approach (Carrica et al. 2007), where only the water flow is solved with enforced kinematic and dynamic free surface boundary conditions on the interfaces, allowing robust computations and large amplitude and/or steep waves. Dynamic overset grid method is used to resolve grid deformations and relative motions (Carrica et al. 2007), with the interpolation coefficients between the grids recomputed dynamically at run time with the code Suggar (Noack 2005). Large-scale computations are achieved using high performance computing (HPC) with a MPI-based domain decomposition approach (Carrica et al. 2010). The code has capabilities for full six degree of freedom (6 DOF) and a parent/child hierarchy of objects that allows motion of control surfaces and other appendages.

2.2.1 Governing Equations

All variables and properties are non-dimensionalized by the characteristic length L and velocity U_0 of interest, and the liquid properties. For wind turbine simulations, they are chosen as the rotor radius and the prevailing incoming wind velocity.

The dimensionless mass momentum and continuity equations for incompressible flows are written as (symbols in bold font represent vector variables)

$$\frac{\partial \boldsymbol{u}}{\partial t} + \nabla \cdot [(\boldsymbol{u} - \dot{\boldsymbol{x}}) \otimes \boldsymbol{u}] = -\nabla p + \nabla \cdot \left[\frac{1}{Re_{eff}} (\nabla \boldsymbol{u} + \nabla \boldsymbol{u}^T) \right] + \boldsymbol{S} \tag{2.5}$$

$$\nabla \cdot \boldsymbol{u} = 0 \tag{2.6}$$

where $\boldsymbol{u}$ is the fluid velocity, $\dot{\boldsymbol{x}}$ is the grid velocity to account for moving or deforming grids, $\otimes$ denotes dyadic product, and $\mathbf{S}$ is a source term due to body forces, e.g. a propeller model, and is zero in this thesis for wind turbine simulations; p is the dimensionless piezometric pressure, $p = p_{abs}/\rho U_0^2 + z/Fr^2 + 2k/3$ with p_{abs} the absolute pressure; $Fr = U_0/\sqrt{gL}$ is the Froude number; Re_{eff} is the effective Reynolds number, defined as $Re_{eff}^{-1} = Re^{-1} + \nu_t$; $Re = \rho_l U_0 L/\mu_l$ is the Reynolds number for water ($l = w$) or air ($l = a$); k and ν_t are the turbulent kinetic energy and turbulent eddy viscosity, respectively, obtained from the turbulence model.

2.2.2 Turbulence Models

A delayed detached eddy simulation (DDES) model (Gritskevich et al. 2011) based on Menter's shear stress transport model (SST) (Menter 1994), was used to model the turbulence, with governing equations for the turbulent kinetic energy k and the specific dissipation rate ω

$$\partial \rho k/\partial t + \nabla \cdot \left((\boldsymbol{u} - \dot{\boldsymbol{x}}) \rho k \right) = P_k - \rho k^{3/2}/l_{DDES} + \nabla \cdot ((\mu + \sigma_k \mu_t) \nabla k) \tag{2.7}$$

$$\partial \rho \omega/\partial t + \nabla \cdot \left((\boldsymbol{u} - \dot{\boldsymbol{x}}) \rho \omega \right) = \alpha \rho P_k/\mu_t - \beta \rho \omega^2 + \nabla \cdot \left((\mu + \sigma_\omega \mu_t) \nabla \omega \right) + 2(1 - F_1) \rho \sigma_{\omega 2} \nabla k \cdot \nabla \omega/\omega \tag{2.8}$$

$$\mu_t = \rho\, a_1 k/\max(a_1 \omega, F_2 S) \tag{2.9}$$

where $P_k = \min(\mu_t S^2, 10\beta^* \rho \omega k)$, $S = \sqrt{2 S_{ij} S_{ij}}$ is the strain rate magnitude, $S_{ij} = {}^1/_2 \left(\partial u_i/\partial x_j + \partial u_j/\partial x_i \right)$, μ_t is the turbulent dynamic viscosity, ρ is the fluid density, and μ is the molecular dynamic viscosity. The length scales of the model are $l_{DDES} = l_{RANS} - f_d \max(0, l_{RANS} - l_{LES})$, $l_{RANS} = \sqrt{k}/(\beta^* \omega)$ and $l_{LES} = C_{DES} \Delta$. The DES

constant is computed from $C_{DES} = C_{DES1}F_1 + C_{DES2}(1 - F_1)$, with $C_{DES1} = 0.78$ and $C_{DES2} = 0.61$, and Δ is the grid length scale, taken as the maximum cell side length. F_1 and F_2 are the SST blending functions, and f_d is an empiric blending function as

$$F_1 = tanh\left[\left(min\left(max\left(\frac{\sqrt{k}}{0.09\omega\delta}, \frac{1}{Re}\frac{500}{\delta^2\omega}\right), \frac{4\sigma_{\omega 2}k}{CD_{k\omega}\delta^2}\right)\right)^4\right] \tag{2.10}$$

$$F_2 = tanh\left[\left(max\left(\frac{2\sqrt{k}}{0.09\omega\delta}, \frac{1}{Re}\frac{500}{\delta^2\omega}\right)^2\right)\right] \tag{2.11}$$

$$f_d = 1 - tanh((C_{d1}r_d)^{C_{d2}}), r_d = \frac{\mu_t + \mu}{\rho\kappa^2 d_w^2\sqrt{0.5(S^2+\Omega^2)}} \tag{2.12}$$

where δ is the distance to the nearest no slip surface and $CD_{k\omega} = \max(2\sigma_{\omega 2}\nabla k \cdot \nabla\omega/\omega; 10^{-20})$. $\Omega = \sqrt{2W_{ij}W_{ij}}$ is the vorticity magnitude, $W_{ij} = {}^1/_2\,(\partial u_i/\partial x_j - \partial u_j/\partial x_i)$ is the rigid rotational component of the velocity gradient. In Eq. (2.12) the constants are $C_{d1} = 20$, $C_{d2} = 3$, $\kappa = 0.41$.

The model constants are $a_1 = 0.31$, $\beta^* = 0.09$, $\alpha_1 = 5/9$, $\beta_1 = 0.075$, $\sigma_{k_1} = 0.85$, $\sigma_{\omega_1} = 0.5$, $\alpha_2 = 0.44$, $\beta_2 = 0.0828$, $\sigma_{k_2} = 1$ and $\sigma_{\omega_2} = 0.856$. α, β, σ_k, σ_ω are computed with the blending function F_1 as $\alpha = \alpha_1 F_1 + \alpha_2(1 - F_1)$, and similarly for the other constants.

2.2.3 Free Surface Modeling

The free surface is modeled with an unsteady single-phase level set approach (Carrica et al. 2007), with the function ϕ defined as the distance to the interface, positive in water and negative in air. The location of the free surface is thus given by the zero level set of the function ϕ. The transport equation for ϕ with no mass interfacial transfer is

$$\frac{\partial\phi}{\partial t} + \boldsymbol{u}\cdot\nabla\phi = 0 \tag{2.13}$$

The kinematic and dynamic free surface boundary conditions are enforced on the interfaces as

$$\nabla \boldsymbol{u} \cdot \boldsymbol{n} = 0 \tag{2.14}$$

$$p_{int} = z_{int}/Fr^2 \tag{2.15}$$

where $\boldsymbol{n} = -\nabla\phi/|\nabla\phi|$ is the unit normal vector on the free surface from water into air, p_{int} and z_{int} are the pressure and surface location at the interface, respectively.

2.2.4 Numerical Methods

To accommodate modeling of complex geometries, a coordinate transformation is performed from the physical domain in Cartesian coordinates (x, y, z, t) to the computational domain in non-orthogonal curvilinear coordinates (ξ, η, ζ, τ) (Thompson et al. 1985). Eqs. (2.5), (2.6), (2.7), (2.8) and (2.13) are re-written in the transformed domain as

$$\frac{\partial u_i}{\partial \tau} + \frac{1}{J} b_j^k \left(u_j - \frac{\partial x_j}{\partial \tau}\right) \frac{\partial u_i}{\partial \xi^k} = -\frac{1}{J} b_i^k \frac{\partial p}{\partial \xi^k} + \frac{1}{J} \frac{\partial}{\partial \xi^j} \left(\frac{1}{J} \frac{b_i^j b_i^k}{Re_{eff}} \frac{\partial u_i}{\partial \xi^k}\right) + \left(\frac{1}{J} b_j^k \frac{\partial v_t}{\partial \xi^k}\right) \left(\frac{1}{J} b_i^l \frac{\partial u_j}{\partial \xi^l}\right) + s_i \tag{2.16}$$

$$\frac{1}{J} \frac{\partial}{\partial \xi^j} \left(b_i^j u_i\right) = 0 \tag{2.17}$$

$$\rho \left(\frac{\partial k}{\partial \tau} + \frac{1}{J} b_j^k \left(u_j - \frac{\partial x_j}{\partial \tau}\right) \frac{\partial k}{\partial \xi^j}\right) = \frac{1}{J} \frac{\partial}{\partial \xi^j} \left(\frac{1}{J} (\mu + \sigma_k \mu_t) b_i^j b_i^k \frac{\partial k}{\partial \xi^k}\right) + P_k - \rho k^{3/2}/l_{DDES} \tag{2.18}$$

$$\rho \left(\frac{\partial \omega}{\partial \tau} + \frac{1}{J} b_j^k \left(u_j - \frac{\partial x_j}{\partial \tau}\right) \frac{\partial \omega}{\partial \xi^j}\right) = \frac{1}{J} \frac{\partial}{\partial \xi^j} \left(\frac{1}{J} (\mu + \sigma_\omega \mu_t) b_i^j b_i^k \frac{\partial \omega}{\partial \xi^k}\right) + \alpha \rho P_k/\mu_t - \beta \rho \omega^2 + 2(1 - F_1) \rho \sigma_{\omega 2} \left(\frac{1}{J} b_j^k \frac{\partial k}{\partial \xi^j} \cdot \frac{1}{J} b_j^k \frac{\partial \omega}{\partial \xi^j}\right)/\omega \tag{2.19}$$

$$\frac{\partial \phi_i}{\partial \tau} + \frac{1}{J} b_j^k \left(u_j - \frac{\partial x_j}{\partial \tau}\right) \frac{\partial \phi_i}{\partial \xi^k} = 0 \tag{2.20}$$

where J and b_i^j are Jacobian and matrices of the transformation. A convective term $b_j^k \frac{\partial x_j}{\partial \tau} \frac{\partial u_i}{\partial \xi^k}$ due to the grid velocity is introduced to account for moving or deforming grids.

A finite differences scheme is used to discretize the equations with second-order implicit Euler scheme for temporal terms. For the spatial discretization, the convective terms are discretized with second-order upwind for RANS or fourth-order upwind biased for DES and delayed DES; second-order centered scheme is used for the viscous terms.

The incompressibility is enforced by a strong pressure/velocity coupling, achieved using either the pressure implicit with splitting of operators (PISO) or projection algorithms.

The overall solution strategy for the flow problems is performed with non-linear iterations at each time step to properly couple the turbulence, level set function, non-linear convective terms in the momentum equations, and the motions of the object. Overset connectivity information for the grids is updated by Suggar at run time based on the latest deformations and motions of the grids provided by the flow solver. After reading the overset information, the flow solver begins to solve for the $k-\omega$ equations implicitly and compute the turbulent viscosity. Then level set function is solved and reinitialized sequentially. With the updated turbulent viscosity and free surface, the momentum equations are solved implicitly and a Poisson equation for the pressure is then constructed and solved to enforce continuity. Forces and moments can then be computed from the flow field solutions, and motions of the objects will be obtained either with the 6-DOF solver included in CFDShip-Iowa v4.5 or the structural solver as the one discussed in this thesis. If the global residuals are within the set acceptable tolerances, the process proceeds to next time step. Otherwise a new non-linear iteration for the current time step will be executed with the corrected motions until convergence is reached.

2.3 Coupling Strategy

The coupled aero-elastic approach is done by exchanging the necessary information between the CFD and the MBD codes at run time. The forces and moments computed by the CFD code are sent to the MBD code as $\boldsymbol{Q}_e^i$ for each body in Eq. (2.2), and the positions/rotations obtained by the MBD code are sent to the CFD code and used to move the CFD grids to recompute the convective term and solid boundary conditions.

Figure 2.1 schematically describes the approach for discretization. Blades and tower are slender and thus can be well approximated by flexible one-dimensional structures. The system is discretized into interconnected bodies and represented in the

MBD code by their generalized coordinates at the center of gravity (CG) with proper position and orientation. The interconnection between bodies is described and constrained by bracket joints for rigid turbine simulations that allow no motions between two bodies, and beam force elements for flexible turbine simulations that allow 6 DOF for each body. Since the CFD grids are much finer than the discretization in the MBD code, special treatment was done to accommodate the information exchange for this non-matching domain discretization, as shown in Fig. 2.1. The CFD grids used to discretize the geometry (blades, tower, etc.) consist of a body-fitted surface grid attached to solid surfaces, and extend into the volume of the fluid to resolve the flow field. Each grid cell is assigned a set of integer IDs that are associated with the bodies it belongs to. As an example, a cell may have ID values *i* and *i-1* indicating that some part of the cell is associated with body *i* and another part with body *i-1*. Integration of the forces and moments for each cell on the surface grid is performed with respect to the CG of the corresponding body to obtain the forces and moments contributing to each body, as needed by the MBD code. To integrate the forces and moments correctly, weights of the contribution for each cell to its associated body are estimated based on the fraction of cell area belonging to that body. The MBD code provides the motions for each body in terms of 3 global positions and the rotational matrix with respect to its initial configuration. Due to issues to be discussed later in this section, positions/rotations from more than one body will be applied to the cell even if the cell is only associated with one body.

Figure 2.2 shows a flow chart depicting the strategy to couple the CFD code and the MBD code. The coupling between structure and fluid is made in explicit form. This is adequate for the case of a wind turbine since the added mass due to flow acceleration by the motion of the structure is negligible compared to the mass of the blades, tower and other moving components.

Communication and exchange of the forces and moments computed from the CFD code and the positions/rotations computed from the MBD code are needed so each

program has the necessary information to perform its computations. Communication is made through two communication files, one for forces and moments, and one for positions and rotations, so that the CFD code writes the appropriate forces and moments that the MBD code needs to perform the multi-body dynamic computations, and the MBD code writes the computed positions and rotations resulting from the input forces and moments. During the initialization stage, the CFD code reads and splits the grids according to user directives for parallel decomposition, while the MBD code reads the information of the system model that includes mass, position and orientation of each body, structural properties and kinematic constraints of the system's components. Then the CFD code sends the initial forces and moments to the MBD code, zero for a simulation starting from scratch or the values from a specific restart solution for a restart run. Afterwards, the two codes begin their independent computations until the time for communication specified by the user. For both codes non-linear iterations are needed, due to the nonlinear nature of the equations of motion of the constrained multi-body system and the fluid flow. The CFD code obtains the overset domain-connectivity-information (DCI) from Suggar at run time, and then non-linear iterations are performed to properly couple turbulence, level set, non-linear convection terms of the momentum equations, and motions. Forces and moments are computed after the pressure implicit split operator (PISO) loop to obtain solenoidal velocity field. When the computations reach the communication time, positions/rotations are sent by the MBD code to the CFD code which deforms the grids and obtains the new DCI for the next time step, while the updated forces and moments are sent to the MBD code to compute the new motion responses. The MBD code is much faster than the CFD code, thus MBD code shares one processor with the CFD code with no significant performance penalty.

Some important issues need to be addressed for a successful coupling of the CFD and MBD codes. One is related to the implementation of the positions provided by the MBD code into the CFD grids. Since the MBD model is composed by rigid bodies

connected by flexible beam connections, direct implementation of the body positions into the CFD grids can (and will) cause a collapse of the surface grids as the bodies partially overlap each other on moderate or large deformations. To prevent this unphysical behavior, the new position of the surface grid point is obtained by a weighted average of the positions of the two bodies whose CG's bound the grid point. Since the CG's behave physically and do not collapse, the new grid obtained with this interpolation process is well behaved.

Another issue related to the CFD grid deformation and motion is related to refinement grids, designed to capture flow features of importance like tip vortices and regions of separation. These grids have to follow the blades accurately, which for deforming blades becomes difficult. An average of the motions of all bodies belonging to each blade is used to move the refinement grids attached to the blade.

In addition, difference in computational time steps between CFD and MBD codes may occur, as in the case to simulate wind turbine drivetrain, in which the small time step required by MBD to produce accurate solutions cannot be matched at a reasonable cost by CFD. To prevent sharp changes in forces when a new time step of CFD produces a new solution, the forces are interpolated from the current and previous CFD time step for all MBD time steps. This approach reduces to the standard exchange when both CFD and MBD time steps are coincident.

2.4 Explicit Wind Turbulence Model

A wind turbulence model that includes turbulence fluctuations and the effect of shear in the atmospheric boundary layer was implemented into the code CFDShip-Iowa v4.5 to provide appropriate initial and inlet boundary conditions. The model is recommended as the wind turbulence model by the international standard for wind turbines IEC 61400-1 ed. 3 (International Electrotechnical Committee 2005) and is suitable for CFD simulations.

In order to provide an appropriate atmospheric wind turbulence input that is suitable for dynamic wind loading analysis of engineering structures such as wind turbines and bridges, Mann (Mann 1994, 1998) proposed and developed an efficient wind turbulence model based on the construction of a spectral tensor for atmospheric surface-layer turbulence. The model is capable of simulating three-dimensional fields of all three components of the wind velocity fluctuations, and has the same second-order statistics as in the real atmosphere, e.g. variances and cross spectra.

There are a few assumptions in the Mann turbulence model to simplify its derivation while maintaining the physical nature of wind turbulence, mainly the statistics of the atmospheric wind turbulence of the model are assumed to be stationary in time and homogeneous in space (i.e. a stochastic process whose joint probability distribution does not change when shifted in time and space), and the wind velocities follow Gaussian distribution. Therefore, what the Mann model provides is a stationary "Mann box" in three-dimensions with the spatially distributed wind fluctuations, which stochastically agree well with the measurements of wind turbulence. Based on that, Mann model adopts the Taylor's frozen turbulence hypothesis to relate the spatial wind fluctuations with time, which interprets time series as "space series". Also, starting from the basis of the isotropic Von Karman spectrum, Mann's model linearizes the N-S equation to estimate the effect of the shear on the turbulence by assuming the mean wind field can be represented by a uniform shear with the flow in the prevailing wind direction $\boldsymbol{U}(\boldsymbol{x}) = z\, dU/dz\, \boldsymbol{e}_1$, (where dU/dz is a constant, z the vertical position, $\boldsymbol{e}_1$ is the prevailing wind direction), while applying the rapid distortion theory (RDT) to model the response of turbulence to shear, such that the wind turbulence is anisotropic.

2.4.1 Spectral Representation of the Velocity Field

The velocity is modeled as a stochastic field using the generalized Fourier-Stieltjes integral

$$\boldsymbol{u}(\boldsymbol{x}) = \int e^{i\boldsymbol{\kappa}\cdot\boldsymbol{x}} d\boldsymbol{Z}(\boldsymbol{\kappa}) \tag{2.21}$$

where the integration in the wavenumber vector $\boldsymbol{\kappa}$ spans the entire wavenumber space, and $\boldsymbol{Z}$ is a orthogonal stochastic process related to the velocity-spectrum tensor Φ_{ij} by

$$\langle dZ_i^*(\boldsymbol{\kappa}) dZ_j(\boldsymbol{\kappa})\rangle = \Phi_{ij}(\boldsymbol{\kappa}) d\kappa_1 d\kappa_2 d\kappa_3 \tag{2.22}$$

with * denoting conjugation and $\langle\cdot\rangle$ ensemble averaging. Equation (2.22) is valid for infinitesimally small $d\kappa_\mathrm{i}$. For isotropic flows the velocity spectrum tensor $\Phi_{\boldsymbol{ij}}$ is related to the three dimensional energy spectrum by

$$\Phi_{ij}(\boldsymbol{\kappa}) = \frac{E(\kappa)}{4\pi\kappa^4}(\delta_{ij}\kappa^2 - \kappa_i\kappa_j) \tag{2.23}$$

where the energy spectrum $E(\kappa)$ is modeled using the von Kármán model.

$$E(\kappa) = \alpha\varepsilon^{2/3}L^{5/3}\frac{L^4\kappa^4}{(1+L^2\kappa^2)^{17/6}} \tag{2.24}$$

with $\alpha \approx 1.5$ the Kolmogorov constant, ε the turbulence dissipation and L a length scale that for high Reynolds numbers approaches the limit $L \approx 0.43\, L_{11}$ with L_{11} the integral length scale. The integral over all wave numbers of the energy spectrum equals the total turbulent kinetic energy k. Performing this integration leads to $\alpha\varepsilon^{2/3}L^{5/3} = 1.453\, \sigma_{\mathrm{iso}}^2\, L$ which allows to eliminate the turbulence dissipation by the mean turbulent fluctuations σ_{iso} related to the turbulent kinetic energy by $k = 3/2\sigma_{\mathrm{iso}}^2$.

It is practically impossible to determine $E(\kappa)$ experimentally. However, one-dimensional spectra can be determined by single-point velocity measurements. A relationship exists between the one-dimensional spectra and the three dimensional spectrum (Pope 2000) which if applied to the von Kármán model in Eq. (2.24) allows to obtain the one-dimensional spectra for the streamwise and transverse directions as

$$F_1(\kappa_1) = \frac{9}{55}\alpha\varepsilon^{2/3}L^{5/3}\frac{1}{(1+(L\kappa_1)^2)^{5/6}} \tag{2.25}$$

$$F_i(\kappa_1) = \frac{3}{110}\alpha\varepsilon^{2/3}L^{5/3}\frac{3+8(L\kappa_1)^2}{(1+(L\kappa_1)^2)^{11/6}} \quad (i = 2,3) \tag{2.26}$$

2.4.2 Discrete Representation in Fourier modes

Equation (2.21) is approximated by a discrete Fourier series as

$$u_i(\boldsymbol{x}) = \sum_{\boldsymbol{\kappa}} e^{i\boldsymbol{\kappa}\cdot\boldsymbol{x}}\, \hat{\boldsymbol{u}}(\boldsymbol{\kappa}) = \sum_{\boldsymbol{\kappa}} e^{i\boldsymbol{\kappa}\cdot\boldsymbol{x}} C_{ij}(\boldsymbol{\kappa}) n_j(\boldsymbol{\kappa}) \tag{2.27}$$

where $\hat{\boldsymbol{u}}(\boldsymbol{\kappa})$ are the Fourier modes of the velocity field and $n_j(\boldsymbol{\kappa})$ are independent Gaussian complex variables with unit variance. In Mann (1998) the relationship between the velocity spectrum and the coefficients $C_{ij}(\boldsymbol{\kappa})$ is found leading to

$$C_{ij}(\boldsymbol{\kappa}) = \left(\frac{E(\kappa_0)\cdot 2\pi^2}{L_1 L_2 L_3 \kappa_0^4}\right)^{1/2} \begin{bmatrix} \kappa_2\zeta_1 & \kappa_3 + \kappa_1\beta - \kappa_1\zeta_1 & -\kappa_2 \\ -\kappa_3 - \kappa_1\beta + \kappa_2\zeta_2 & -\kappa_1\zeta_2 & \kappa_1 \\ \frac{\kappa_0^2}{\kappa^2}\kappa_2 & -\frac{\kappa_0^2}{\kappa^2}\kappa_1 & 0 \end{bmatrix} \tag{2.28}$$

$$\zeta_1 = C_1 - \kappa_2 C_2/\kappa_1,\ \zeta_2 = \kappa_2 C_1/\kappa_1 + C_2 \tag{2.29}$$

$$C_1 = \frac{\beta\kappa_1^2\left(\kappa_1^2+\kappa_2^2-\kappa_3(\kappa_3+\beta\kappa_1)\right)}{\kappa^2(\kappa_1^2+\kappa_2^2)},\ C_2 = \frac{\kappa_2\kappa_0^2}{(\kappa_1^2+\kappa_2^2)^{3/2}} \arctan\left(\frac{\beta\kappa_1\sqrt{\kappa_1^2+\kappa_2^2}}{(\kappa_0^2-\beta\kappa_1(\kappa_3+\beta\kappa_1))}\right) \tag{2.30}$$

$$\beta = \frac{\Gamma}{\kappa^{\frac{2}{3}}\cdot\sqrt{{}_2F_1\left(\frac{1}{3},\frac{17}{6},\frac{4}{3},-\kappa^{-2}\right)}} \tag{2.31}$$

where L_i are the dimensions of the physical domain, $\kappa = \sqrt{\kappa_1^2+\kappa_2^2+\kappa_3^2}$ is the magnitude of the wave number and $\kappa_0 = \sqrt{\kappa^2 + 2\beta\kappa_1\kappa_3 + (\beta\kappa_1)^2}$ is the magnitude before shear distortion. The model includes the effect of shear through the dimensionless distortion time β where $\Gamma = 3.9$ is used as recommended by the IEC and ${}_2F_1$ is the hypergeometric function. The parameters of the model σ_{iso} and L are estimated following the IEC standard from where

$$L[\text{m}] = \begin{cases} 0.56\, z_h & z_h < 60\ \text{m} \\ 33.6\ \text{m} & z_h > 60\ \text{m} \end{cases} \tag{2.32}$$

$$\sigma_{\text{iso}}[\text{m/s}] = 0.55\, I_{\text{ref}}\,(0.75\, U_h[\text{m/s}] + 5.6) \tag{2.33}$$

where z_h and U_h are the hub height and mean wind velocity at the hub height, respectively. Units are indicated in brackets. I_{ref} is a reference turbulent intensity specified according to the wind classes defined in the IEC standard. Once the Fourier

modes $\hat{\boldsymbol{u}}(\boldsymbol{\kappa})$ are computed the physical velocity is obtained by inversion of Eq. (2.27) using an FFT.

2.4.3 Verification of the Divergence–free Velocity Field

The condition of divergence-free velocity is critical for CFD computations. However, since the wind turbulence velocity fluctuations in time domain are obtained through FFT computations in frequency domain, and the corresponding derivations are in frequency domain and focused more on the statistical accuracy than the physical considerations, though the Mann model produces incompressible velocity field, it is not quite clear whether the generated velocity field is divergence-free in the discretized domain as required by CFD. This is probably the main concern for some CFD simulation tools to introduce the Mann model via body forces in the momentum equations as immersed boundary instead of the simpler inlet boundary. In this section, an inspection is conducted to show the degree of satisfaction of the continuity constraint.

In wave space, the velocity field can be expressed in Fourier series as stated in Eq. (2.27). Let $\hat{u}(\boldsymbol{\kappa}) = C_{ij}(\boldsymbol{\kappa})n_j(\boldsymbol{\kappa})$ for convenience. The divergence of velocity in the frequency domain can be expressed as

$$\mathcal{F}_\kappa\left\{\frac{\partial u_j}{\partial x_j}\right\} = i\kappa_j\hat{u}_j = i\boldsymbol{\kappa}\cdot\hat{\boldsymbol{u}} \tag{2.34}$$

where $\mathcal{F}_\kappa$ denotes Fourier transform operation.

From Eq. (2.34), the continuity equation $\nabla\cdot\boldsymbol{u} = 0$ in time domain indicates that $\hat{\boldsymbol{u}}$ is normal to $\boldsymbol{\kappa}$, i.e. $\boldsymbol{\kappa}\cdot\hat{\boldsymbol{u}} = 0$. By inserting the coefficient matrix $C_{ij}(\boldsymbol{\kappa})$ which has explicit expression with undetermined parameters from Eq. (2.28), it turns out that

$$\boldsymbol{\kappa}\cdot\hat{\boldsymbol{u}} = \boldsymbol{\kappa}\cdot\boldsymbol{C}(\boldsymbol{\kappa}) = \boldsymbol{0} \tag{2.35}$$

Equation (2.35) is valid for all wave vectors and independent of the random Gaussian variable $n_j(\boldsymbol{\kappa})$, therefore all discrete points in the Mann box conserve

continuity. However, it should be note that the continuity in general is not conserved in the discretized finer simulation domain.

2.4.4 Computation of the Pressure Field

It is usually sufficient to have the velocity field as the solely wind turbulence input for most of the simulation tools, and thus there is no description for the computation of the corresponding pressure field in Mann model. However, the pressure field is needed for CFD simulations. This can be obtained by solving the N-S equations in the frequency domain as done in the context of DNS simulations using spectral methods (Pope 2000).

The Poisson equation for pressure obtained from N-S equations in wavenumber space can be expressed as

$$\mathcal{F}_\kappa\{-\nabla^2 p\} = \mathcal{F}_\kappa\left\{\frac{\partial}{\partial x_j}\left(\frac{\partial}{\partial x_k}\left(u_j u_k\right)\right)\right\} \tag{2.36}$$

Relationship between the Fourier coefficient of the dynamic pressure (p/ρ) and the Fourier coefficients of velocities can be expressed as

$$\hat{p}(\boldsymbol{\kappa}, t) = i\kappa_j \hat{G}_j/\kappa^2 \tag{2.37}$$

$$\hat{G}_j(\boldsymbol{\kappa}, t) = \mathcal{F}_\kappa\left\{\frac{\partial}{\partial x_k}\left(u_j u_k\right)\right\} = i\kappa_k \mathcal{F}_\kappa\{u_j u_k\} \tag{2.38}$$

$$\hat{p}(\boldsymbol{\kappa}, t) \equiv \mathcal{F}_\kappa\{p(x,t)/\rho\} \tag{2.39}$$

where $\hat{p}$ is the Fourier coefficient of the dynamic pressure in wavenumber space.

The product $u_j u_k$ in Eq. (2.38) is computed in the physical domain with the generated velocity field and then transformed to the frequency domain where Eqs. (2.37) and (2.38) are evaluated. Pressure in the physical domain is then obtained by applying the inverse Fourier transform to Eq. (2.39) using an FFT.

2.4.5 Implementation into CFDShip-Iowa v4.5

The general schematic for the implementation of Mann wind turbulence model into CFDShip-Iowa v4.5 as wind turbulence boundary condition is shown in Fig. 2.3,

which also shows cross sections in the Mann's box with non-dimensional axial velocity U. A stationary Mann wind turbulence box is generated as a pre-processing step computing FFT using the FFTW library(Frigo and Johnson 2005). Since by construction the velocity field is periodic, the dimensions of the box are chosen to be several integral length scales such that velocities at the opposite faces of the box can be considered to be uncorrelated. As depicted in Fig. 2.3, at time $t = 0$ the front face of the Mann box is coincident with the inlet of the CFD domain. Using Taylor's hypothesis of frozen turbulence, velocity and pressure at the inlet are interpolated from a plane within the Mann box located at $x = L_1 - U_h t$. This plane is made to go back to the front of the box once it reaches the back using the fact that the generated velocity field is periodic. This procedure is equivalent to having the Mann box moving forward as depicted in Fig. 2.3. Using the same Taylor's hypothesis velocity and pressure are initialized at $t = 0$.

The generation of Mann wind turbulence box is fast with FFT. For a Mann box with dimension of $128 \times 64 \times 64$ points in the three directions, it typically takes less than 0.2 seconds for a single processor to complete the computation. In addition, with the superposition of mean wind profiles, including uniformly distributed, log law and power law winds, the effect of wind atmospheric boundary layer with wind shear can be estimated with or without wind turbulence for both onshore and offshore wind turbine simulations.

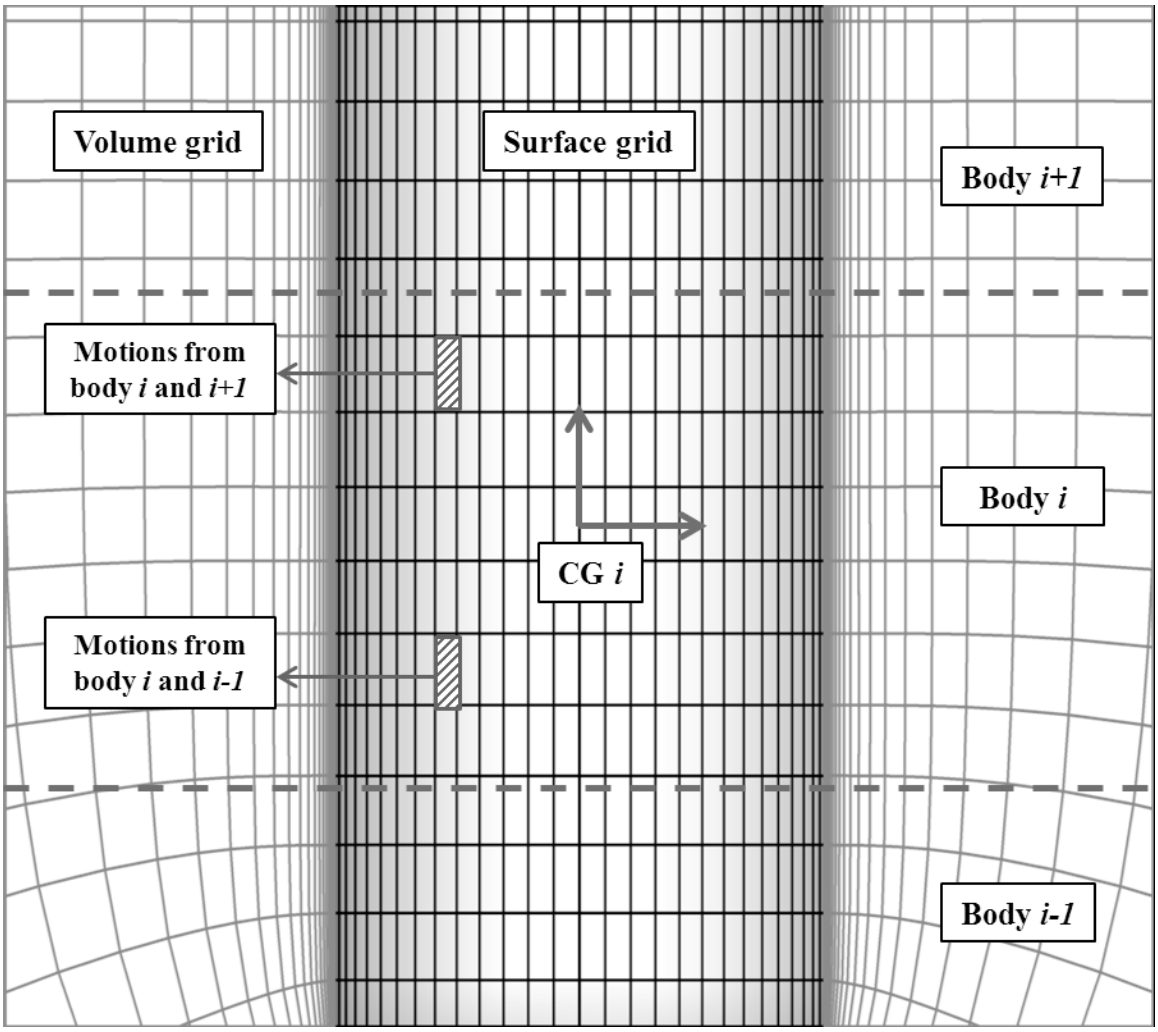

Figure 2.1 Schematic demonstration of information exchange

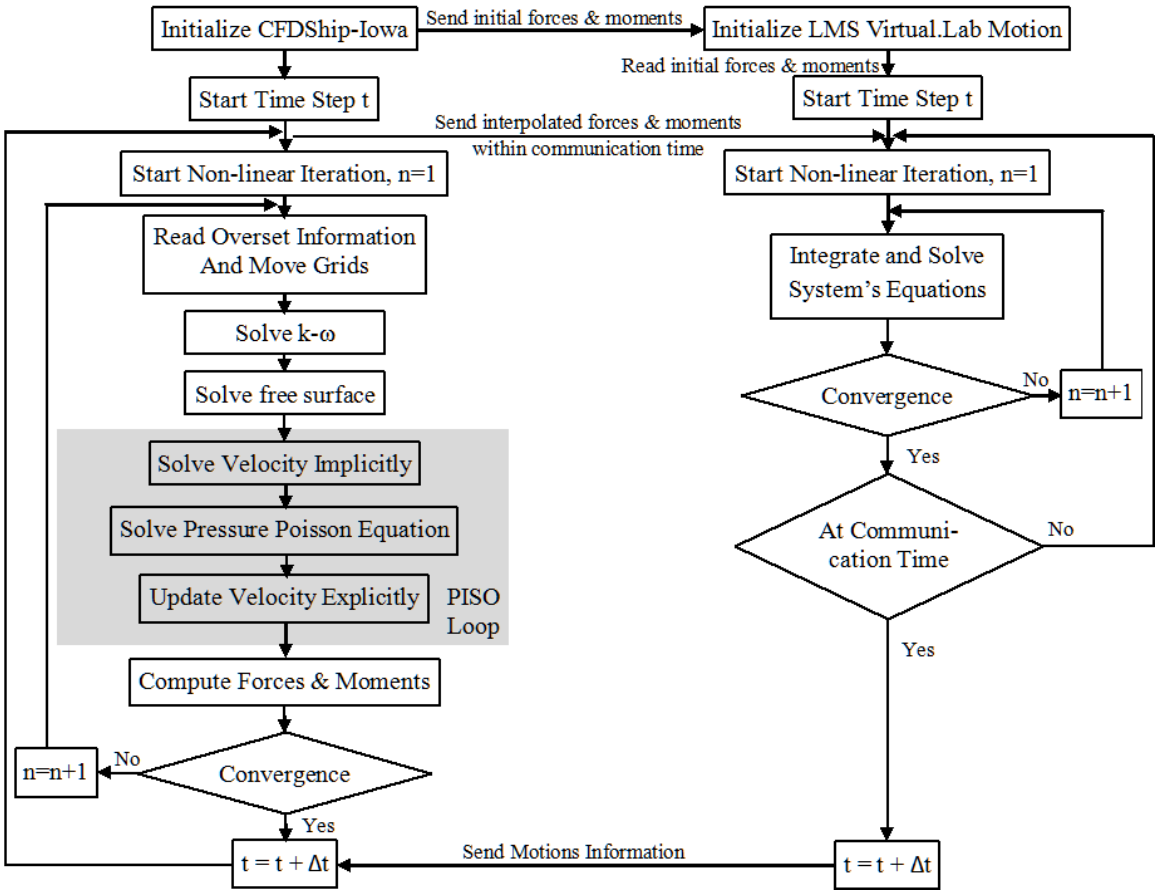

Figure 2.2 Coupling strategy

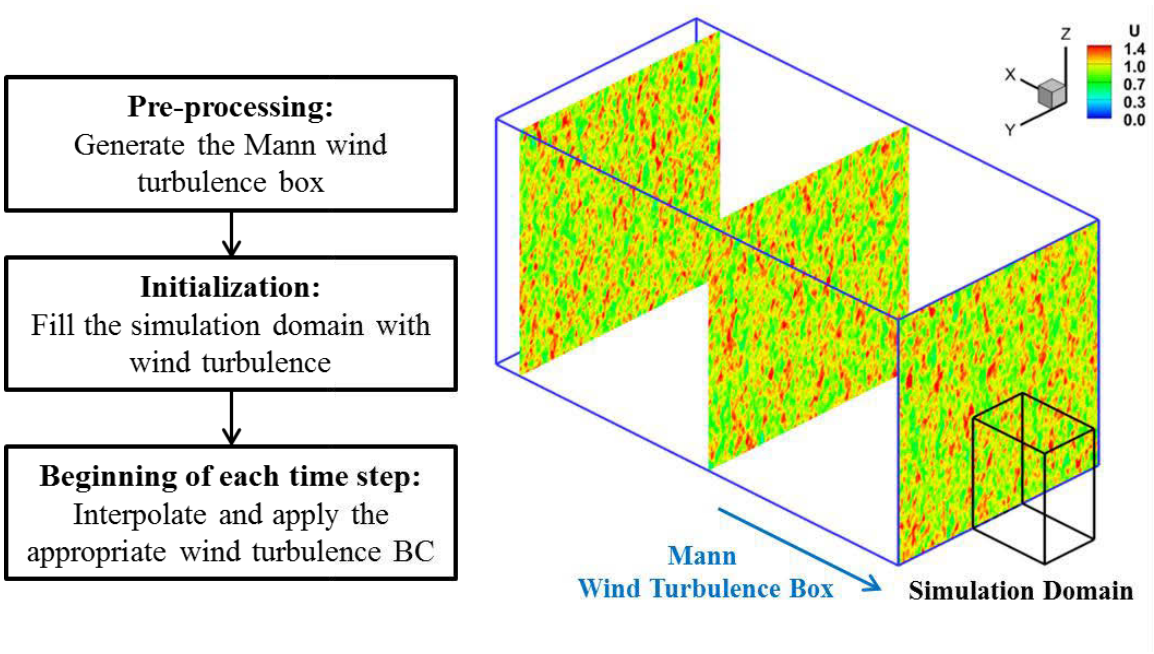

Figure 2.3 Schematic of implementation for Mann wind turbulence model

CHAPTER 3
UNSTEADY AERODYNAMICS EXPERIMENT PHASE VI TURBINE SIMULATIONS

3.1 Overview

Most computations to date testing numerical methods for aerodynamic predictions are compared to the National Renewable Energy Laboratory (NREL) Unsteady Aerodynamics Experiment (UAE) (Fingersh et al. 2001; Hand et al. 2001), which provides comprehensive high-quality data for a modified Grumman 20 KW twin-bladed turbine, tested in the wind tunnel at NASA Ames. The most important results are in the Phase VI of the experiments. A blind numerical study involving 20 different participants using various CFD codes was conducted subsequently (Schreck 2002).

Notice that most studies for wind turbines consider the rotor-only geometry, excluding the tower and nacelle; in most cases only one blade was included in the simulation. These simplifications are understandable because the resulting grid is static throughout the calculation and thus greatly alleviate the computational complexity and cost, but they can leave out some important effects. Dynamic moving overset grid technique is one of the methods that allow for computation of bodies with relative motions, including elastic deformation for both on-shore and off-shore wind turbines, and the floating motions for offshore wind turbines.

3.2 Simulation Design

3.2.1 Simulation Turbine

The testing wind turbine is the NREL phase VI, a modified Grumman Windstream 33 stall-regulated turbine with full-span pitch control and a power rating of 20 KW. It has 2 blades, with NREL s809 tapered and twisted blade profile. The rotor diameter is 10.058 m while hub height is 12.192 m. The experiments were performed in

the NASA Ames wind tunnel in 1999 and are considered a benchmark for evaluation of wind turbine aerodynamics computer codes. Detailed geometry, machine parameters and experimental procedures can be found in the NREL report (Hand et al. 2001; Simms et al. 2001).

3.2.2 Grid Design

The grid design for the on-shore turbine simulations is shown in Fig. 3.1. The geometries of the nacelle and hub have been approximated and do not correspond to the true shape of the NREL VI turbine. The grid system consists of 13 overset blocks to discretize the blades, hub, nacelle, tower and floor. The blades themselves are each gridded with an O-type block to cover the span, one block for the tip and one for the root. O blocks are used for the hub and nacelle as well as for the tower. A refinement block is used to match the nacelle grid with those from the hub/blade roots/tower systems. Finer refinements are used to capture the flow around the rotor using a Cartesian block and an O-type block. Overall 52.3 million grid points are used, distributed in 2048 domains each sent to a processor, with an average of 28,046 grid points per processor and a maximum deviation around the average of 2.2% maximum. After splitting, the 52.3 million grid points increase to 57.4 million due to duplication on the block to block interfaces, see Table 3.1.

Since surface overset grids are used, the computation of forces and areas requires evaluation of the portions that are overset to avoid double-counting in overlaid areas. This is done as a pre-processing step with the code Usurp (Boger and Dreyer 2006), which generates weights that alter the area of each cell on the solid body to provide the appropriate forces and areas at each cell.

The grids are organized in a parent/child hierarchy, as shown in Table 3.1. The grids comprising the blades can pitch about the pitching axis, while these and the hub form the rotor, which rotates about the shaft axis. The nacelle and the rotor form the body

Nacelle which can rotate about the tower axis with the yaw angle. In this way a fully controlled turbine can be simulated, with a rotational speed controller acting on the blade pitch and an attitude controller acting on the yaw. In this work the yaw is kept at 0 degrees, but the pitch is modified dynamically to perform the simulations of variable-pitch control. The time step was chosen such that the blades rotate 1 degree per time step for cases with 5 to 15 m/s wind speed, and 0.5 degrees for cases with 25 m/s wind speed.

3.2.3 Simulation Cases

Two cases were selected from the test matrix of the NREL experiments, belonging to sequences S and K. In particular, simulations for sequence S are used to evaluate the ability of the code to predict the aerodynamics under different wind velocities (5, 10, 15 and 25 m/s) at a fixed 3 degrees blade tip pitch angle. Simulations for sequence K are designed to evaluate the performance of the 3D blade in the presence of rotation to different static angles of attack by varying the blade tip pitch angles from 40 to -15 degrees in steps of 5 degrees. The wind velocity for sequence K is fixed at 15 m/s (the experimental data also evaluates 6, 10 and 20 m/s). For both cases the rotational speed is 72 RPM. Several yaw angles were tested experimentally, but only those with the yaw angle fixed at 0 degree were simulated. Table 3.2 summarizes all CFD simulation cases.

RANS and DES computations were conducted for sequence S to investigate the response of the two methodologies for wind turbine modeling, while only DES was applied to sequence K. In both cases hybrid 2^{nd}-4^{th} order schemes were used for convection.

3.3 Results and Discussion

3.3.1 Variable Wind Speed at Constant Pitch Angle

The experimental sequence S comprises data at 3 degrees of blade pitch for wind speeds from 5 to 25 m/s at intervals of 1 m/s. The CFD study is focused on 5, 10, 15 and 25 m/s. The highest two wind speeds correspond to stall conditions in most of the blade and simulations are thus challenging. This is shown in Fig. 3.2, which illustrates the vortical structures using iso-surfaces of the second invariant of the rate of strain tensor (Hunt et al. 1988) at $Q = 5$. It is clear that these DES computations predict fully attached flow for 5 and 10 m/s, with development of unsteady trailing vortices at 10 m/s. At these two velocities the blade tip vortices are strong and stable. Strong vortices detach also from the tower and the roots of the blades, where the geometry changes quickly from the s809 profile to cylindrical posts attached to the hub. Notice that the vortical structures dissipate quickly away from the regions covered by grid refinements, downstream of the rotor plane and at the tower below 1 blade length. At 15 m/s about the outer half of the blade experiences massive unsteady separation, while at 25 m/s most of the blade suffers massive unsteady flow separation. For these two higher velocities the interaction of the tip vortices with the unsteady separation from the suction side of the blades causes breakdown of the tip vortices, very dramatically at 25 m/s. Also, note the tower vertical vortices tend to evolve into hairpin vortices and into smaller structures as the wind speed increases. The formation of these hairpin vortices is interesting, since it requires the presence of gradients of streamwise velocities (Dousset and Pothérat 2010), which in this case occur along the rotor, and especially by the rotor tip vortex.

Figure 3.3 shows comparisons of predicted vortical structures at two wind speeds for RANS and DES computations. At 5 m/s both methods predict essentially the same flow around the blades. More vortices can be observed for DES in the separated flow regions close to the hub, tower and nacelle, but these have lesser effect on the

performance of the turbine. At wind speed of 25 m/s the differences between RANS and DES are more dramatic. In particular the separation bubbles on the suction side of the blade are highly unsteady and are shed periodically for the DES computation, while they are mostly steady for RANS. This causes a stable tip vortex for RANS, while the tip vortex breaks down for DES, as previously discussed.

The experimental thrust and torque (and thus power) are obtained integrating the pressure measurements along the blade, and consequently the friction effects are neglected. CFD computations account for both pressure and friction forces. Figures 3.4 and 3.5 show comparisons of thrust and power between DES-based CFD and NREL experiments for Sequence S. In all figures the vertical bars represent the experimental standard deviation, not the error or experimental uncertainty, which is not reported in the experiment report (Hand et al. 2001). Overall CFD simulations predict very well the general performance of the turbine, even at the two highest wind speeds where stalled flows occur. CFD predictions of the thrust are all well within the standard deviation of the experimental measurements, except for a slight over prediction at 25 m/s where as previously shown stalled flow and separation are pronounced. The friction component on the total thrust is negligible. Power is a bit underpredicted, except for the highest speed. In addition, results neglecting friction in the computation of the forces are closer to the experimental data as expected, but the friction force contribution is still small except at slower wind speeds. Notice that the code predicts properly the flattening of the power as a function of the wind speed as the turbine becomes stall-controlled at higher wind speeds.

As thrust and power are parameters integrated over the area of the blades, evaluation of sectional force coefficients such as radial normal force coefficient C_n allows a better check on the ability of the code to properly capture the aerodynamic behavior of the wind turbine. The normal force coefficient is still an integration of pressure but limited to a section of the blade. As pointed out by Simms et al. (2001), who

summarized blind predictions of several codes for the Phase VI turbine, good prediction of integrated parameters can be obtained with models that over predict aerodynamic forces on the inboard part of the blade, while under predicting the forces outboard. Figure 3.6 compares RANS and DES CFD and experimental results of C_n at 5 different sections of the blade. Both RANS and DES match very well the experimental measurements for all wind velocities simulated. In particular, at lower wind velocities (5 m/s) where no flow separation occurs except at the transition section near the root, RANS and DES simulations show accurate predictions with little difference between each other, as expected from the similarity shown in the flow regimes from Fig. 3.3. At higher wind velocities, where flow separation becomes more important and vortex shedding occurs, discrepancies appear gradually. At 15 m/s RANS and DES results are very similar for $r/R < 0.5$ where the flow around the blade separates weakly (see Fig. 3.2 for the DES results), but differ more for $r/R > 0.5$ where separation and vortex shedding are important and differences in flow pattern between RANS and DES are remarkable. At 25 m/s the differences between RANS and DES are significant for all sections, as expected from the dramatic difference in flow patterns shown in Fig. 3.3. Observe that RANS computations tend to predict more lift as the flow remains attached at larger angles of attack. All normal force coefficients are well predicted with DES with the exception of section $r/R = 0.63$ at V=15 m/s and section $r/R = 0.47$ at V=25 m/s. Large differences in normal force coefficients at these sections and wind speeds are also shown in the computations of Duque et al. (2003).

Direct comparisons of the pressure coefficient C_p between CFD and experimental data at 5 different sections as a function of wind speed are shown in Fig. 3.7. The pressure coefficient is a harder test for CFD since it is a local quantity, and comparison is made against pressure taps installed in the blade. See that the incompressible formulation of CFDShip-Iowa, appropriate for wind turbines, does not produce the spurious pressure peaks observed on compressible codes (Duque et al. 2003). At low wind speeds the CFD

predictions match the experimental data remarkably well. For 10 m/s at $r/R = 0.47$ the experiments show a flat pressure on the suction side, indicating separation, while CFD results predict a leading edge peak. The same behavior occurs for 15 m/s at $r/R = 0.30$, where CFD predicts a peak at 0.2 chord lengths downstream of the leading edge while experimental results show a more flat pressure distribution. Notice that the integral of the pressure for these two anomalous conditions will be about the same for CFD and experiments, resulting in good prediction of the normal force coefficient. Duque et al. (2003) argued that possibly unsteadiness is the reason for these discrepancies, since they used the code Overflow-D in steady-state mode. This is not supported by the current simulations as similar differences are observed for DES that captures significant unsteadiness in the trailing edge on the suction side both for 10 m/s at $r/R = 0.47$ and for 15 m/s at $r/R = 0.30$. It is possible that CFD grossly under-predicts the separation, though it is hard to think of a mechanism that would separate locally at $r/R = 0.47$ for V = 10 m/s while all other sections inboard and outboard are attached. The two points in Fig. 3.6 that show the largest errors, section $r/R = 0.63$ at V = 15 m/s and section $r/R = 0.47$ at V = 25 m/s, show significant under prediction of the suction pressure and thus result in lower integral inside the curves.

Figure 3.8 shows instantaneous limiting streamlines on the blade, along with streamlines on the projected velocities at the selected sections. At low wind speed (5 m/s) the CFD computations predict fully attached flow everywhere in the active blade, and some separation where the s809 blade profile merges to a cylindrical section. At this speed the pressure stays low on the suction side and the blade provides consistent lift. At 15 m/s the flow exhibits significant separation at all sections, with smaller scale, unsteady vortices shed in the second half of the blade. For section $r/R = 0.47$ at this speed the flow separates from the leading edge and reattaches to the blade surface to form a closed separation bubble whereas all other sections show open separation where vortices are shedding away from the blade surface to the wake. Significant pressure recovery is

observed, mostly for the outer sections. Similar trends are observed for all sections at 25 m/s, but the separation is stronger with violent vortex shedding, with very little pressure recovery on the suction side indicating massive stall.

Time histories of C_p for 15 m/s at 3 degrees blade pitch angle are shown in Fig. 3.9a, and the corresponding frequency spectra are shown in Fig. 3.9b. The time evolution is expressed in terms of blade rotations with the blade down at zero rotations. The measurements were taken at five different points on sections r/R = 0.30, 0.47, 0.63, 0.80 and 0.95 at 44% of the chord from the leading edge on the pressure side. The CFD values correspond to one rotation saving every 4 (5 to 15 m/s) or 8 (25 m/s) time steps (90 points per rotation) and are repeated three times, due to the cost of saving large number of volume solutions and the corresponding processing. Because the absolute pressures are small, the differences between the mean values for experiments and CFD appear large for all sections except $r/R = 0.47$, but the largest error occurs at $r/R = 0.30$ and is less than 2.5% of the pressure dynamic range at that section, see Fig. 3.7.

Notice in Fig. 3.9b that the amplitude of the fluctuations is in general larger in the experiments than in CFD. At $r/R = 0.30$ the presence of the tower is clear, shown in Fig. 3.9a as an increase in pressure at integer rotations (0, 1, 2, etc.), and in Fig. 3.9b as a peak at 1.2 Hz, the rotational frequency. Large amplitudes at 1.2 Hz and 2.4 Hz are present at all sections, but the amplitude decreases for larger radii. Most of the frequency content is limited to frequencies below 10 Hz, as can be expected for a machine of this size. In CFD these high frequencies can be associated with vortex shedding. The magnitude of the fluctuations is larger in the experiments than in CFD at the other sections, but the difference is more evident at $r/R = 0.63$. Notice that the frequency content in CFD is comparable with the experiments, indicating that the turbulence model is able to capture most of the oscillations caused by organized vortical structures and fluctuations caused by turbulent structures. On the same line of analysis, the turbulence model seems to fail to capture the amplitude of the pressure fluctuations, likely due to

insufficient grid discretization to maintain the low pressure on the vortex cores, though other causes may be speculated that would cause differences in pressure fluctuation amplitudes, like blade vibrations caused by gears and bearings and by the elasticity of the blade. All these effects are neglected in current CFD simulations.

Time histories of thrust for 5, 10, 15 and 25 m/s at 3 degrees blade pitch angle are shown in Fig. 3.10a, and the frequency spectra in Fig. 3.10b. In this case the forces are saved every time step, so there are 1080 points in CFD for 5 to 15 m/s and 2160 for 25 m/s. To compare with the experiments fairly, the thrust in one blade is multiplied by two instead of using the thrust in both blades, which would smooth the transient behavior of CFD by adding two blades that have different instantaneous forces. The experimental thrust was obtained by integrating the pressures measured on the five sections at r/R = 0.30, 0.47, 0.63, 0.80 and 0.95, while CFD forces are integrated on every grid cell on the blade, smoothing transients more than in the experimental evaluation of the force by averaging local pressure highs with local pressure lows. It is not surprising then that the experiments show larger fluctuation amplitudes than CFD, though a significant portion of the larger fluctuations is likely due to inadequacy of the turbulence model to fully capture the transient instabilities observed in the flow, as discussed in the previous paragraph. Figure 3.10a clearly displays a decrease in thrust when the blade is in the downward position, indicating that the presence of the tower has a small but appreciable effect. This effect is most marked at 5 m/s and decreases with speed to be completely masked by fluctuations at 25 m/s. Perceive that at 5 m/s CFD shows no fluctuations since the flow does not separate, while the experiments show significant fluctuations, likely due to vibrations. The frequency spectrum at 5 m/s is matched very well by CFD at low frequencies, showing a peak at 2.4 Hz. At higher wind speeds the lower frequencies are matched reasonably but as expected higher frequencies are exhibiting amplitudes much smaller than the experiments. Sezer-Uzol and Long (2006) computed the case with 15

m/s, showing fluctuations of the thrust coefficient of about 1.8%, compared with 9% of the NREL experiments and 5% in this work.

Regarding performance of the two models, there are no major differences between RANS and DES when wind velocity is small, while small but clear differences can be seen at higher velocities on time-averaged quantities. However, both models predict the same trends and magnitudes for all blade sections, indicating that these models are capable tools for wind turbine simulations, at least within the conditions simulated herein. At higher wind speeds (25 m/s), where separation is massive, DES appears to produce better results, while the opposite occurs for lower wind speeds (15 m/s). A more advanced Delayed-DES (DDES) model (Shur et al. 2008) may be able to improve on these results.

3.3.2 Variable Pitch Angle at Constant Wind Speed

Computations with variable pitch follow one of the conditions of the experimental sequence K. In this case the pitch angle is varied from -15 degrees to 40 degrees in increments of 5 degrees for wind speed of 15 m/s. The resulting angles of attack at section $r/R = 0.30$ vary from 48.2 to -1.6 degrees and at $r/R = 0.95$ vary from 34 to -16.3 degrees. The experiments were performed for a step up, then step down procedure, while the computations were limited to the step up phase of the procedure. In the experiments there was an 8 seconds hold between pitch steps, while in CFD this hold was reduced to 4 seconds to save computational time.

Figure 3.11 shows vortical structures represented by iso-surfaces of $Q = 5$. At -15 degrees of pitch the angle of attack is maximum and as expected the separation is massive. The angle of attack is zero at the tip for approximately 25 degree pitch, and at this condition there is a consequent absence of tip vortices. At higher pitch angles the angle of attack becomes negative and the turbine starts behaving as a fan. This can be seen in Fig. 3.12, which shows the thrust force on the shaft as a function of pitch angle.

The thrust continuously decreases with increasing pitch angle, and is negative for pitch angles bigger than 30 degrees. Notice the remarkably good predictions for all positive pitch angles, while the difference with the experiments increases for very large angles of attack (negative pitch angles), to reach 9% difference at -15 degree pitch.

The effect of pitch angle on power is shown in Fig. 3.13. This is an important curve since it guides the design of the controller of a pitch-controlled turbine. At wind speed of 15 m/s the maximum power predicted by CFD is 19.1 KW and occurs at 15 degree pitch, compared to the maximum experimental value of 18.9 KW at the same pitch angle and a rated power of 19.8 KW. At this wind speed the wind kinetic carries a potential of 160 KW, which implies a maximum mechanical efficiency of 12%. This value is particularly low because under the cited conditions the turbine is in off-design operation. At 15 degree pitch angle, the angle of attack is 21 degrees at $r/R = 0.30$ and 6.6 degrees at $r/R = 0.95$, while equal angles of attack would be achieved at wind speed of 7.5 m/s approximately. At high angles of attack CFD tends to overpredict the power, while at higher blade pitch angles (smaller and negative angles of attack) the trend reverses and the power is underpredicted. Still the ability of the code to predict this curve is remarkable.

The normal coefficient C_n is shown in Fig. 3.14. The predictions are in good agreement with experiments for a wide range of sectional locations and pitch angles. Significant underpredictions occur at high angles of attack for $r/R = 0.47$ and $r/R = 0.80$, for moderate angles of attack at $r/R = 0.63$ and for low angles of attack at $r/R = 0.30$. The largest deviations are present at the innermost sections of the blade, with excellent results for $r/R = 0.80$ and $r/R = 0.95$. Notice that the normal force coefficient is, for the same blade pitch angle, mostly larger in the inner sections of the blade, consistent with a larger angle of attack in those sections. At $r/R = 0.95$, where large flow separation is observed up to about 10 degrees of pitch (see Fig. 3.11), the normal force coefficient remains flat until the flow is attached, evidencing stall at large

angles of attack. The essentially flat response with pitch angle occurs 5~10 degrees of pitch angle, and then the normal force decays faster with decreased angle of attack, becoming negative for negative angles of attack (pitch angles greater than 25 degrees at $r/R = 0.95$ and greater than 38 degrees at $r/R = 0.30$).

Figure 3.15 shows results of pressure distributions at three blade sections for pitch angles from -15 to 40 degrees. Predictions at $r/R = 0.95$ are excellent in trend and magnitude and are very good at $r/R = 0.63$ with some magnitude issues discussed later. In contrast, predictions at $r/R = 0.30$ are excellent in trend and magnitude for small angles of attack but fair for high angles of attack (pitch angles from -15 to 10 degrees). At section $r/R = 0.30$ the experiments show a much flatter pressure coefficient on the suction side of the blade than the CFD predictions, mostly for 10 degrees of blade pitch angle where the CFD and experiment discrepancies are largest. At 15 degrees of pitch angle and higher the experiments and CFD both show attached flow and the agreement is excellent. The integral of the pressure on the normal direction, leading to the normal force coefficient of Fig. 3.14, is still excellent except for 10 degrees of pitch angle, indicating that the errors in pressure tend to cancel each other at other sections, as can be seen in Fig. 3.14. At $r/R = 0.63$ the predicted trends are in good agreement with the data, showing stalled flow up to about 10 degrees of pitch angle, and attached flow thereafter. The magnitude of the pressure on the suction side is a bit underpredicted for pitch angles from -5 to 10 degrees, resulting in underpredicted normal forces as seen in Fig. 3.14. At section $r/R = 0.95$ the flow is stalled with flat pressure distributions on the suction side up to 0 degrees blade pitch, and then remains mostly attached. The agreement at all angles of attack is excellent. Notice that the suction and pressure sides are reversed for negative angles of attack at all sections.

Cross-sections at $x/R = 0.8$ showing instantaneous axial velocity are depicted in Fig. 3.16, representing the near wakes at pitch angles -15, -5, 5, 15, 25 and 40 degrees. The axial velocity exhibits decreases that are consistent with the level of power generated

at this wind speed, shown in Fig. 3.13. The vortical structures evident in Fig. 3.11 at stall conditions (negative or small pitch angles) are present in the form of large variations of axial velocity. For instance at -15 degrees pitch there are extensive areas with axial velocities higher than the incoming wind speed, mainly near the tip of the blade, and very low velocities for regions close to $r/R = 0.30$, but again very high wind speeds around the nacelle. On the other extreme, at 40 degrees pitch the turbine is actually working as a fan and the axial velocities are higher than the inlet velocity.

3.4 Summary

In this chapter, dynamic overset CFD simulations for the NREL phase VI wind turbine were presented to validate the capabilities of the code for wind turbine simulations. In particular, two sequences of the experiment test cases are studied with complete turbine geometry, including the NREL phase VI blades, and approximate geometries for hub, nacelle and tower. RANS and DES models are used in the simulations, and extensive comparisons with experimental data are performed. The motion model coupled with the overset methodology allows for the presence of parent/children objects, enabling the computation of variable blade pitch in a moving rotor with respect to static tower, nacelle and ground. Results at constant pitch and variable wind speed (experimental sequence S) or with constant wind speed and variable pitch (experimental sequence K) show that the CFD predictions match the experimental data consistently well, including the general trends of power and thrust, sectional normal force coefficients and pressure coefficients at different sections along the blade. At very large angles of attack the conditions are more demanding and the CFD results tend to slightly overpredict the thrust and underpredict the power. Evaluation of the transient pressure on the blades reveals that DES is able to predict fluctuations with similar frequencies to the experimental measurements; however, at least at the level of grid

resolution used in this study, the amplitude is underpredicted, mainly at the outermost sections.

Table 3.1 Grid details

Name	imax	jmax	kmax	Procs	isplit	jsplit	ksplit	Processor points	Total	Hierarchy
Hub	121	101	51	24	41	26	26	27716	665K	Rotor-Nacelle
Blade 1	201	101	241	192	35	26	31	28210	5.41M	Blade-Rotor-Nacelle
Tip 1	121	101	101	48	41	26	26	27716	1.33M	Blade-Rotor-Nacelle
Root 1	201	101	31	24	35	26	31	28210	677K	Blade-Rotor-Nacelle
Blade 2	201	101	241	192	35	26	31	28210	5.41M	Blade-Rotor-Nacelle
Tip 2	121	101	101	48	41	26	26	27716	1.33M	Blade-Rotor-Nacelle
Root 2	201	101	31	24	35	26	31	28210	677K	Blade-Rotor-Nacelle
Refinement	241	262	262	648	31	30	30	27900	18.08M	Earth
Ref. Tip	61	1081	201	512	31	35	26	28210	14.44M	Nacelle
Ref. Nacelle	221	69	69	40	23	35	35	28175	1.13M	Nacelle
Tower	214	61	71	36	37	31	25	28675	1.03M	Earth
Nacelle	151	61	101	36	26	31	35	28210	1.02M	Nacelle
Background	241	151	151	224	31	39	23	27807	6.23M	Earth
Total				**2048**				**Ave:28046**	**57.43M**	

Table 3.2 Simulation cases

Case No.	Nominal Wind Speed [m/s]	Re (based on blade length)	Pitch [degree]	Run	RANS/DES
1	5	1.766×10^{6}	3	S0500000	RANS
2	15	5.205×10^{6}	3	S1500000	RANS
3	25	8.645×10^{6}	3	S2500001	RANS
4	5	1.766×10^{6}	3	S0500000	DES
5	10	3.535×10^{6}	3	S1000000	DES
6	15	5.205×10^{6}	3	S1500000	DES
7	25	8.645×10^{6}	3	S2500001	DES
8	15	5.241×10^{6}	-15 to 40 In 5 degree steps	K1500ST1	DES

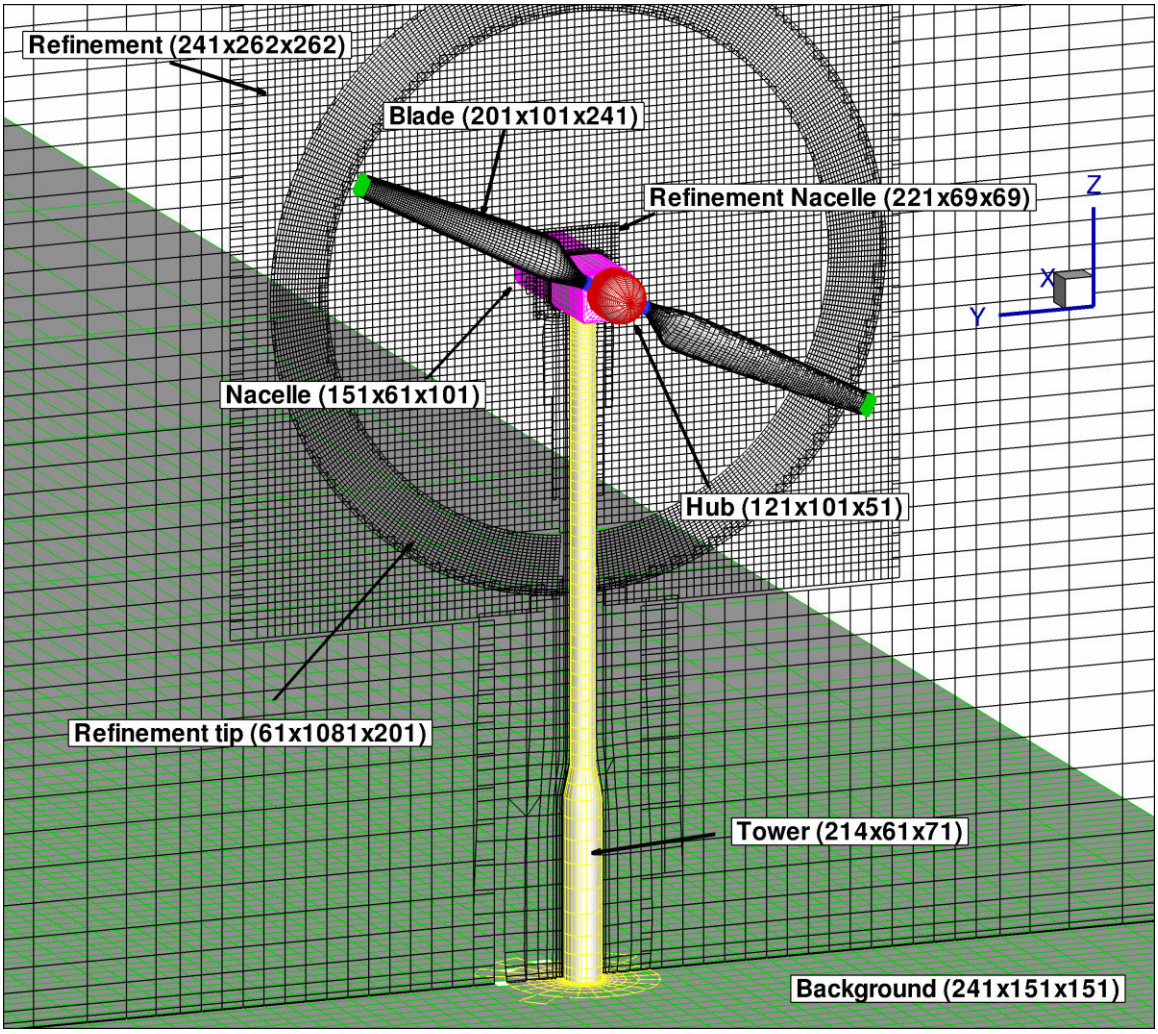

Figure 3.1 Grid design (Grid points are skipped in all directions for clarity)

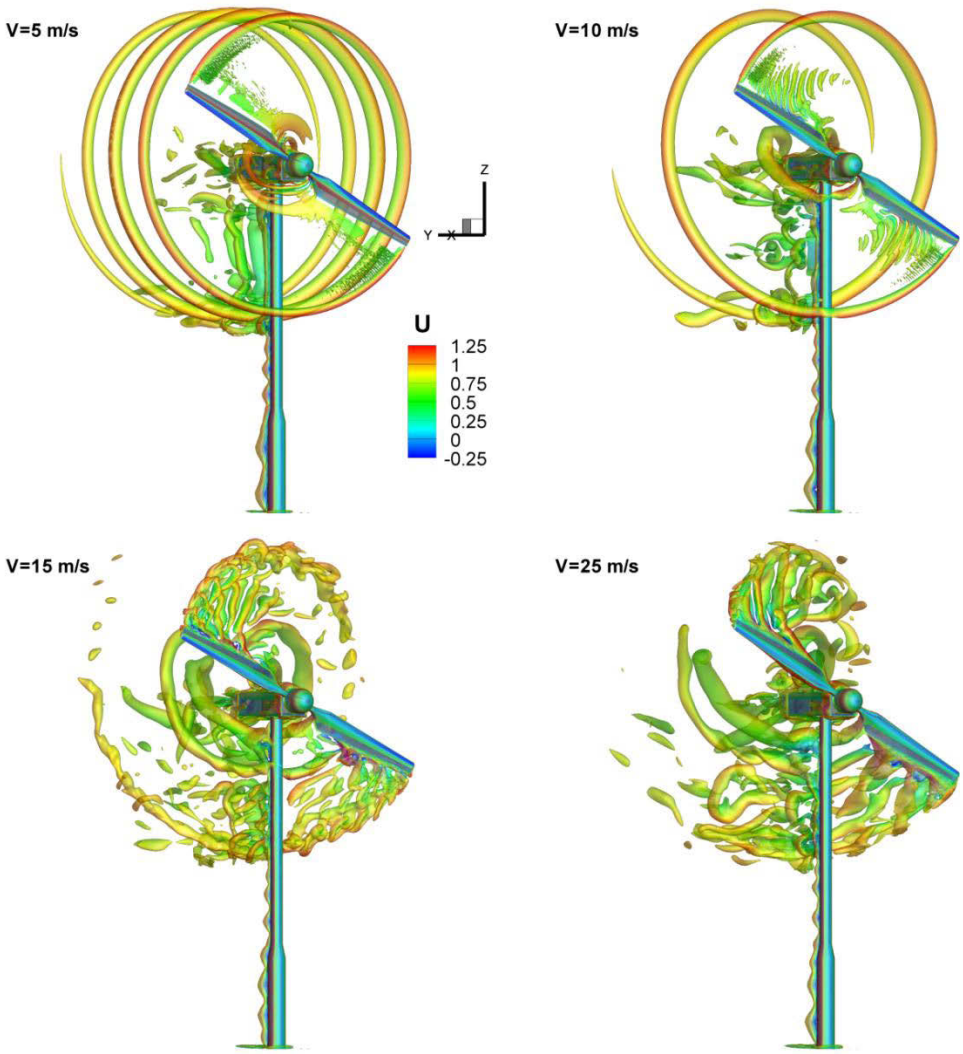

Figure 3.2 Vortical structures represented by iso-surfaces of Q=5 for different velocities (pitch angle 3 degrees)

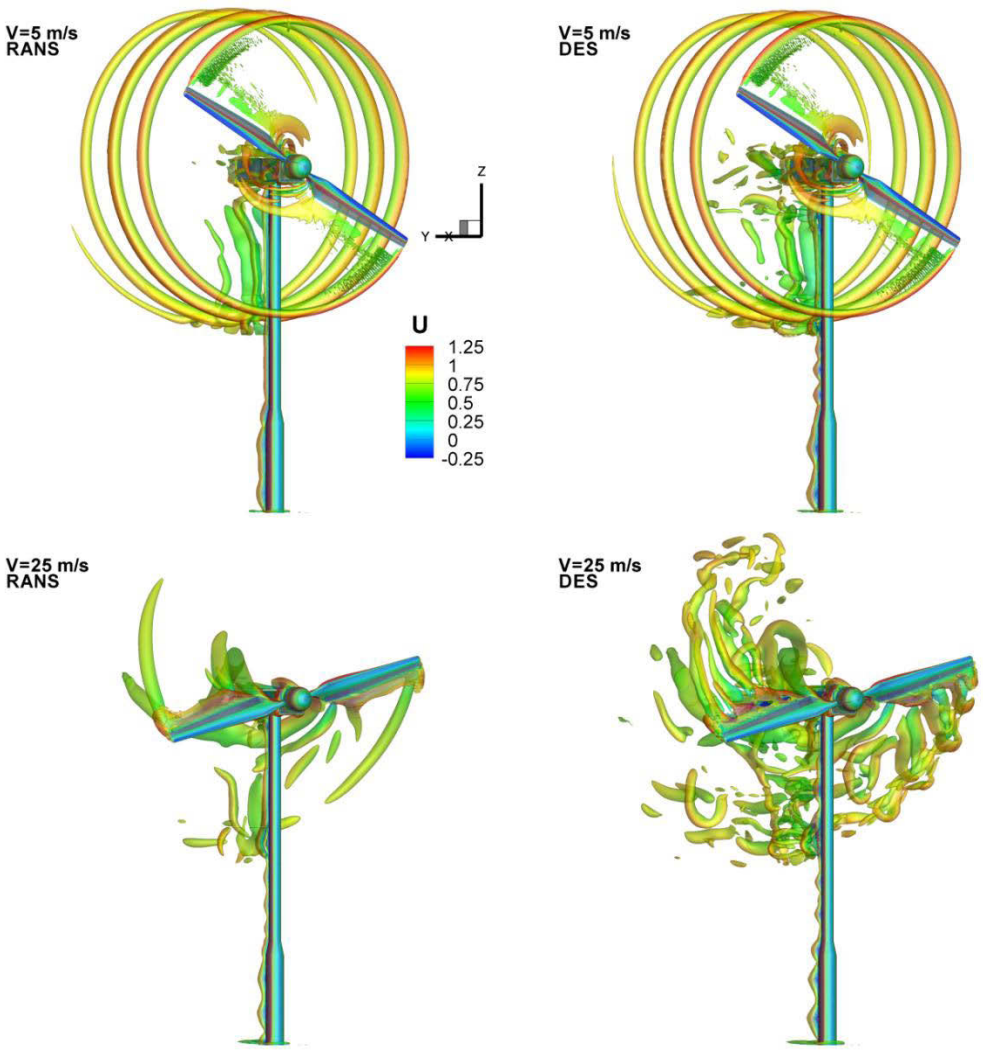

Figure 3.3 Comparison of vortical structures predicted by RANS and DES for low (5 m/s) and high (25 m/s) wind speeds. Vortical structures are represented by iso-surfaces of Q=5 (pitch angle 3 degrees)

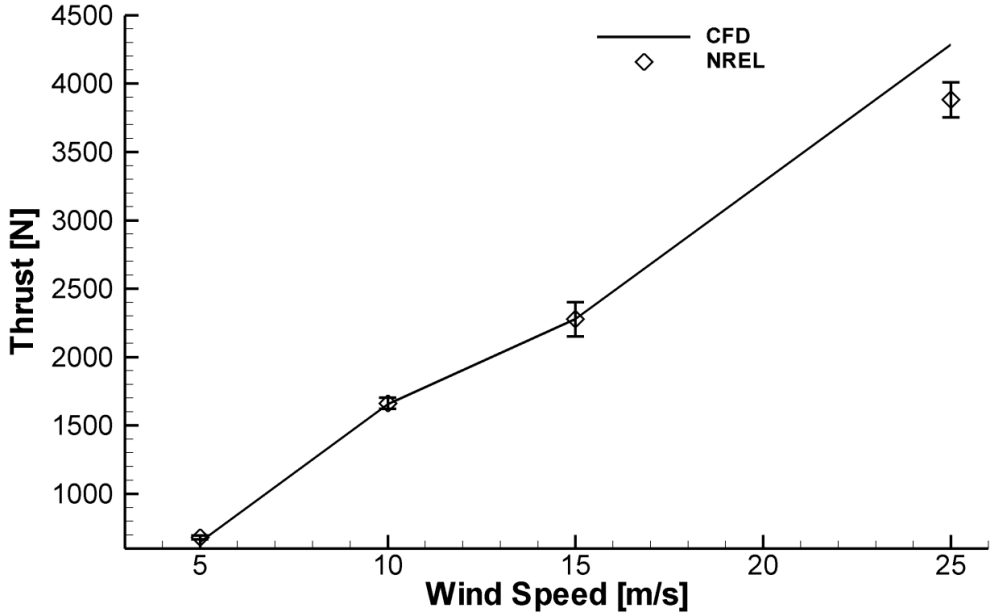

Figure 3.4 Thrust for different velocities (pitch angle 3 degrees)

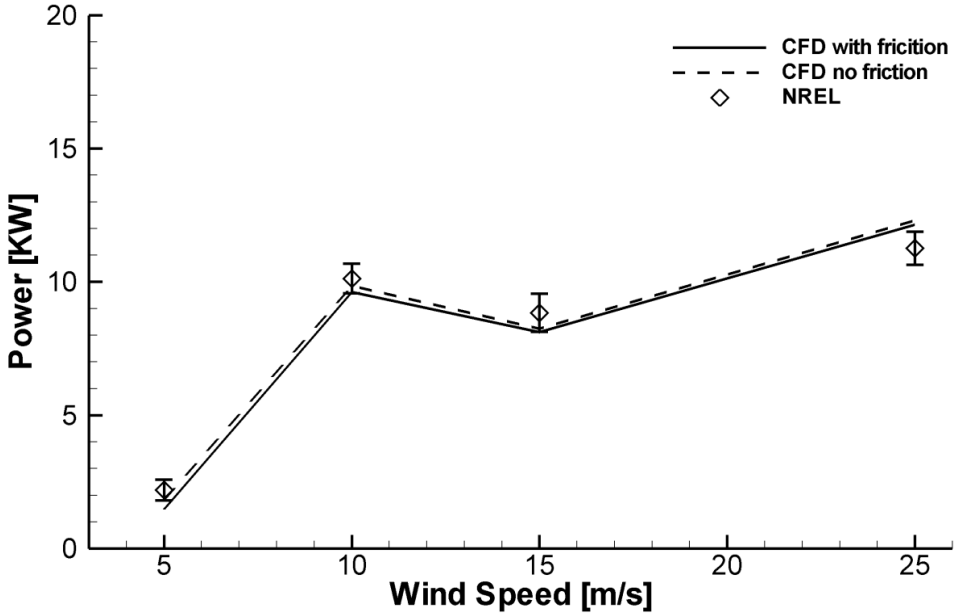

Figure 3.5 Power to the shaft for different velocities (pitch angle 3 degrees)

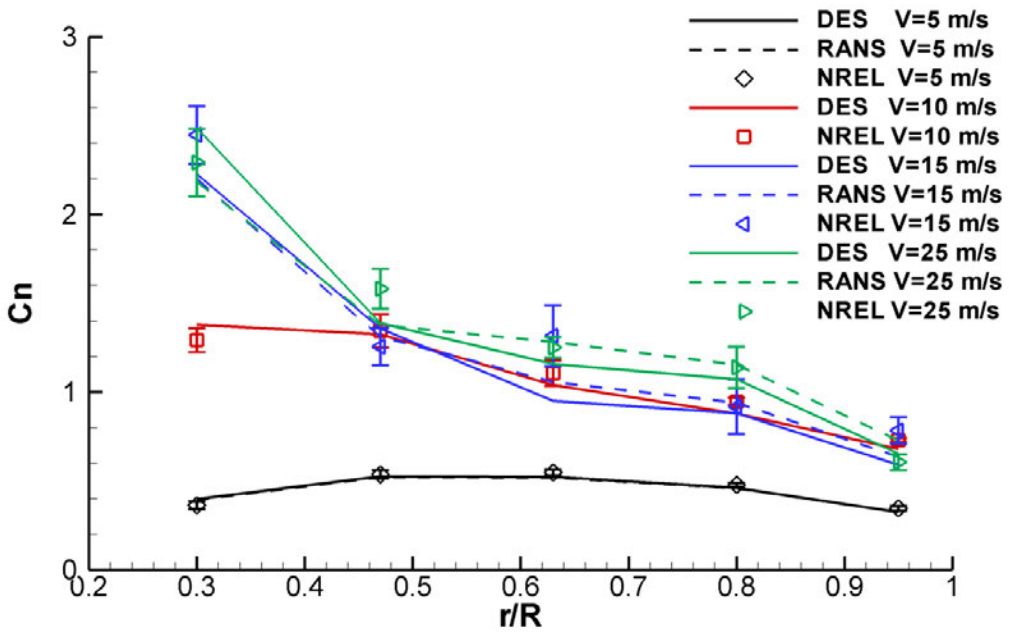

Figure 3.6 Normal force coefficients for different velocities at 5 radial sections (pitch angle 3 degrees)

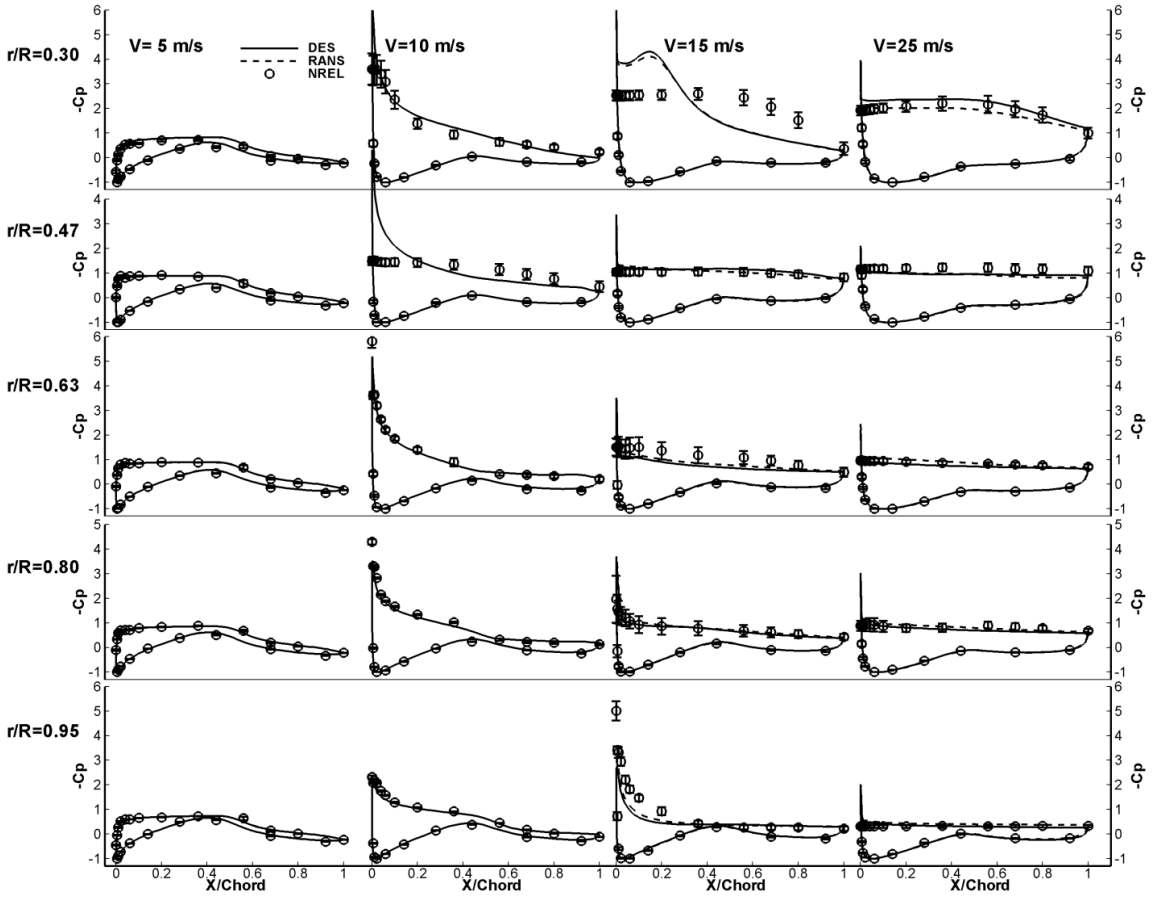

Figure 3.7 Pressure coefficient for different velocities on 5 blade sections (pitch angle 3 degrees)

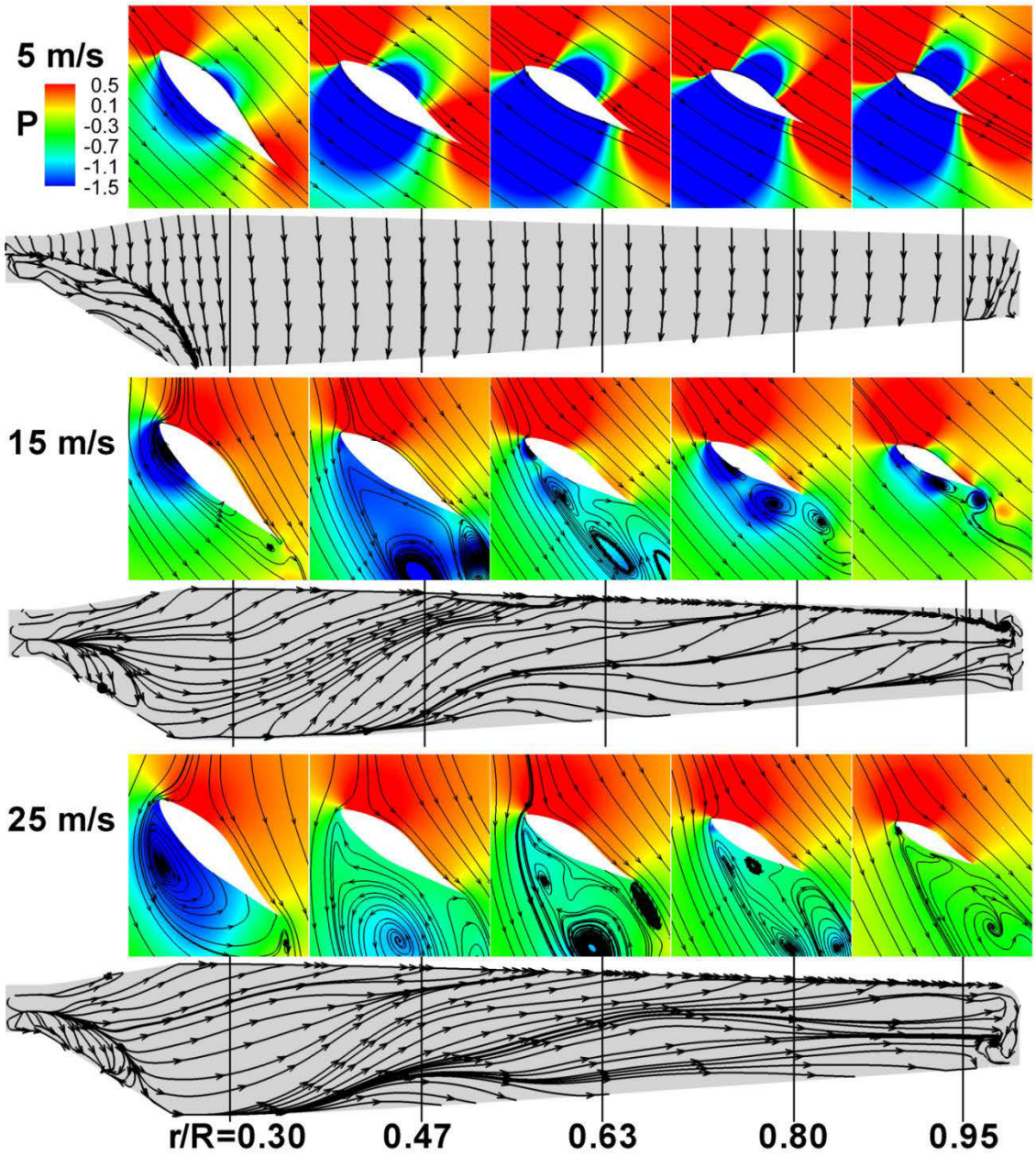

Figure 3.8 Limiting streamlines on the suction side of the blade and selected sections (colored with pressure) for 3 degrees pitch angle

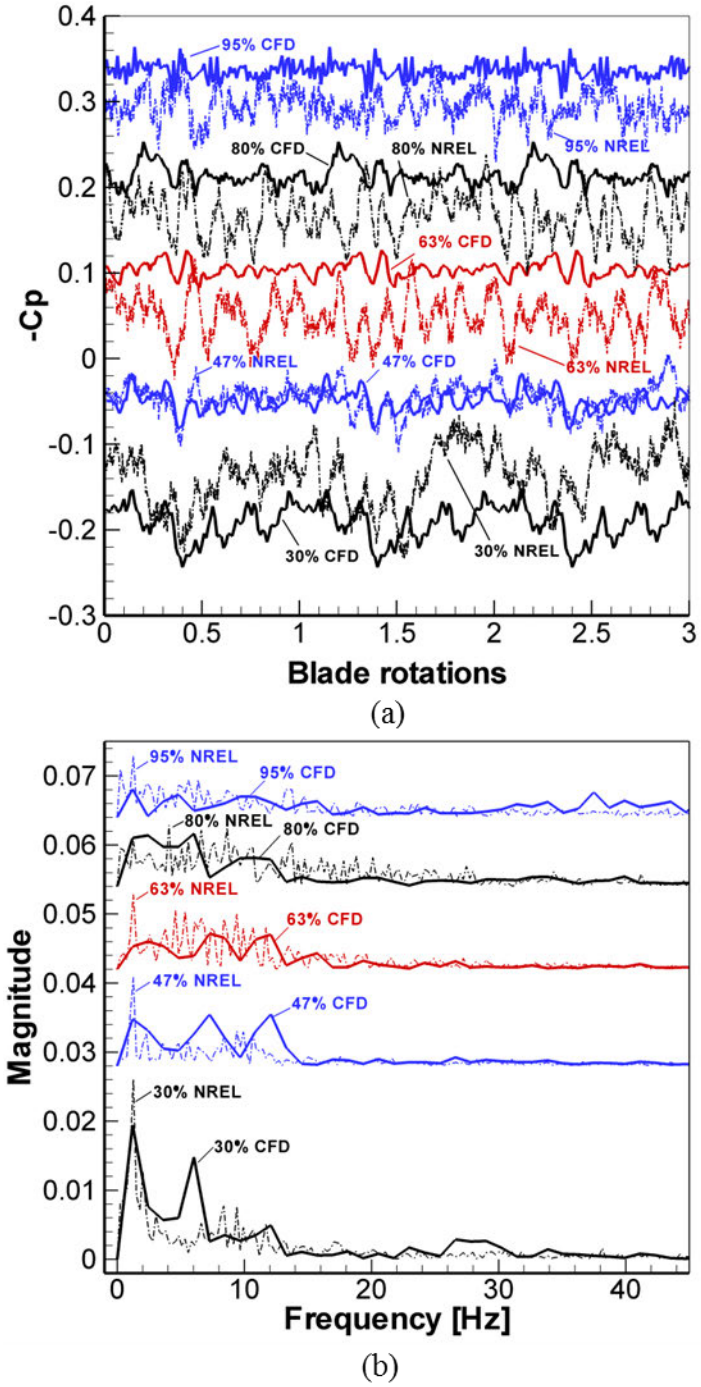

Figure 3.9 Cp on five sections for 15 m/s, 3 degrees pitch: (a) time histories, (b) FFT

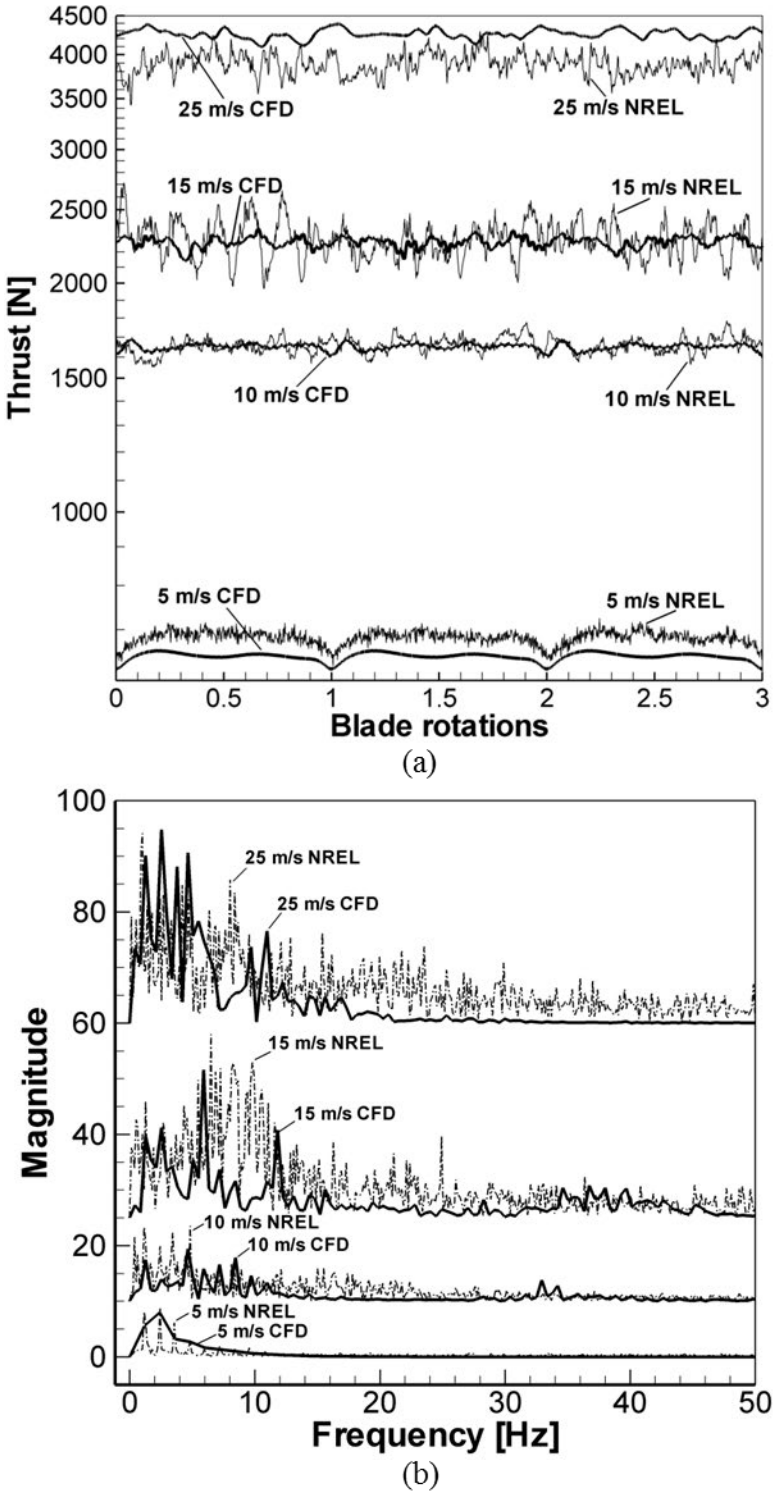

Figure 3.10 Thrust for different velocities, 3 degrees pitch: (a) time history, (b) FFT

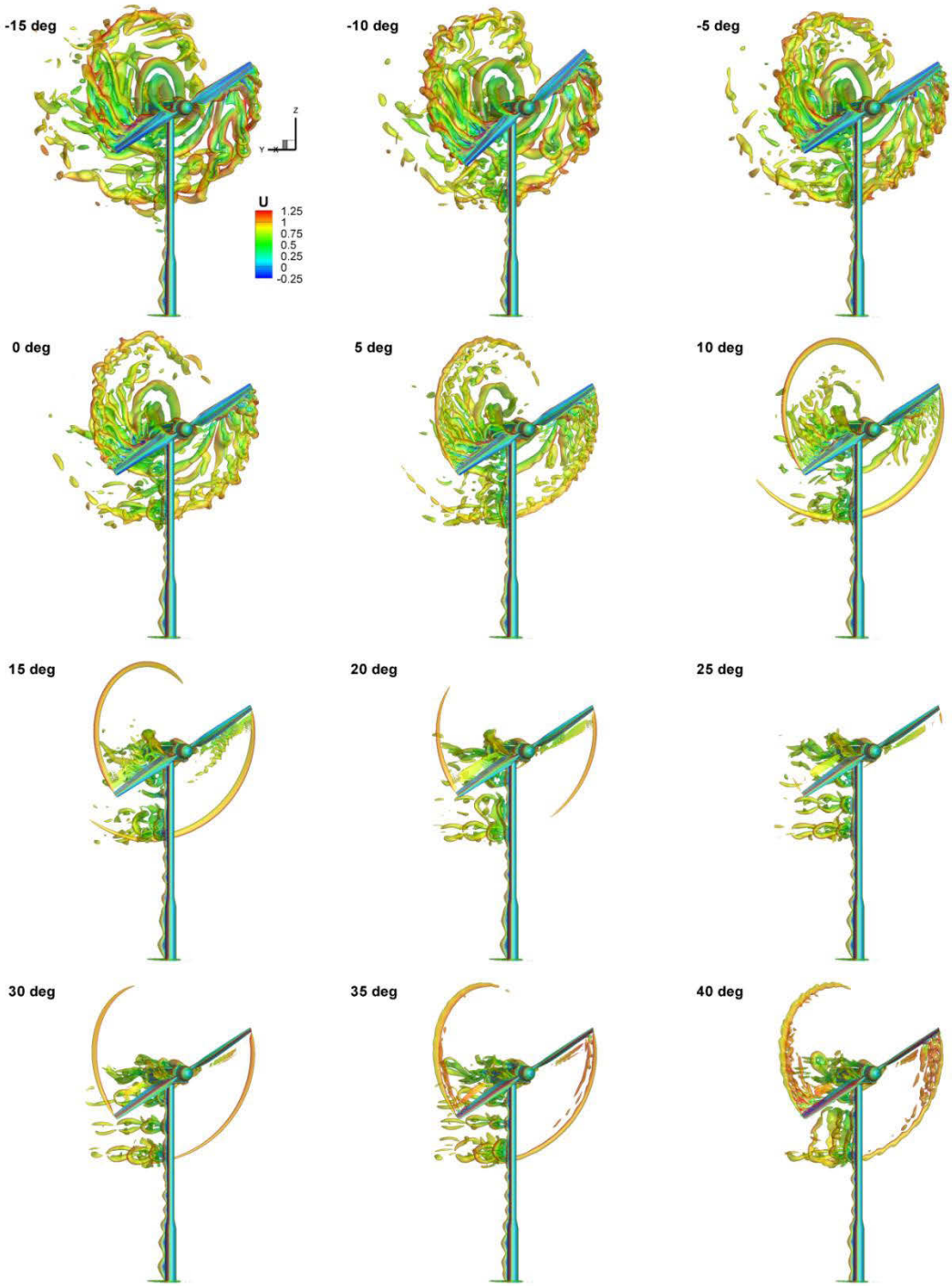

Figure 3.11 Vortical structures represented by iso-surfaces of Q=5 for different pitch angles (wind velocity 15 m/s)

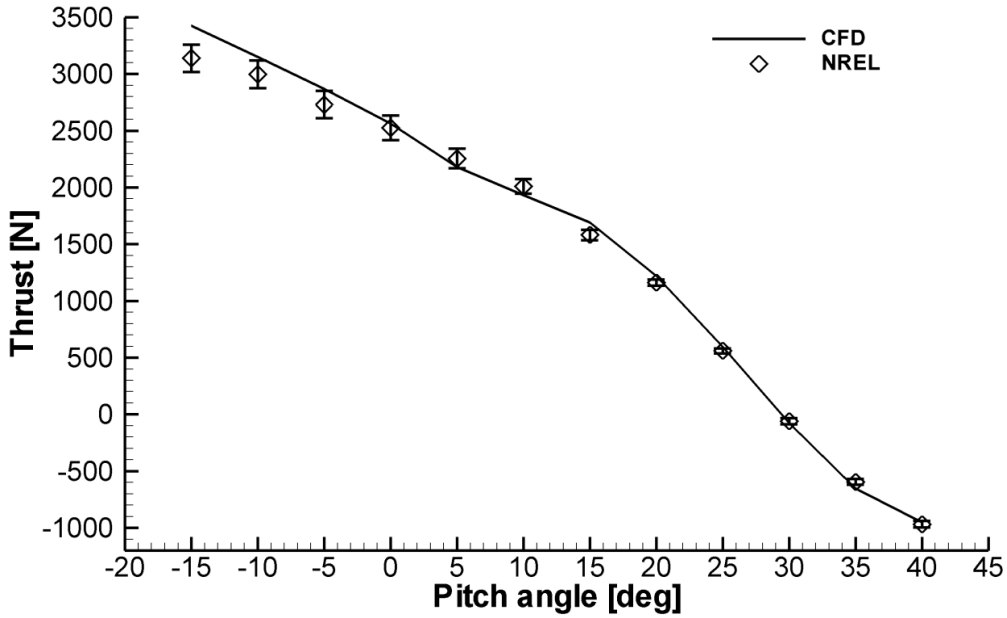

Figure 3.12 Thrust for different pitch angles (wind velocity 15 m/s)

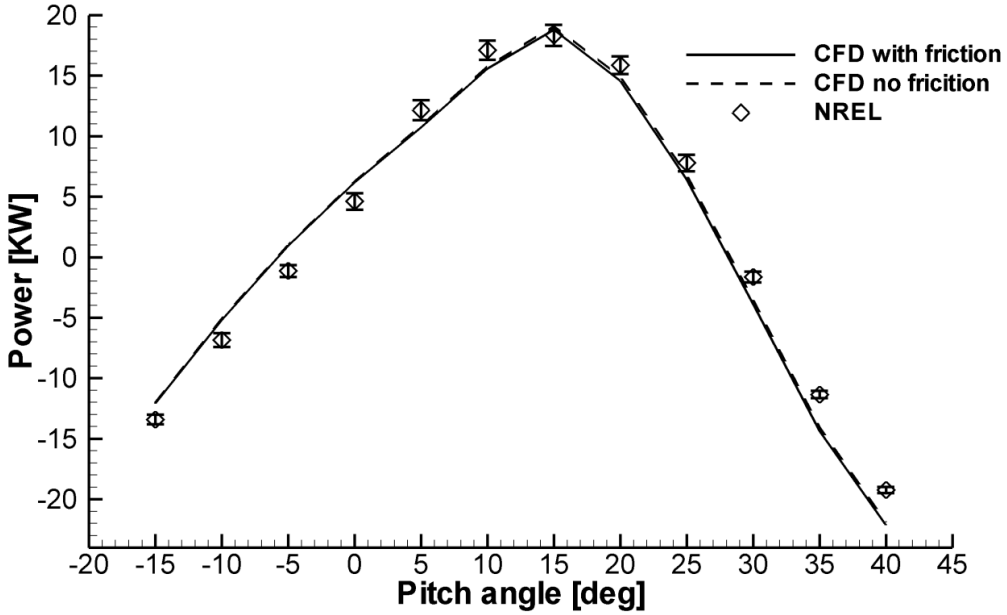

Figure 3.13 Power to the shaft for different pitch angles (wind velocity 15 m/s)

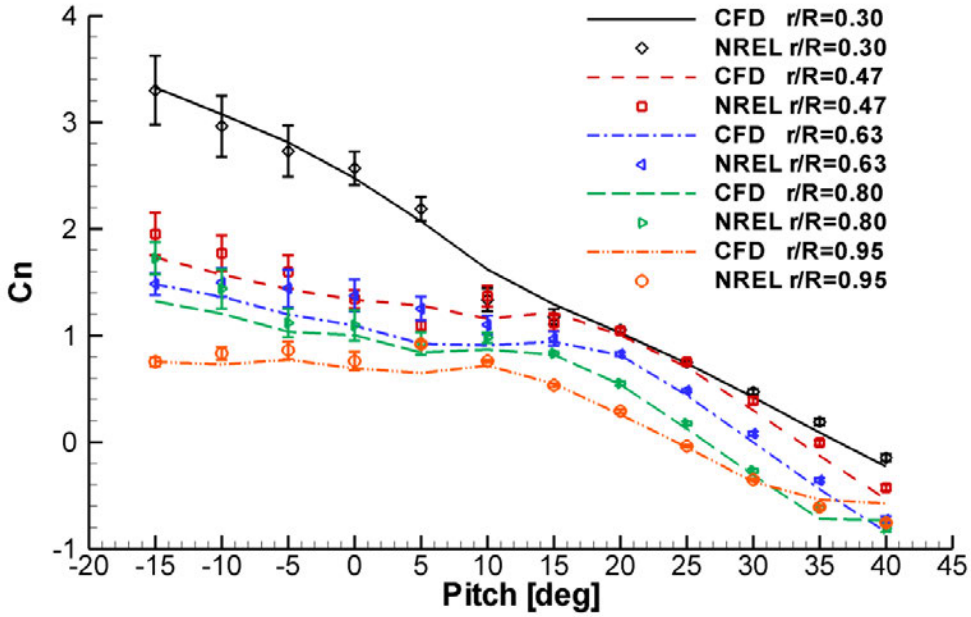

Figure 3.14 Radial normal force coefficients for different pitch angles (wind velocity 15 m/s)

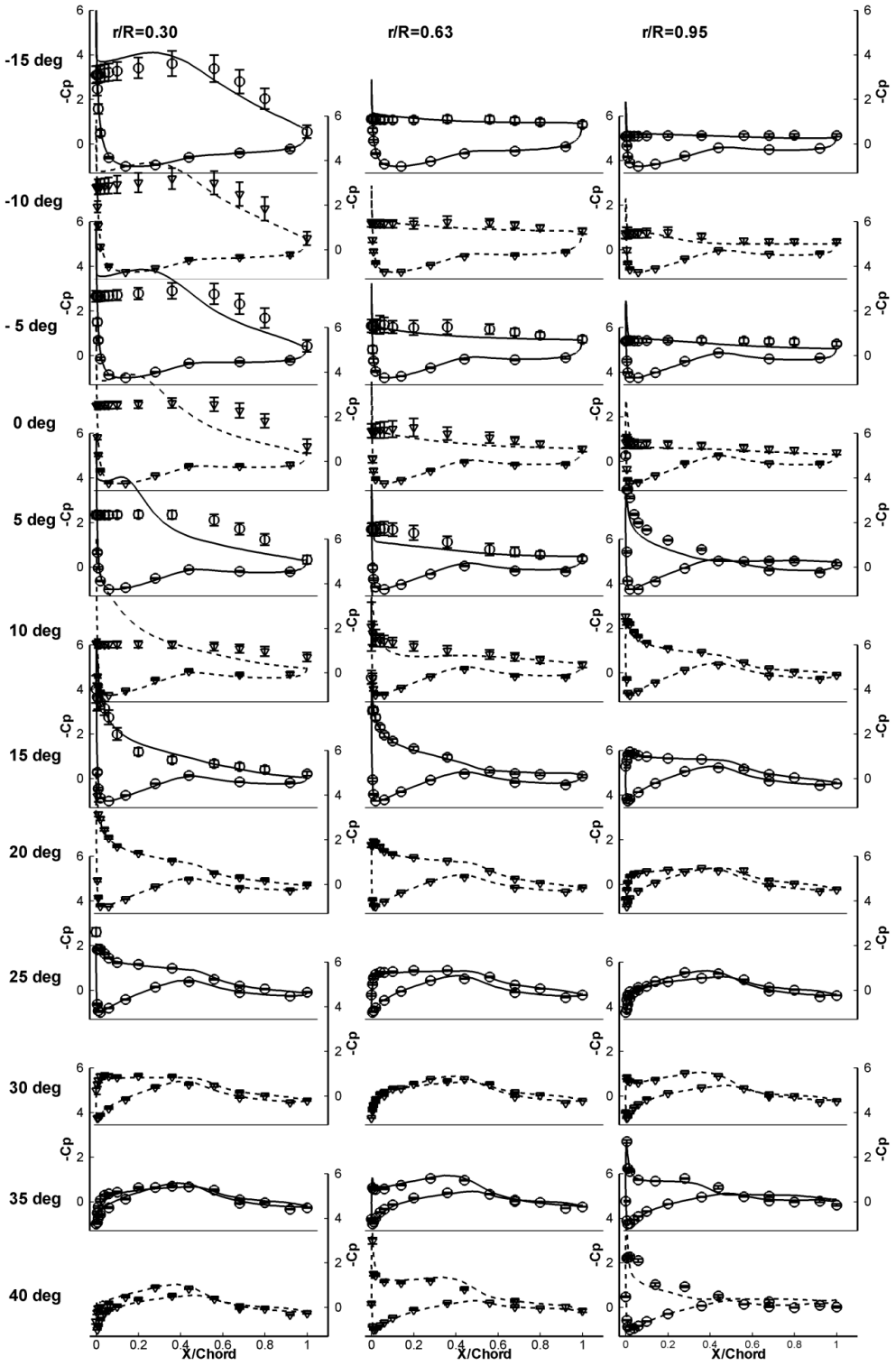

Figure 3.15 Pressure coefficients at different pitch angles and blade sections (wind speed 15 m/s, lines: CFD, symbols: experiments)

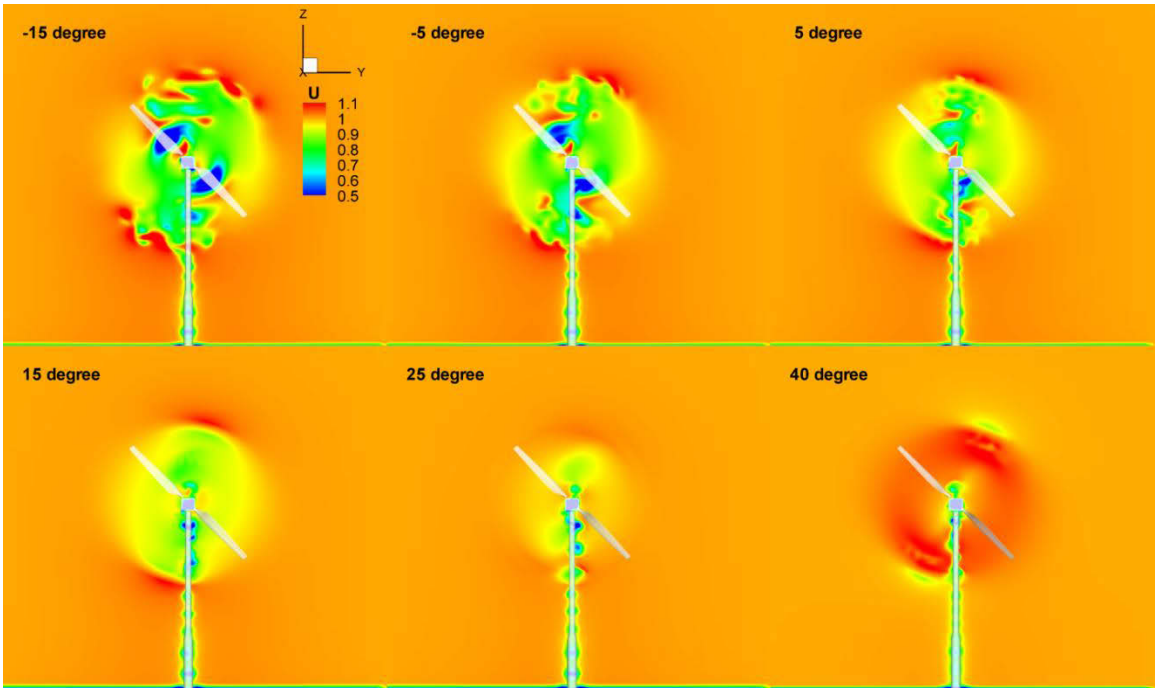

Figure 3.16 Dimensionless axial velocities at x/R=0.8 (wind speed 15 m/s)

CHAPTER 4

OFF-SHORE WIND TURBINE SIMULATIONS

4.1 Overview

Large-scale turbines place more challenges for CFD to simulate the full scale 3D turbine with long blades and high Reynolds number. In this chapter, a well-documented conceptual large-scale offshore wind turbine was used to develop and validate the proposed coupled aero-elastic approach.

4.2 Simulation Design

4.2.1 Simulation Turbine

The conceptual NREL 5MW offshore wind turbine (Jonkman et al. 2009; Jonkman 2010) is used as geometry for the simulations. Figure 4.1 and Table 4.1 show the geometry and basic properties of the turbine that consists of the baseline turbine, tower and floating support platform structure. It is a utility-scale, conventional three-bladed upwind variable-speed variable-pitch controlled turbine, and has been widely used as the reference turbine by other researchers and wind turbine industries, including the Offshore Code Comparison Collaboration project (OC3) (Jonkman and Musial 2010) and its continuation (OC4) (Popko et al. 2012). A spar-buoy type floating platform known as OC3-Hywind spar defined in (Jonkman 2010) was adopted due to its simplicity in design and modeling. Notice that the design rated tip speed of the turbine is 80 m/s, with Mach number less than 0.3, justifying the use of an incompressible code as flow solver.

4.2.2 Grid Design

Figure 4.2 shows the grid design for CFD simulations. The grid system consists of the grids defining the turbine, including accurate representations of the three blades, tips and tower/floating platform as documented in the NREL reports (Jonkman et al. 2009; Jonkman 2010), and an approximate nacelle and hub due to insufficient geometric

information for these components. In addition to the turbine grids, a Cartesian background grid is used to set for the boundary conditions, with the grids refined near the expected free surface location so that ocean wave motions can be well captured. The background grid is extended far enough in both longitudinal and vertical directions to minimize the boundary effect, and the grid spacing in the air side is designed to be fine enough to capture the wind turbulence generated by the explicit wind turbulence model. Three Cartesian blade refinement grids are used to resolve the flow around the blades, and one Cartesian air refinement grid is constructed to resolve the wake flow close to and behind the rotor. A Total of 14 grids are used with about 6.7 M grid points. The grids are organized in a parent/child hierarchy, as shown in Table 4.2. The blades, tips, hub and the blade refinements together form the body rotor that rotates around the shaft; nacelle, tower, air refinement and the body rotor form the body rotor-nacelle, allowing motions of the whole turbine under winds and waves. Though it is not included in the present simulations, another hierarchy can be constructed with body rotor and the nacelle grid forming the body rotor-nacelle while the body rotor-nacelle plus the tower grid form the body rotor-nacelle-tower, such that turbine yaw motion can be considered. In addition, a child could be added to the body rotor such that the blade pitch motion can be controlled or predicted. The dynamic overset technique is applied to re-compute the overset coefficients at run time with the code Suggar. With this approach, full control or prediction of the turbine can be realized with the rotating rotor, blade-pitch and yaw control, and motions of the floating turbine under winds and waves.

4.2.3 Multi-body System Model

The multi-body system model for the turbine consists of blades/tips, hub, nacelle and tower/floating platform as the substructures or components that are linked by the appropriate kinematical constraints at their interfaces, as can be seen in Fig. 4.3. Each turbine component comprises one or several rigid bodies connected by the relevant

connections. The structural properties of each component include mass and center of gravity, flap-wise, edge-wise, torsional and extensional section stiffness, as well as flap-wise and edge-wise section inertia. Construction of the model follows the structural information specified in the NREL reports (Jonkman et al. 2009; Jonkman 2010). The structural model of the turbine consists of 6 components: 3 blades, nacelle, hub, and tower/floating platform. Each blade component comprises of 48 bodies, the tower/floating platform component has 11 bodies, and the nacelle and hub only contain 1 body each. In total the turbine multi-body system has 157 bodies. Bracket joints are used as the connection in all components for the rigid turbine simulations to prevent any relative motion between two bodies, while beam force elements are used as connections for the flexible turbine simulations, allowing 6 degrees of freedom (6 DOF) for each body. For the kinematic description between turbine components, appropriate kinetic joints or constraints are applied: each interface of the blade and hub is connected by the bracket joint, restraining relative motions between the components; a revolute joint is used between the hub and nacelle along the rotational axis of the rotor to allow rotor rotation and constrain other DOFs; similarly, another revolute joint is used at the interface of nacelle and tower for the yaw motion.

4.2.4 Simulation Cases

Considering the sophistication of wind turbine aero-hydro-servo-elastic simulations, the test cases were chosen with incremental level of complexity from the publicly available OC3 results (Jonkman and Musial 2010), to include rigid and flexible turbines with or without wind turbulence. Several revisions for each simulation case performed independently by a group of international participants from universities, research institutions and industries with expertise in wind energy makes the OC3 project a good benchmark for the utility-scale offshore wind turbine.

The simulation matrix from OC3 phase I was simulated, excluding the water/wave effects. Simulations results of two participants from OC3 that both use the BEM-based aerodynamic code AeroDyn (Laino et al. 2002) as aerodynamic solver but different MBD-based structural solvers, FAST (Jonkman and Buhl Jr. 2005) and Bladed Multibody were compared (Hereby called NREL FAST and GH Bladed). Table 4.3 summarizes all cases evaluated, where rigid turbine simulations are named 2.x and flexible turbine simulations are labeled 3.x. The simulation matrix includes cases with moderate wind condition with the mean hub height wind speed of 8 m/s and rotor speed of 9 RPM, rated wind condition with mean hub height wind speed of 11.4 m/s and rotor speed of 12.1 RPM, uniformly distributed wind profile, wind shear with log-law wind profile, wind turbulence, rigid and flexible turbine. For the wind turbulence, a box of $256 \times 128 \times 128$ points was used with length increment $\Delta L = 10\ m$ for Mann's model, generating a turbulence field with dimension of $2560\ \text{m} \times 1280\ \text{m} \times 1280\ \text{m}$. Reference turbulence intensity is 0.14, a medium turbulence level and is consistent with the OC3 simulation conditions.

While all simulation in this chapter are performed at constant rotational speed, only case 2.1a in OC3 involves a constant rotor speed, as shown in Table 4.3 and Table 4.4. The simulation case with constant rotor speed of 9 RPM at wind speed of 8 m/s for rigid turbine was to serve as the basic and simplest validation case in OC3 project, and complexity was gradually added to include the turbine control system, flexibility and wind turbulence. For wind speed below the rated wind speed of 11.4 m/s, variable rotor speed controller with fixed blade pitch was applied to maximize turbine efficiency, and variable pitch controller with regulated rotor speed was applied for wind speeds beyond the rated wind speed so as to maintain a constant rated power and regulate the generator speed. One example can be found by comparing cases 2.1a and 2.1b at wind speed of 8 m/s, where NREL FAST determined that a rotor speed of 9.3 RPM was optimal while GH Bladed obtained 9.1 RPM. Detailed discussion is included in the following sections.

4.3 Results and Discussion

4.3.1 Mann Wind Turbulence Model Predictions

The validation of the explicit turbulence model is conducted in two steps: first the generated Mann box is validated by comparing with the theoretical isotropic one-point spectrum; then in step 2 a CFD wind turbulence simulation for an open field (i.e. no wind turbine) is conducted with the applied Mann wind turbulence model as inlet boundary and initial conditions. Statistical comparison is made to show the validity of the implementation. To compare the isotropic one-point spectrum, the parameter (Γ) to control the anisotropic wind fluctuations is set to 0 and thus the model reduces to isotropic wind turbulence. In addition, the mean prevailing velocity is set to 0 for convenient comparison. In step 2, all parameters were set appropriately to include anisotropic and sheared wind turbulence, while mean velocity of 8 m/s was used in the prevailing wind direction, resulting in a total simulation time of 320 s. The CFD grid for this simulation consists only of the same background grid used for turbine simulations.

Figure 4.4 shows a Mann's turbulence box with slices colored with the axial velocity. The distribution of the velocity fluctuations is random in space, with velocities mostly within ± 1 m/s and the largest wind fluctuations reaching ± 3 m/s sparsely distributed in the box. Figure 4.5(a) shows the time history of velocities fluctuations at the point that corresponds to the position of the turbine hub. From Taylor's frozen hypothesis, the spatial information in the axial direction x is related to temporal information, and thus velocities at a point in the box moving in the x-direction is interpreted as velocities at a fixed point in space over time t. Since the turbulence is isotropic with zero mean velocity, all other points should have similar behavior. As can be seen in Fig. 4.5(a), all velocities fluctuate within ± 3 m/s with zero net velocity, but no similar or periodic pattern exists for the three velocity components in time. Statistics for all points in the box show zero mean velocity and unit variance. In addition, Fig. 4.5 (b)

shows a comparison of the one-point spectrum computed using the parametric spectral estimation method by Burg (Marple Jr 1987) and the theoretical one-point spectrum as defined in Eqs. (2.25) and (2.26). It can be seen that the spectra for the three velocity components from the Mann model compare well with the theoretical curves. Due to the finite size of the Mann box and the cell, there are truncations in the calculated spectrum for low wave number (limited by the size of the box) and for large wave number (limited by the size of the cell).

Since the turbulence is introduced as initial and boundary conditions, there is a decay of turbulence in time, seen as a decay with position in the CFD computation. This expected phenomenon in a viscous computation has been observed by Larsen (2013), and is alleviated using a turbulence scaling factor (SF) in the Mann model, which is calculated based on the actual variance level in the box and the target longitudinal turbulence standard deviation $\sigma_{1,\text{target}} = \sigma_{\text{iso}}/0.55$ based on the requested turbulence intensity, such that $\text{SF} = \sigma_{1,\text{target}}/\sigma_{1,\text{box}}$ multiplies all velocity fluctuations. Figure 4.6 shows demonstrations of the evolution of the turbulent wind field with the visual assistance of vortical structure represented by Q = 1 contoured with non-dimensional axial velocity. It can be seen that massive wind turbulence was generated at the inlet due to the explicit turbulence model, and has dissipation as it develops downwind, which is mainly due to the fact that no turbulence is produced to balance the dissipation in the rest of the simulation domain except at the free surface. The vortical structures close to the free surface (shown with a blue line in Fig. 4.6) are thin, long and stretched. Note that grids are refined in this region to capture highly turbulent flow field. Since the water is still in this simulation, the free surface is a no-slip wall to the wind, causing turbulence due to shear.

Figure 4.7 shows the time history of turbulent velocities for 4 points located at approximately hub height and center of the turbine ($y = 0$ m and $z = 90$ m) and at different non-dimensional axial locations including the inlet of the simulation domain,

right in the position of the turbine at $x = 0$ and further downstream to the exit of simulation domain approximately at $x = 5$. Recall that all spatial dimensions are non-dimensionalized by the rotor radius R. It can be seen that for all locations the 3 velocities components fluctuate randomly around their expected mean velocities, 1 for u and 0 for v and w. The figure essentially shows that the turbulent field solved by CFD with the explicit wind turbulence at the inlet is appropriately transported through the whole simulation domain throughout the simulation, but turbulence decay due to viscous losses mentioned previously is observed, as velocities closer to the inlet tend to have larger fluctuations than more downstream locations.

Figure 4.8 shows mean and standard deviation of the velocities on vertical and horizontal transects crossing the turbine hub. The mean velocity is maintained in $\boldsymbol{u} = (1,0,0)$ while the standard deviation for u (σ_1) satisfies the requested reference turbulent intensity of 0.14 for axial velocity, and standard deviations for v (σ_2) and w (σ_3) are about 0.1 and 0.08, respectively, satisfying the requirements by the IEC standard that $\sigma_2 \geq 0.7\,\sigma_1$ and $\sigma_3 \geq 0.5\,\sigma_1$. Note that velocities at inlet have larger standard deviations than other axial positions, with approximately 0.18, 0.12 and 0.09 for σ_1, σ_2 and σ_3, respectively, due to the introduction of the turbulent scaling factor.

4.3.2 Aerodynamic Predictions

Case 2.1a provides a good scenario to compare results of the CFD approach presented herein (from now on called the CFD approach or simply CFD) against the widely used aerodynamic solver AeroDyn under fixed operational conditions without controller. For all performed simulations with CFD, at the initial time step blade 1 was placed downward right in front of the tower, and thus at every complete rotation blade 1 is passing the tower while half rotation later is at the uppermost position. Turbine rotation is counter clock-wise when seen facing downwind. Figure 4.9 shows a comparison of the time history of thrust and torque once the periodic behavior has been reached for wind

speed of 8 m/s, and Table 4.5 quantitatively compares statistics. As can be seen in Fig. 4.9, both CFD and the OC3 results predict similar trends for thrust and torque for the rigid turbine under uniformly distributed wind. Being a 3-bladed turbine, a decrease in thrust and torque occurs every 1/3 rotation due to the presence of the tower. Using GH Bladed as baseline, quantitative comparisons in Table 4.5 show that the CFD approach has close predictions to both NREL FAST and GH Bladed. For thrust, CFD predicts an average value of 389 KN with standard deviation of 2.7 KN, 4.5% larger than GH Bladed, while NREL FAST predicts average thrust of 385 KN with standard deviation of 2.6 KN, 3.4% larger than GH Bladed. For torque, CFD shows an average magnitude of 1946 KN m with standard deviation of 27.5 KN m, while NREL FAST predicts an average of 2096 KN m with standard deviation of 27.4 KN m, 1.5% lower and 6.1% higher than GH Bladed, respectively. Beside the good agreement for averaged magnitudes, all three methods exhibit similar statistics for this case, including maximum, minimum and standard deviation of the thrust and torque. Notice that NREL FAST and GH Bladed share the same aerodynamic code, and yet a difference of 3.4% is reported for thrust and even a larger 6.1% difference for torque. As pointed out in the OC3 final report (Jonkman and Musial 2010) "certain differences were apparent in the aerodynamic blade-load calculations" with "differences in the mean magnitude of rotor torque of about 5%" for all participants. Regarding this fundamental test, CFD shows good agreement with both methods.

Further investigation of the individual blade loads is beneficial to explain and understand the aerodynamic behavior of the rotor and quantify the effects of the tower shadow and tilt/precone angle. Figure 4.10 shows the time history of thrust and torque for blade 1. The loads experienced by the blades show periodic oscillations, with a sharp drop of 6.3% in thrust and 10.6% in torque every time the blade passes by the tower. The tilt causes a lower relative velocity of the wind with respect to the blade when the blade is rotating from bottom to top, and the opposite when the blade is coming back down from

top to bottom. This effect is caused by the tip of the blades moving back and forth in the axial direction as they rotate. The consequence is fluctuations in thrust and torque with approximately 2% and 5% amplitude, respectively.

4.3.3 Effect of Elasticity

Case 3.1 was designed to test aero-elastic capabilities of the simulation codes by OC3. However, as mentioned in the simulation cases section, OC3 simulations have a variable-speed controller, which is not included in this chapter's CFD simulations. An analysis is conducted here to estimate the influence of the controller before comparing results with elasticity. The control algorithm seeks for the maximum efficiency, with the rotor speed adjusted at run time and resulted in around 9.3 RPM for both the rigid and flexible turbines by NREL FAST and 9.1 RPM by GH Bladed. These results in significant decreases in standard deviation for the power, by a factor of 9 for NREL FAST and 6 for GH Bladed, see cases 2.1a and 2.1b in Table 4.4. The turbine can then be operated with more stable power output. Increasing the rotor speed at constant wind increases tip speed ratio and thus usually helps to improve efficiency. However, the torque decreases slightly for the case with controller, by 3% for NREL FAST and 1.4% for GH Bladed. The thrust increases about 2.5% for NREL FAST and 0.8% for GH Bladed. In this case of moderate wind speeds, higher rotor speed results in larger thrust and smaller torque for the flexible turbine.

Figure 4.9 and Table 4.5 show turbine thrust and torque for rigid and flexible blades and tower. Comparing with its rigid turbine counterpart, the CFD approach predicts an increase of 3.5% for average thrust and 0.6% decrease for torque, in close agreement with cases 2.1b and 3.1 for the OC3 results. For the flexible turbine the mean magnitude of thrust predicted by CFD is 6.3% higher than results from GH Bladed, while NREL FAST predicts 8% more than GH Bladed. The average torque is 0.5% lower than GH Bladed, and NREL FAST is 4.5% higher. Due to the lack of a controller, the standard

deviation predicted for the loads by CFD are much larger than those in OC3 participants. Since the OC3 results deviated from the nominal rotor speed of 9 RPM due to the use of the controller, as discussed in the previous paragraph, the differences between OC3 participants and the CFD results could be higher or lower than those reported in this study.

Loads for the individual blades for the rigid and flexible cases are shown in Fig. 4.10. Neglecting the effect of the tower, which causes a sudden drop in thrust and torque when the blade is at the bottom, there is a minimum in loads when the blade is approximately at the top, and a maximum when the blade is approximately at the bottom. This behavior can be explained in terms of changes in the angle of attack due to flow and geometry, as discussed below in reference to Fig. 4.12.

Classical BEM characterizes the airfoil sections in terms of parameters describing local flow and forces. These include the sectional angle of attack (AOA), axial induction factor (a) and tangential induction factor (a'), lift (C_l) and drag (C_d) coefficients, normal (C_n) and tangential (C_t) coefficients. CFD results can be inspected to obtain these airfoil parameters, though the definition of some of them makes evaluation somewhat ambiguous. Figure 4.11 shows the streamlines at 4 different spanwise sections of blade 1 colored by dimensionless axial velocity, exhibiting streamlined flow on all sections except near the root. Flow velocities were transformed to the blade system as seen by the airfoil section. The AOA is defined as the difference in angle between the chord of the airfoil and the flow direction far upstream of the airfoil. Use of the velocity far upstream of the airfoil would be inappropriate since it would not contain the induced flow in the axial and tangential directions. Using the velocity too close to the airfoil does not work either, since the influence of the airfoil affects the streamlines and causes errors in the AOA. Necessarily, a compromise needs to be made to estimate the flow direction so that represents the flow impacting the airfoil but not overly affected by it. Similarly, the induction factors are computed from velocities obtained from CFD and the location of the

points selected to compute the velocities used to estimate the induction factors affect the results. In light of this, the AOA and the induction factors have to be considered a qualitative estimate to evaluate behavior and trends.

The average axial velocity over a set of points approximate half chord length around the foil is used to compute the axial induction factor a. Of those points, only the points on the suction side are used to compute the tangential induction factor a', and a few points close upstream of the airfoil on the leading edge are used to evaluate the AOA. The force coefficients C_l, C_d, C_n and C_t are computed evaluating forces on a section of the foil and using the same velocity used to compute the AOA. The computations are conducted in the airfoil system of reference, so transformations are applied to project velocities from the earth reference system, where velocities are computed by CFD, to the blade reference system. These transformations account for yaw, tilt, precone, and rotor angle.

Figure 4.12 shows time histories of the AOA, a and a' for blade 1 at 5 selected radial positions for wind speed of 8 m/s. The presence of the tower is clear when the blade is on the bottom (integer number of rotations) by an increase in axial induction factor and decrease in angle of attack. Since the tilt moves the blade downstream when moving from bottom to top, the incoming wind velocity in the airfoil system of reference decreases as the blade moves from bottom to top and increases when moving from top to bottom. At the same time, when the blade is at the top it is immersed deeper into the wake, resulting in lower axial velocities. As a consequence, for all sections with $r > 0.5R$, the AOA has a trough in uniform wind approximately when the blade is at the top and a high when it is on the bottom. The axial induction factor is highest when the blade is at the top and a minimum for the blade on the bottom, approximately $a_{max} = 0.4$ and $a_{min} = 0.33$ at $r/R = 0.93$. At most sections the AOA is below 10^o, $0.28 < a < 0.4$ and $a' < 0.1$, indicating operation of the turbine close to design point.

For uniform wind, a flexible blade results in slightly higher AOAs, a lower induction factor for sections closer to the shaft and a higher induction factor near the tip. The higher axial induction factor near the tip of the blade is expected as the blades deform and gets deeper into the wake. Due to deflections, the blade twist decreases a small amount close to the root to about 1 degree in average at the tip, resulting in larger AOAs for flexible blades.

The trends seen in AOA and a determine the blade load behavior shown in Fig. 4.10. The blade thrust is the integration of the differential normal force $F_n = C_n \times (1/2\ \rho V_{rel}^2 c)$, where C_n is the normal force coefficient, V_{rel} is the relative velocity seen by the airfoil and c is the chord length. For AOAs below stall, C_n is approximately proportional to AOA, while ignoring tilt and precone $V_{rel}^2 = (V_0(1-a))^2 + (\omega r(1+a'))^2$. Examining Figs. 4.10 and 4.12, the increase in AOA for a flexible turbine results in larger C_n than for a rigid turbine, with consequent higher thrust. In addition, AOA and $(1-a)^2$ determine the trend of F_n and thus the blade thrust, showing periodic oscillations with primary trough when blade is at the top and secondary trough when it is close to the tower, peaking approximately 0.1 rotation before and after passing the tower.

Figure 4.13 shows the average and standard deviation of the pressure coefficient C_p for the rigid and flexible turbines at 5 different radial sections. The section at $r/R = 0.16$ is very close to the root and in the transition from cylindrical to airfoil section. From 60% chord to the trailing edge, C_p at the pressure side is slightly smaller than at the suction side, indicating that in that portion of the section the lift coefficient is negative. At the same time, this section also shows large lift coefficient from 0 to 60% chord. However, the strong adverse pressure gradient after 20% chord is an indicator of possible flow transition and separation. This is consistent with the high AOA shown for that section in Fig. 4.12. Standard deviations for C_p at this section are large, further confirming the unsteadiness and separation. All other sections show standard behavior of attached flow, with small standard deviation and moderate pressure gradients on the

suction side. Note that pressure coefficients for the elastic and rigid turbines have almost identical trends.

Figure 4.14 shows radial distribution of average and standard deviation of the normal and tangential coefficients C_n and C_t for the rigid and flexible turbines. Since the structure is very rigid close to the root, there is no significant difference between rigid and flexible results, but differences are apparent for higher r/R for C_n. C_n is essentially flat with mean magnitude around 1.0 for $0.6 < r/R < 0.8$, where most of the torque is produced, while the flexible turbine gradually increases from 1.0 at $r/R = 0.6$ to 1.1 at $r/R = 0.8$. The losses at the tip are clear for both rigid and flexible turbine, but the flexible turbine shows larger C_n. This explains the large difference for the blade thrust between rigid and flexible blade as shown in Fig. 4.10. C_t exhibits less differences between rigid and flexible results, consistent with the torque behavior shown in Fig. 4.10.

When the AOA changes, vortices are shed from the airfoil leading edge. Because of the interaction of the vortices with the flow, and the travel time of these vortices along the airfoil surface, there is a time lag between changes in the AOA and the aerodynamic loads (Fuglsang et al. 1998). Figure 4.15 shows C_l and AOA over two rotor revolutions for the rigid (Fig. 4.15a) and flexible (Fig. 4.15b) turbines. The standard angle of attack-lift coefficient curve is shown in Fig. 4.15c. As shown in Figs. 4.15a and 4.15b, both rigid and flexible turbines display a small delay between C_l and AOA. Figure 4.15c shows primarily a counter clockwise path in all sections. When the blade rotates from the top and approaches the tower, a secondary counter clockwise path is formed as the blade passes the tower shadow. Paths for the rigid and flexible turbines stay close at inboard sections, but then gradually depart from each other, as can be seen in the partially intersected loops at $r/R = 0.55$ and fully separated at $r/R = 0.93$. The drag coefficient C_d, from Fig. 4.16, shows similar trends as the lift coefficient, with the particularity that C_d in the section $r/R = 0.16$ is about 10 times higher than at other sections, due to the

much thicker geometry of the airfoil in the root/airfoil transition region, and also exhibiting significant fluctuations as observed for the lift.

Figure 4.17 and Table 4.6 compare the predicted blade 1 tip deflections from CFD and by OC3 participants. The deflections are respect to the coned coordinate system that rotates with the rigid rotor. Positive out-of-plane (OoP) deflection points downwind in the coned coordinate system, positive in-plane (IP) deflection points from leading edge to trailing edge, opposite to the blade rotational direction. Due to the rotational and tilt effects, all blade deflections exhibit cyclic oscillations.

OoP deflection is important since it is related to the structural strength and fatigue of the blade, and to tower clearance issues. Since thrust is the largest contributor to the OoP tip deflection, the predicted deflection follows similar trends as those observed and discussed in Fig. 4.10 for blade thrust. The primary trough occurs approximately when blade is at the top with the least influence from gravity, and the secondary trough is induced by the tower shadow with mean magnitude of about 3.5 m. If the tower was not present, the deflection would keep increasing to a maximum value with the blade on the bottom where the gravity effect is maximum due to the tilt and precone angle. As a consequence, the tower shadow contributes to increase the blade/tower clearance. As seen in Table 4.6, CFD shows OoP mean deflection of 3.592 m, while NREL FAST and GH Bladed predict averaged deflections of 3.244 m and 3.011 m, respectively. The maximum deflection is 3.692 m for CFD, 3.37 m for NREL FAST and 3.149 m for GH Bladed.

For the In-Plane (IP) deflections, all three methods predict essentially sinusoidal patterns, determined mainly by centripetal force, blade rotation and tilt effects, but dominated by gravity. Due to the CM offset to the blade pitch axis and the twist angle, centripetal forces cause a negative deflection towards leading edge, while aerodynamic forces from the wind push the curve to negative deflections, leading to asymmetric oscillations with smaller deflection towards trailing edge and larger deflection towards

leading edge. CFD predicts an average -0.345 m for IP deflections, while NREL FAST and GH Bladed show an average value of -0.318 m and -0.304 m, respectively. All three methods also show similar deflection amplitudes.

4.3.4 Effect of Wind Shear

Realistic wind profiles account for the atmospheric boundary layer shear and turbulence. In this thesis, wind shear is modeled with the log-law wind profile as inlet boundary condition, $u(z) = u(z_{ref}) \ln(z/z_0)/\ln(z_{ref}/z_0)$, where z_{ref} is the hub height and z_0 is the surface roughness. The surface roughness is taken as the value for a smooth sea condition, $z_0 = 10^{-4}\, m$. A rougher surface will result in larger z_0 and the larger wind shear. With the non-dimensional axial wind speed at hub height as 1, the wind speed experienced by a blade of 63 m long at the tip is 0.912 at lowest position and 1.039 at the top (ignoring tilt), a 14% difference. Since forces scale with velocity squared, the forces will increase from bottom to top by approximately 30% at the blade tip section.

Figure 4.9 compares the time history of turbine thrust and torque for uniform and log-law wind and Table 4.5 shows quantitative values. The general trends are similar to those with uniform wind, but the mean thrust is about 1 % lower and the torque about 2% lower for both rigid and flexible turbines. The individual blade behavior, shown in Fig. 4.10, exhibits a significant increase in thrust and torque when the blade is at the top and a decrease when the blade is at the bottom, as expected. A logarithmic wind velocity distribution immediately results in higher AOAs when the blade is at the top and the incoming wind speed is higher, with a dramatic decrease when the blade is at the bottom adding the effect of lower wind speed with the tower shadow effect, see Fig. 4.12. Conversely, the axial induction factor tends to be flatter than for uniform winds.

Due to the blade loads affected by wind shear, blade OoP deflections under log-law wind follow closely the individual blade loads shown in Fig. 4.10, see Fig. 4.17 for time history of deflections and Table 4.6 for mean and standard deviation values. IP

deflections are less affected by the vertical wind distribution due to the large edge-wise stiffness of the blade, but the deflection from trailing edge to leading edge (negative IP) decreases by a small amount.

4.3.5 Effect of Wind Turbulence

Wind turbulence is a harsh challenge for both wind turbine operation and simulation due to its stochastic nature. The Mann wind turbulence model described in §2.4 was applied to both rigid and flexible turbines at the rated condition of 11.4 m/s with uniform wind to investigate effect of wind turbulence. Note that no time history results were reported by OC3 participants for the wind turbulence cases, but statistics and results in frequency domain were reported, allowing for some comparison. Also note that the OC3 cases have a pitch controller which significantly changes the behavior of the turbine, making comparisons with fixed pitch CFD only qualitative.

Figure 4.18 shows time histories of thrust and torque with wind turbulence, including a case for rigid turbine without wind turbulence for reference. As shown in Table 4.7, rigid turbine with wind turbulence shows small increases of 0.2% in mean thrust and 1.4% in mean torque respect to the case without turbulence, while the elastic turbine sees an increase of 4.7% for thrust and decrease of 4.9% for torque under wind turbulence, consistent with the trends seen in OC3 results. Large fluctuations exist due to the wind turbulence, with approximately 7 times larger standard deviation for both thrust and torque compared to the no wind turbulence case.

Figure 4.19 compares blade tip deflections for 11.4 m/s with and without wind turbulence. The OoP deflection increased considerably respect to the 8 m/s case shown in Fig. 4.17, where the average OoP deflection was approximately 3.6 m, increasing now to 6.3 m as shown in Table 4.8. The turbulence-induced fluctuations are considerable, reaching a maximum of almost 8 m, still far from the blade-tower design clearance of 13.2 m. Turbulence effects on IP deflection are much smaller, but still clearly noticeable.

The power spectrum densities of thrust, torque, and blade tip OoP and IP deflections are shown in Fig. 4.20. Peaks at low frequency compare well, but at higher frequencies CFD losses energy faster. Unfortunately a fair comparison is not possible since the use of a controller by OC3 introduces frequencies not present in CFD.

C_n and C_t represented by the averaged value over rotations for wind speed of 11.4 m/s show similar pattern with those at lower speed of 8 m/s, shown in Fig. 4.14, except that cases under wind turbulence consistently show significant large standard deviations than no-turbulence case. Figure 4.22 shows the time history of AOA, axial and tangential induction factor for wind turbulence effect. Comparing with the no-turbulence case, the flow parameters at $r/R = 16\%$ that close to root in general follow those of no-turbulence case, however, wind turbulence begins to dominate the local flow and airfoil behaviors, even for the tangential induction factor that only slightly affected by wind shear and turbine elasticity.

4.3.6 Flow Analysis

Vortical structures for the cases with and without turbulence are shown in Fig. 4.23 for a wind speed of 11.4 m/s. The vortical structures rendered as iso-surfaces of $Q = 1$, colored with axial velocity. The case without wind turbulence has strong tip and hub vortices, as well as vortex detachment from the tower. Notice that the tip vortices cannot be resolved beyond $x/R = 1$, the region covered by the finer refinement grid. In the case with turbulence vortical structures are present in the system as part of external atmospheric turbulence. These turbulent structures interact with the turbine, in particular with the tip vortices which become unstable and breakdown closer to the rotor. External wind turbulence also diffuses the wake faster, as can be seen comparing the cross sections at $y = -0.8$ for the cases with and without wind turbulence.

Cross sections of the wake are shown in Fig. 4.24. Axial velocity on lateral traverses at hub and top tip height for $x/R = -1, 1, 2, 3, 4$ are plotted in Fig. 4.25. The

CFD results show that the flexibility of the turbine has little effect on the wake, an important point since it suggests that wake studies can be performed with reasonable approximation using rigid turbines. The wind turbulence, on the other hand, has a considerable effect in the wake by adding, as expected, an effective eddy viscosity that diffuses the wake faster. This effect highlights the importance of proper estimation of the atmospheric and local turbulence to properly predict the wakes in a wind farm.

4.4 Summary

In this chapter, a high fidelity approach for wind turbine aero-elastic simulations including explicit representation of the atmospheric wind turbulence has been presented. The approach uses a dynamic overset CFD code to compute the aerodynamics coupled with a MBD code to predict the motion responses to the aerodynamic loads. This approach allows for accurate simulations of wind turbine under complex operational environment with the consideration of realistic wind turbulence and wind shear, and the blade elasticity.

The IEC 61400-1 ed. 3 recommended Mann wind turbulence model was implemented into the CFD code as boundary and initial conditions. The wind turbulence model was validated by comparing the generated stationary wind turbulence field with the theoretical one-point spectrum for the three components of the velocity fluctuations, and by comparing the expected statistics from the CFD simulated wind turbulent field with the explicit wind turbulence inlet boundary from Mann model. Extensive simulations based on the proposed coupled approach were conducted with the conceptual NREL 5MW offshore wind turbine in an increasing level of complexity, so as to validate and analyze the aerodynamic predictions, elasticity, wind shear and atmospheric wind turbulence. Results were compared with the publicly available simulations results from OC3 participants, showing good agreement for the aerodynamic loads and blade tip deflections in time and frequency domains. Wind turbulence/turbine interaction was

examined for the wake flow to analyze the influence of wind turbulence on wake diffusion, finding that explicit turbulence addition results in considerably increased wake diffusion.

Table 4.1 Basic properties of NREL 5MW offshore wind turbine

Baseline turbine properties	
Rating	5 MW
Rotor orientation, configuration	Upwind, 3 blades
Rotor diameter, hub diameter	126 m, 3 m
Hub height	90 m
Cut-in, rated, cut-out wind speed	3 m/s, 11.4 m/s, 25 m/s
Cut-in, rated rotor speed	6.9 RPM, 12.1 RPM
Rated tip speed	80 m/s
Control	Variable speed, collective pitch
Drivetrain	High speed, multiple-stage gearbox
Overhang, shaft tilt, precone	5 m, 5^o, 2.5^o
Tower properties	
Elevation to tower base above SWL	10 m
Elevation to tower top	87.6 m
Floating platform properties	
Depth to platform base below SWL	120 m
Elevation to platform top above SWL	10 m
Depth to top of taper below SWL	4 m
Depth to bottom of taper below SWL	12 m
Platform diameter above taper	6.5 m
Platform diameter below taper	9.4 m

Table 4.2 Grid system information

Name	i max	j max	k max	Total points	Hierarchy
Nacelle	51	48	61	149 K	Rotor-Nacelle
Tower	201	48	61	588 K	Rotor-Nacelle
RefAir	48	51	61	149 K	Rotor-Nacelle
Hub	51	48	61	149 K	Rotor
Blade1	151	48	61	442 K	Rotor
Tip 1	51	48	61	149 K	Rotor
Blade2	151	48	61	442 K	Rotor
Tip 2	51	48	61	149 K	Rotor
Blade 3	151	48	61	442 K	Rotor
Tip 3	51	48	61	149 K	Rotor
Blade Ref	67	48	92	295 K	Rotor
Blade Ref	67	48	92	295 K	Rotor
Blade Ref	67	48	92	295 K	Rotor
Background	244	101	123	3.03 M	Earth
Total				6.7 M	

Table 4.3 Simulation conditions for the selected cases from OC3 Phase I

Case	Controller	Wind Condition	Turbine Flexibility
2.1a	Constant rotor speed and fixed blade pitch	Steady, uniform, no shear: V_{hub} = 8 m/s	Rigid
2.1b	Controlled rotor speed		
2.2	Controlled blade pitch	V_{hub} = 11.4 m/s, I_{ref} = 0.14 (B), turbulence model = Mann	
3.1	Controlled rotor speed	Steady, uniform, no shear: V_{hub} = 8 m/s	Flexible
3.2	Controlled blade pitch	V_{hub} = 11.4 m/s, I_{ref} = 0.14 (B), turbulence model = Mann	

Table 4.4 Summary of OC3 results for wind speed 8 m/s

Participant		NREL FAST			GH Bladed		
Case		2.1 a	2.1 b	3.1	2.1 a	2.1 b	3.1
Rotor speed [RPM]	Mean	9.000	9.334	9.329	9.000	9.136	9.128
	Min	9.000	9.332	9.324	9.000	9.133	9.125
	Max	9.000	9.337	9.335	9.000	9.139	9.132
	σ	0.000	0.002	0.003	0.000	0.002	0.002
Thrust [KN]	Mean	384.97	394.74	409.63	372.32	375.62	378.61
	Min	377.70	387.30	406.30	361.06	364.19	376.07
	Max	387.00	396.90	412.70	374.49	377.90	381.26
	σ	2.60	2.66	1.46	3.77	3.82	1.36
Shaft torque [KN m]	Mean	2096.40	2033.76	2031.62	1975.54	1948.36	1945.01
	Min	2019.00	2025.00	2019.00	1863.94	1931.70	1933.54
	Max	2115.00	2036.00	2043.00	1998.38	1958.56	1954.30
	σ	27.37	2.88	5.87	37.40	5.87	5.31
power [KW]	Mean	1975.81	1987.95	1984.80	1861.90	1864.04	1859.23
	Min	1902.86	1979.34	1971.58	1756.72	1847.71	1847.86
	Max	1993.34	1990.74	1996.72	1883.43	1873.13	1867.93
	σ	25.79	2.86	5.81	35.25	5.66	5.12

Table 4.5 Thrust and torque for wind speed 8 m/s

Participant		CFD		NREL FAST	GH Bladed
Case		Uniform, rigid	Log-law, rigid	2.1a	2.1a
Thrust [KN]	Mean/ Difference	388.9 (4.46%)	385.0 (3.41%)	385.0 (3.41%)	372.3 (0.00%)
	Min/ Difference	382.0 (5.79%)	378.2 (4.74%)	377.7 (4.60%)	361.1 (0.00%)
	Max/ Difference	392.5 (4.81%)	388.2 (3.66%)	387.0 (3.34%)	374.5 (0.00%)
	σ	2.71	2.75	2.60	3.77
Shaft torque [KN m]	Mean/ Difference	1945.7 (-1.51%)	1899.6 (-3.84%)	2096.4 (6.12%)	1975.5 (0.00%)
	Min/ Difference	1869.8 (0.32%)	1830.5 (-1.79%)	2019.0 (8.32%)	1863.9 (0.00%)
	Max/ Difference	1980.1 (-0.92%)	1929.0 (-3.47%)	2115.0 (5.83%)	1998.4 (0.00%)
	σ	27.53	26.53	27.37	37.40
Case		Uniform, flex	Log-law, flex	3.1	3.1
Thrust [KN]	Mean/ Difference	402.6 (6.34%)	398.2 (5.18%)	409.6 (8.19%)	378.6 (0.00%)
	Min/ Difference	396.0 (5.29%)	391.4 (4.07%)	406.3 (8.03%)	376.1 (0.00%)
	Max/ Difference	406.7 (6.66%)	401.7 (5.35%)	412.7 (8.23%)	381.3 (0.00%)
	σ	2.30	2.40	1.46	1.36
Shaft torque [KN m]	Mean/ Difference	1934.6 (-0.53%)	1886.1 (-3.03%)	2031.6 (4.45%)	1945.0 (0.00%)
	Min/ Difference	1853.3 (-4.15%)	1811.2 (-6.33%)	2019.0 (4.42%)	1933.5 (0.00%)
	Max/ Difference	1974.5 (1.03%)	1918.4 (-1.84%)	2043.0 (4.54%)	1954.3 (0.00%)
	σ	25.73	23.71	5.87	5.31

Table 4.6 Blade 1 tip deflections for wind speed 8 m/s

Participant		CFD		NREL FAST	GH Bladed
Case		Uniform wind	Log-law wind	3.1	3.1
Out-of-Plane deflection [m]	Mean	3.592	3.559	3.244	3.011
	Min	3.510	3.309	3.109	2.857
	Max	3.692	3.709	3.370	3.149
	σ	0.059	0.107	0.090	0.098
In-Plane deflection [m]	Mean	-0.345	-0.340	-0.318	-0.304
	Min	-0.703	-0.702	-0.795	-0.749
	Max	-0.001	0.007	0.164	0.139
	σ	0.246	0.249	0.334	0.311

Table 4.7 Thrust and torque for wind speed 11.4 m/s

Participant		CFD		
Case		No turbulence, rigid	Wind Turbulence, rigid	Wind turbulence, flexible
Thrust [KN]	Mean	758.67	760.03	795.84
	Min	737.29	640.04	694.12
	Max	768.79	858.04	869.92
	σ	7.23	48.88	44.40
Torque [KN m]	Mean	4267.34	4327.05	4113.94
	Min	4003.72	2890.96	2983.40
	Max	4385.58	5706.80	5067.52
	σ	88.59	619.86	519.06

Table 4.8 Blade 1 tip deflections for wind speed 11.4 m/s

Participant		CFD	
Case		No turbulence	Wind turbulence
Out-of-Plane deflection [m]	Mean	6.383	6.387
	Min	6.264	5.248
	Max	6.540	7.913
	σ	0.059	0.463
In-Plane deflection [m]	Mean	-0.601	-0.606
	Min	-0.976	-1.184
	Max	-0.233	-0.087
	σ	0.259	0.281

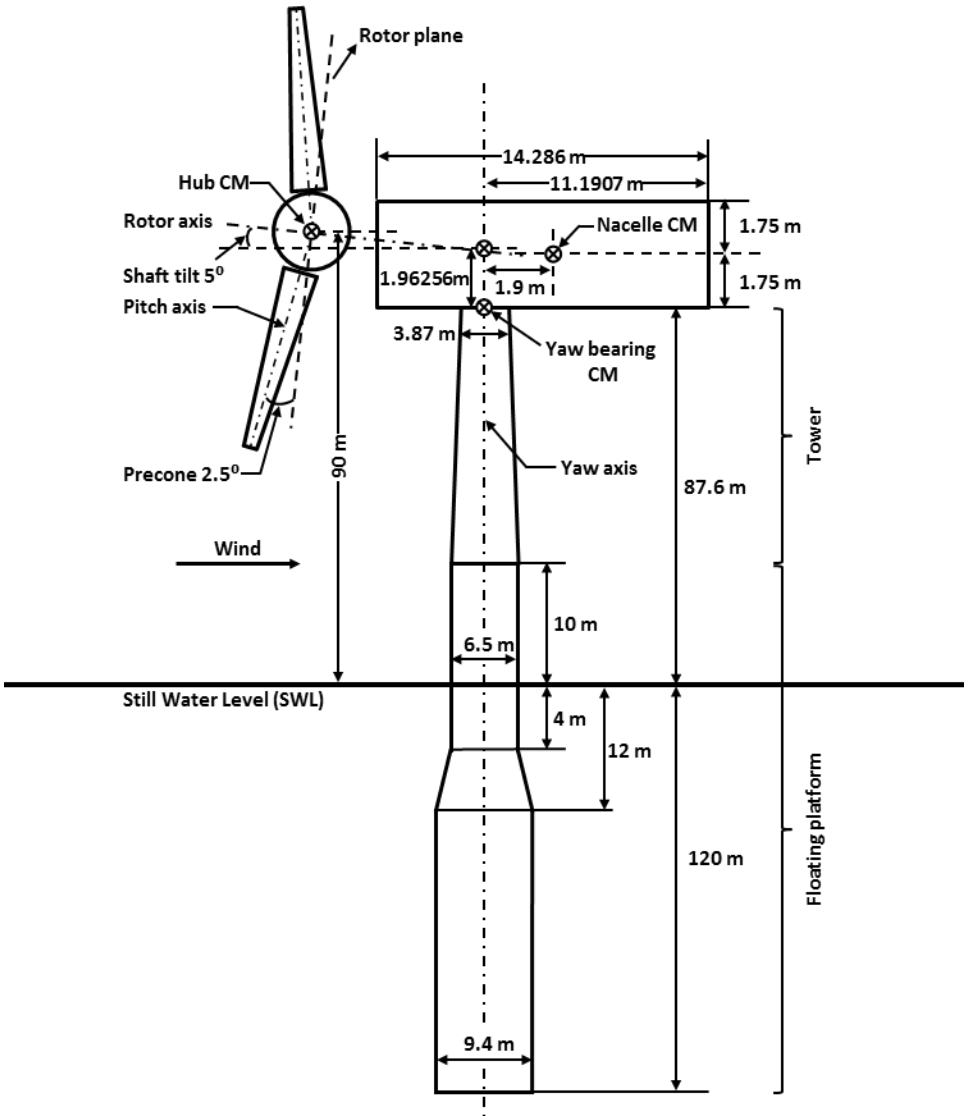

Figure 4.1 NREL 5MW offshore wind turbine configuration

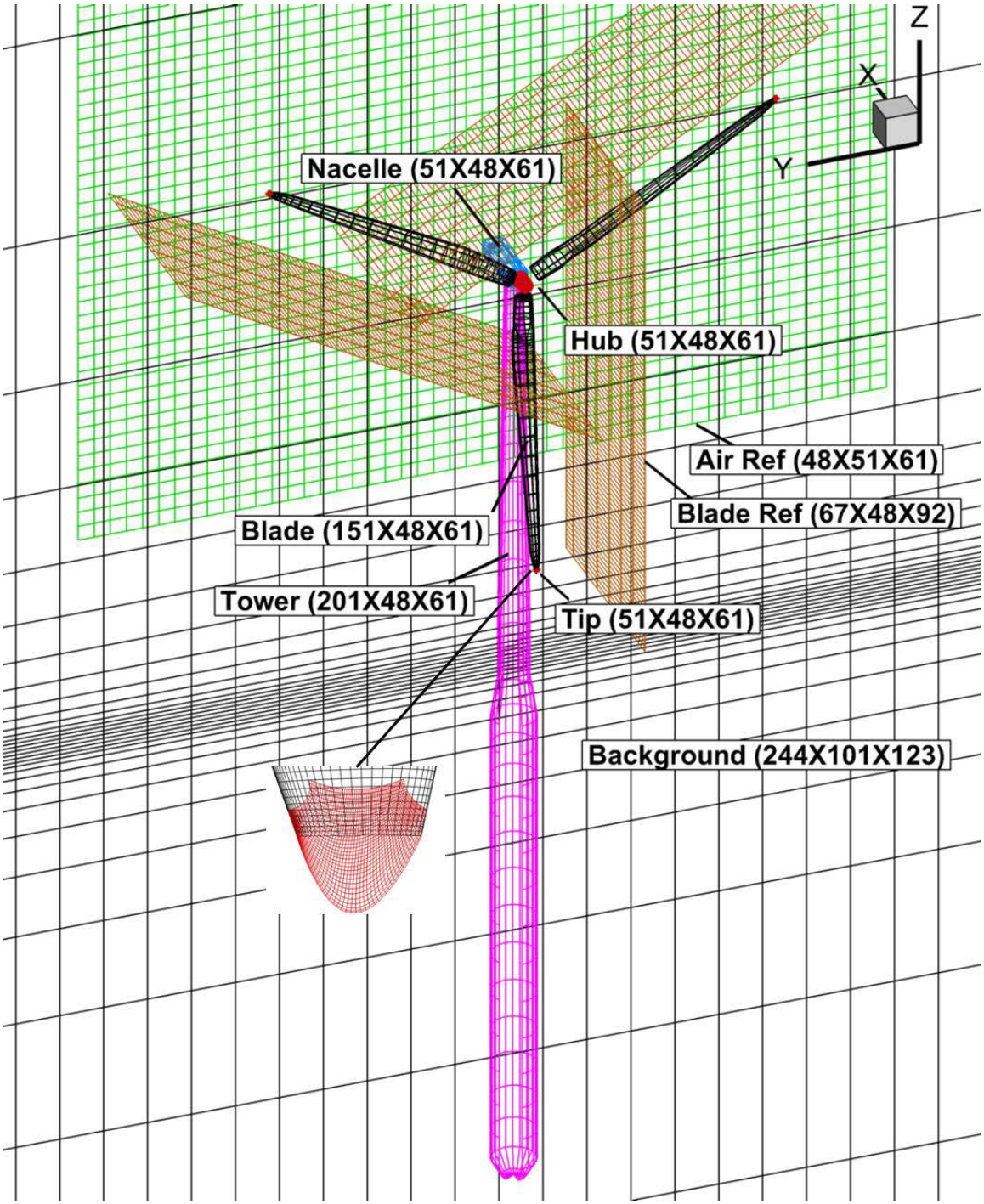

Figure 4.2 Grid system. Slice in x shows background (black) and wake refinement (green) grids. Axis-aligned slices on the blades show blade refinements (brown). (Grid points are skipped in all directions for clarity)

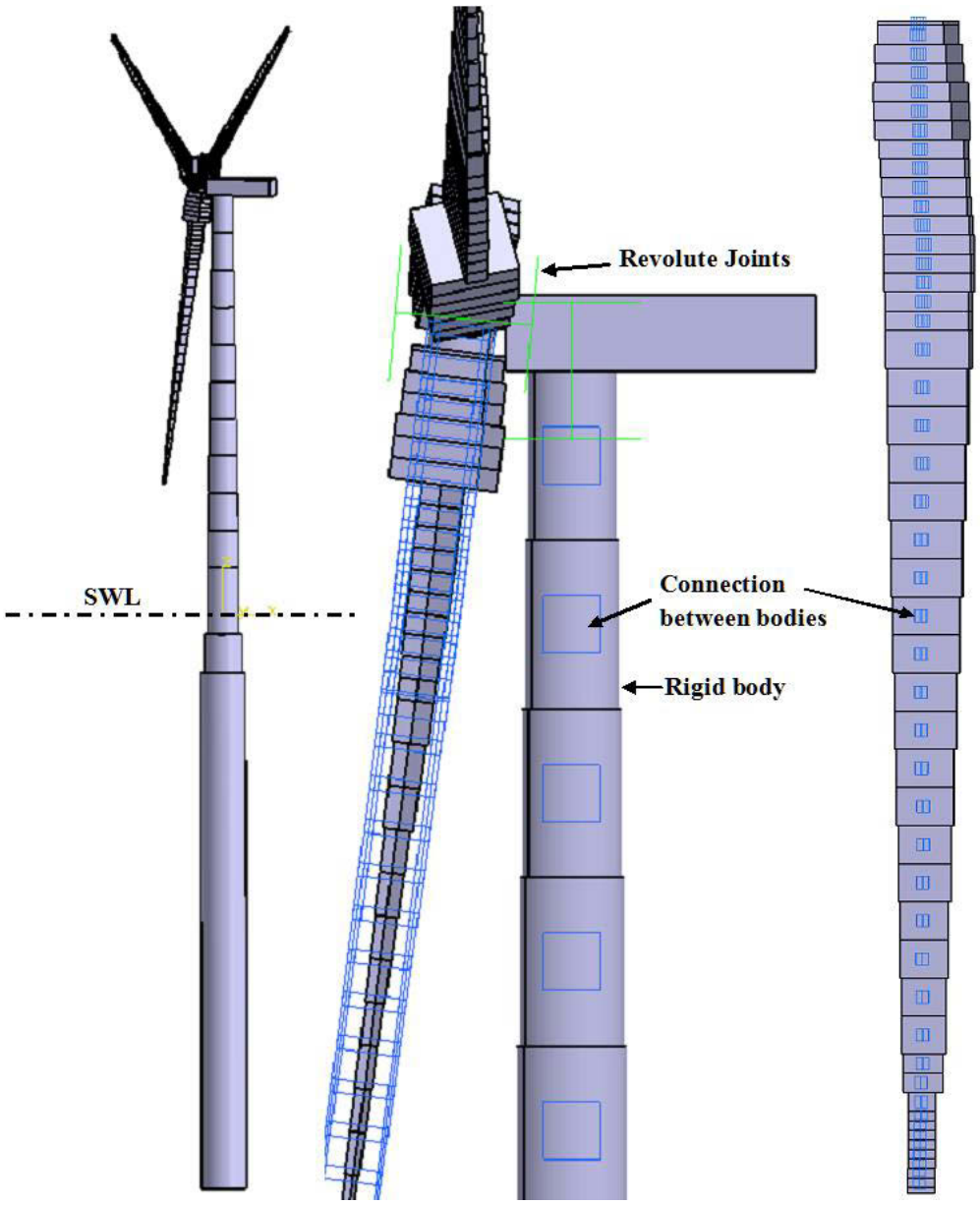

Figure 4.3 Multi-body system model

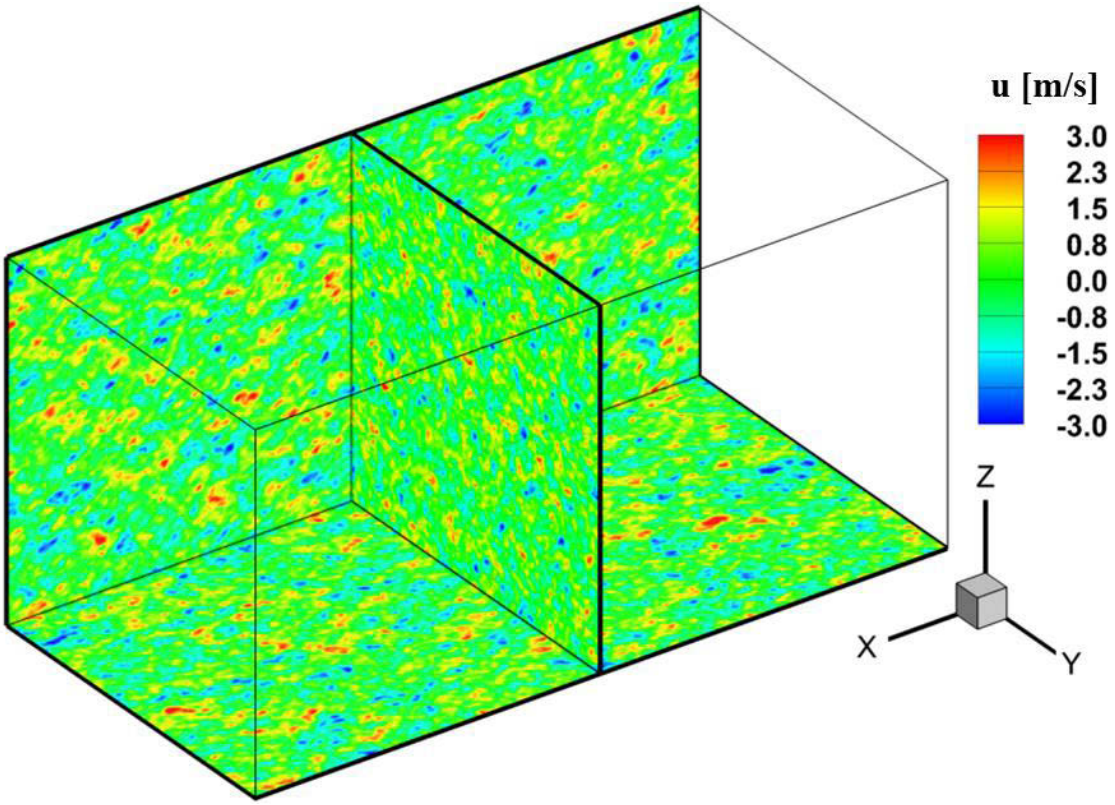

Figure 4.4 Demonstration of the Mann turbulence box with axial velocity fluctuations

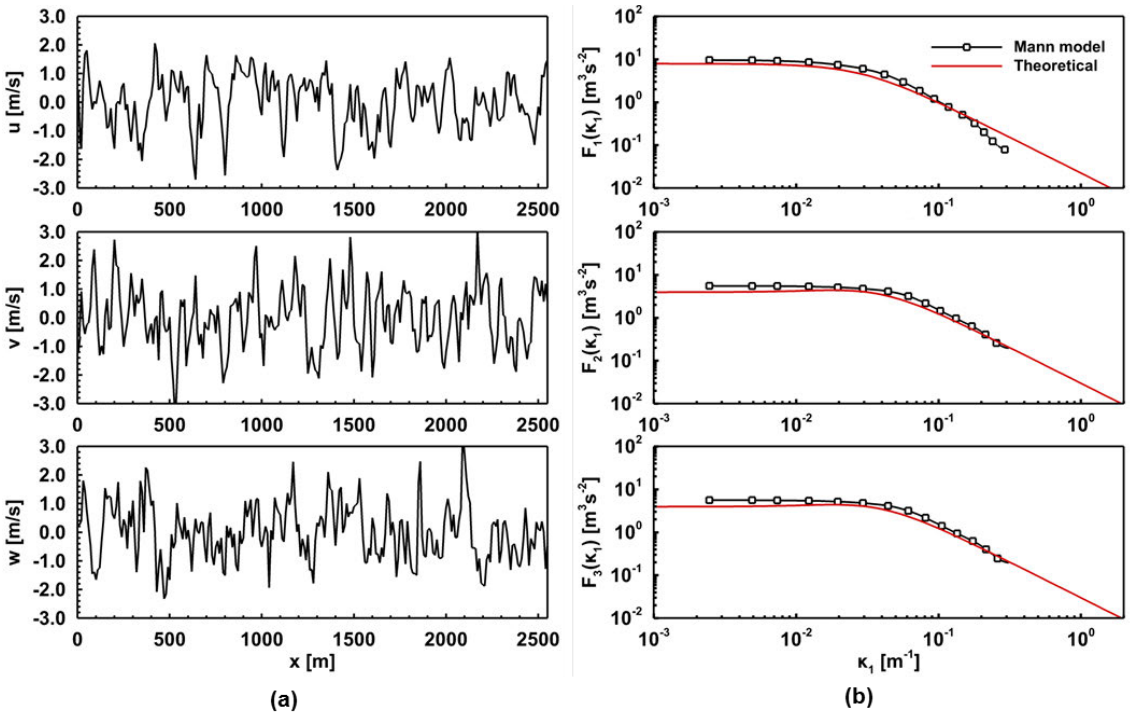

Figure 4.5 Mann wind turbulence box validation (a): pseudo time history of velocities fluctuations at a selected point; (b) comparison of one-point spectrum for all points in the Mann box and the theoretical spectrum

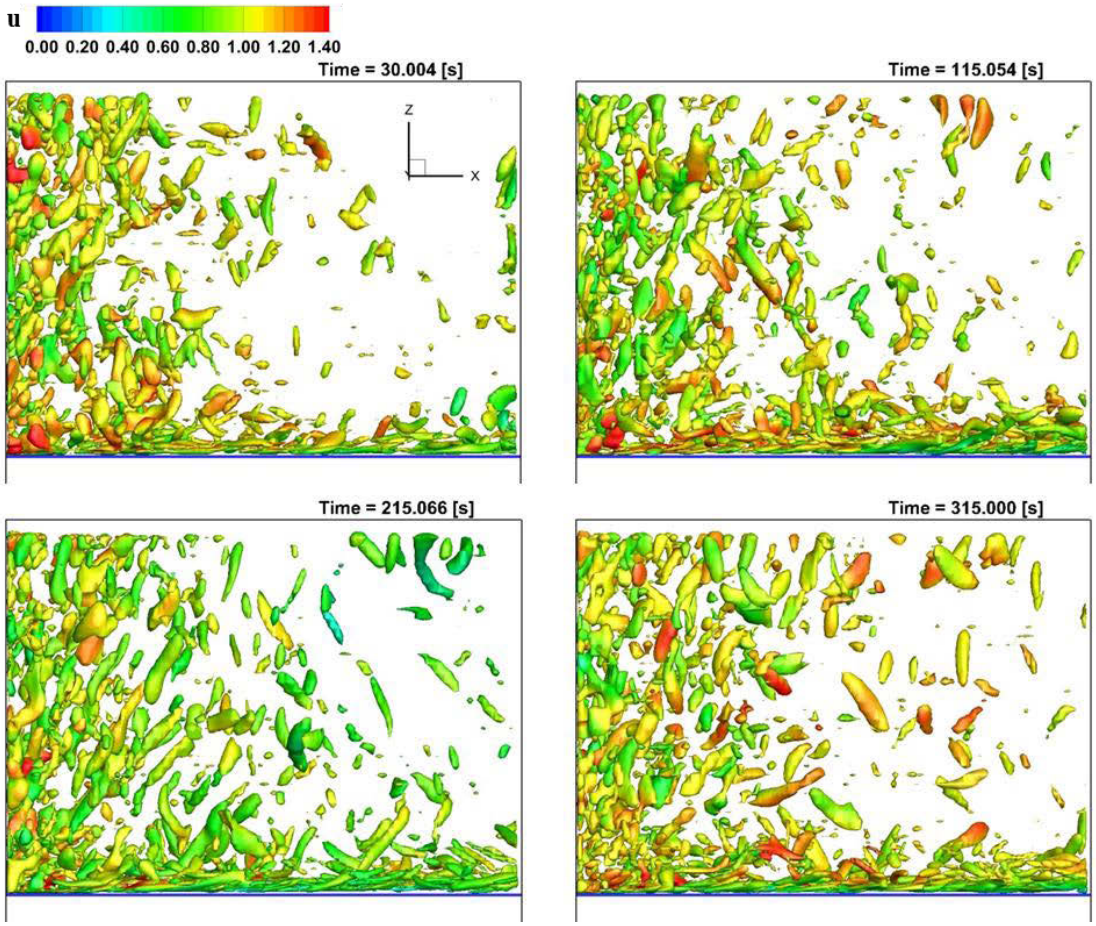

Figure 4.6 Evolution of the vortical structure represented by Q = 1 contoured with non-dimensional axial velocity u for turbulent filed simulation

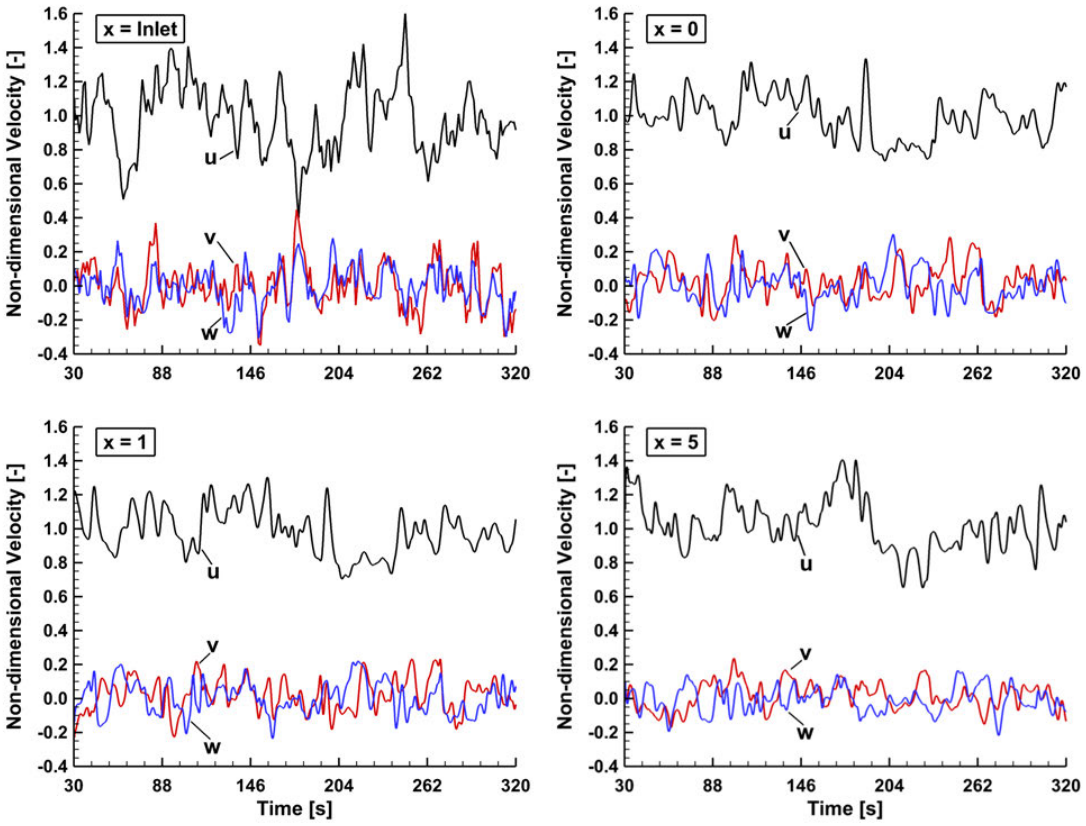

Figure 4.7 Time history of turbulent velocities at hub height (y=0 m; z = 90 m) and different non-dimensional axial positions

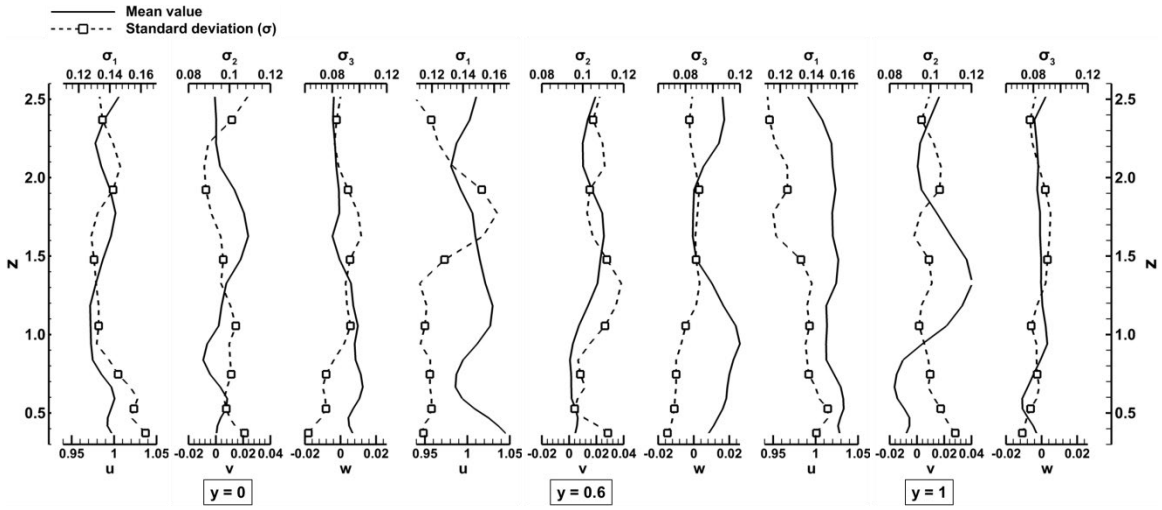

(a)

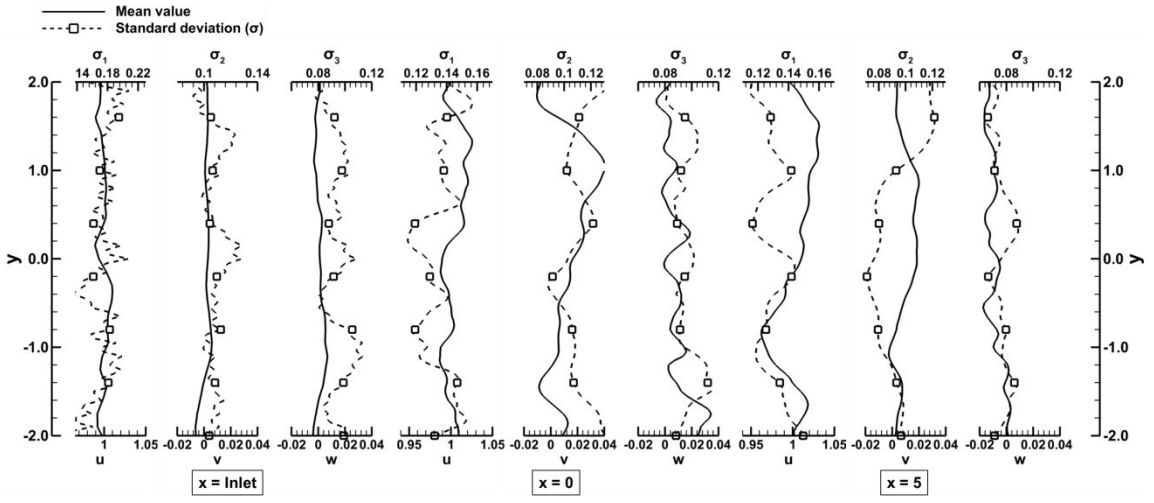

(b)

Figure 4.8 Flow field statistics for several vertical lines at $x = 0$ (a) and horizontal lines at $z = 93\ m$ (b)

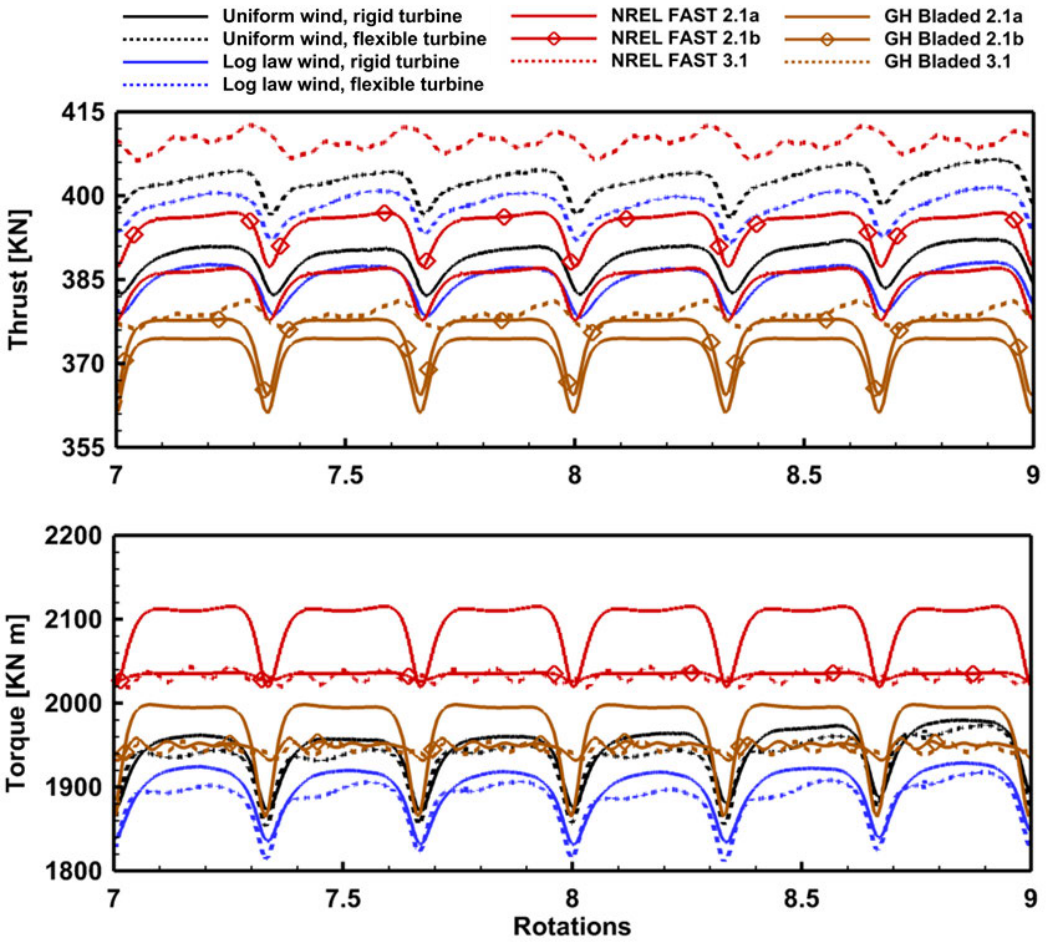

Figure 4.9 Thrust and torque for wind speed 8 m/s

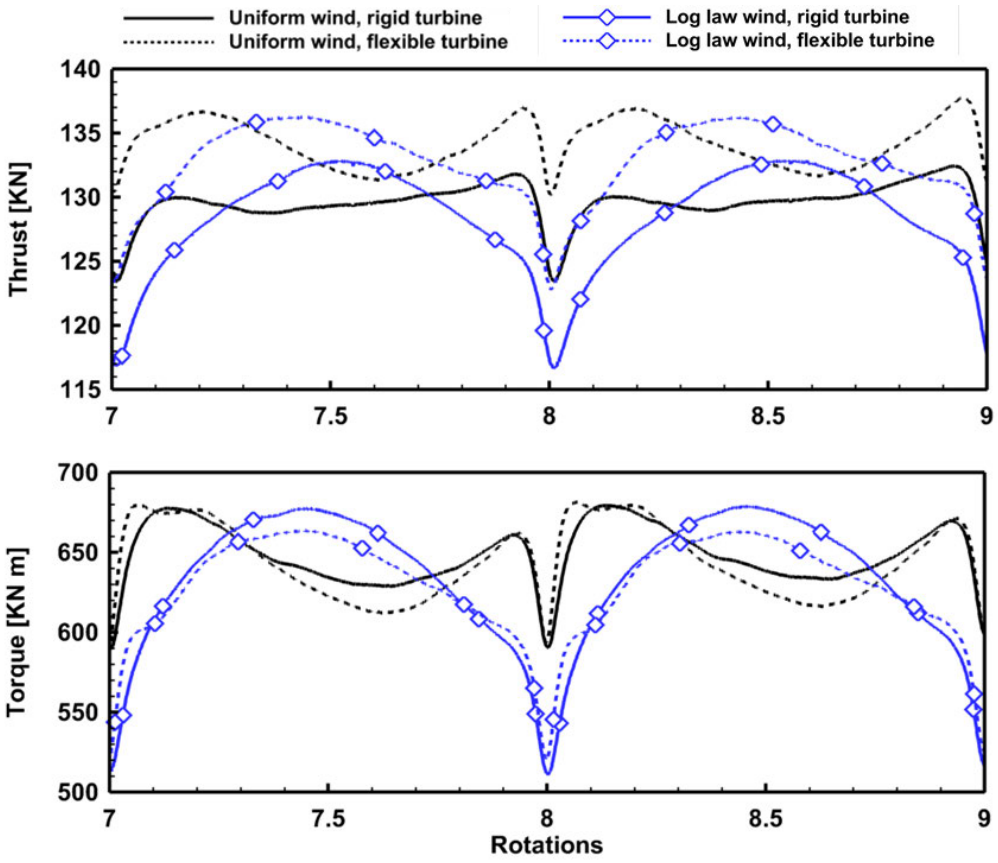

Figure 4.10 Thrust and torque for blade 1

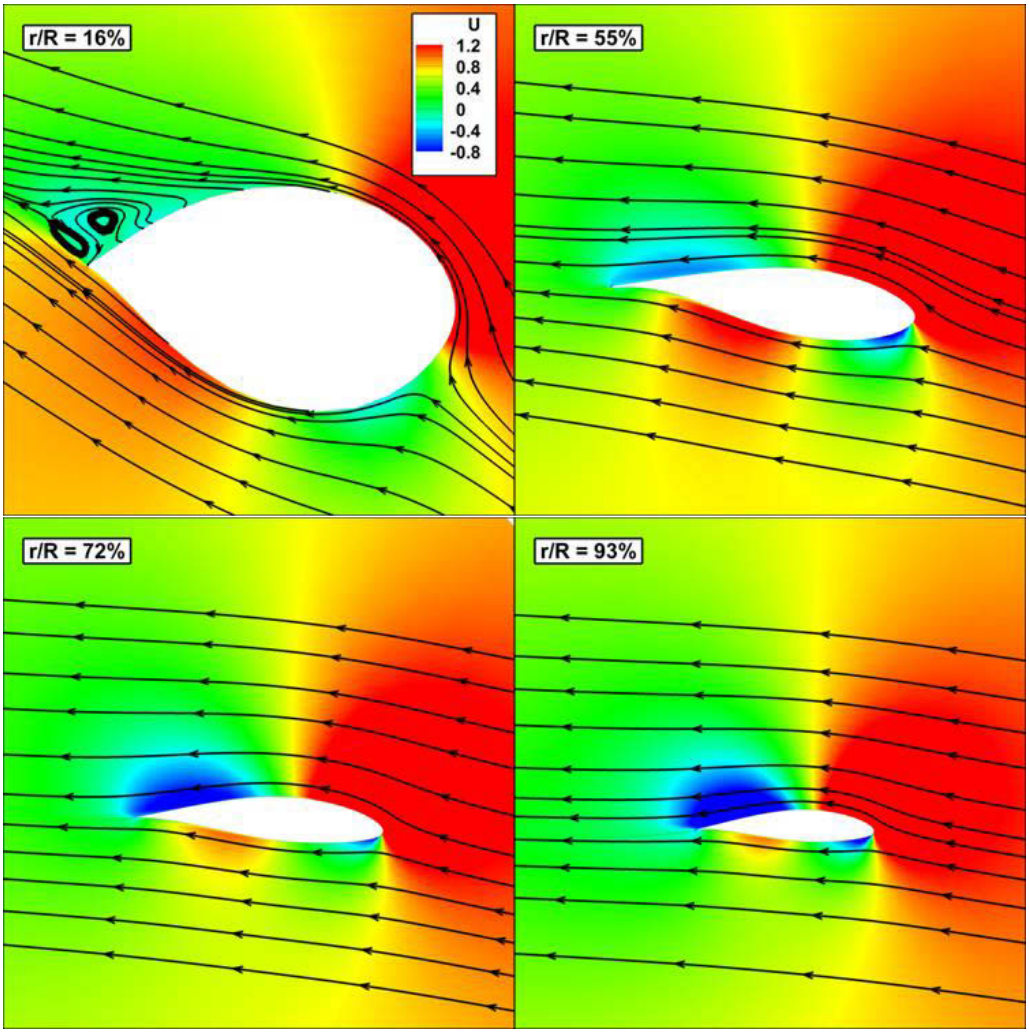

Figure 4.11 Instantaneous flow field contoured by non-dimensional axial velocity in blade system at wind speed 8 m/s

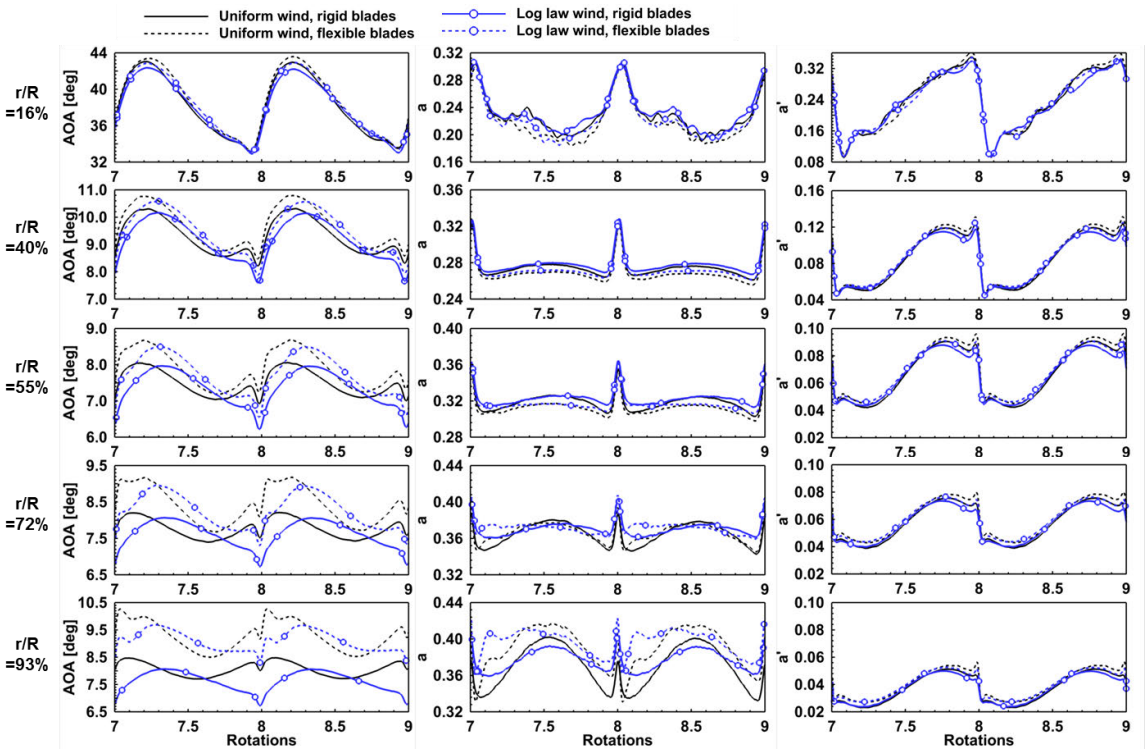

Figure 4.12 Time history of angle of attack (left), axial induction factor *a* (center) and tangential induction factor *a'* (right) at selected radial positions for blade 1 with wind speed 8 m/s

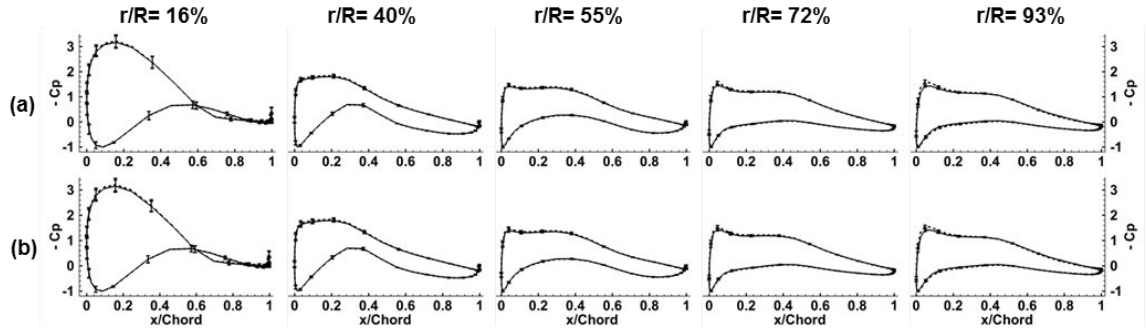

Figure 4.13 Average pressure coefficient and standard deviation at selected radial positions for uniform wind (a) and log-law wind at wind speed 8 m/s (solid: rigid turbine; dashed: flexible turbine)

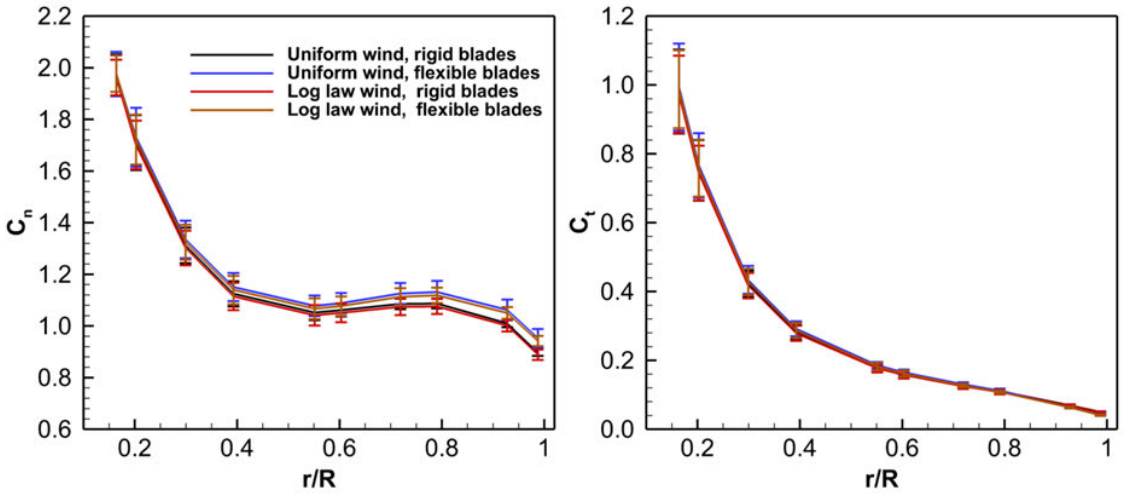

Figure 4.14 Radial distribution of Cn and Ct for wind speed 8 m/s

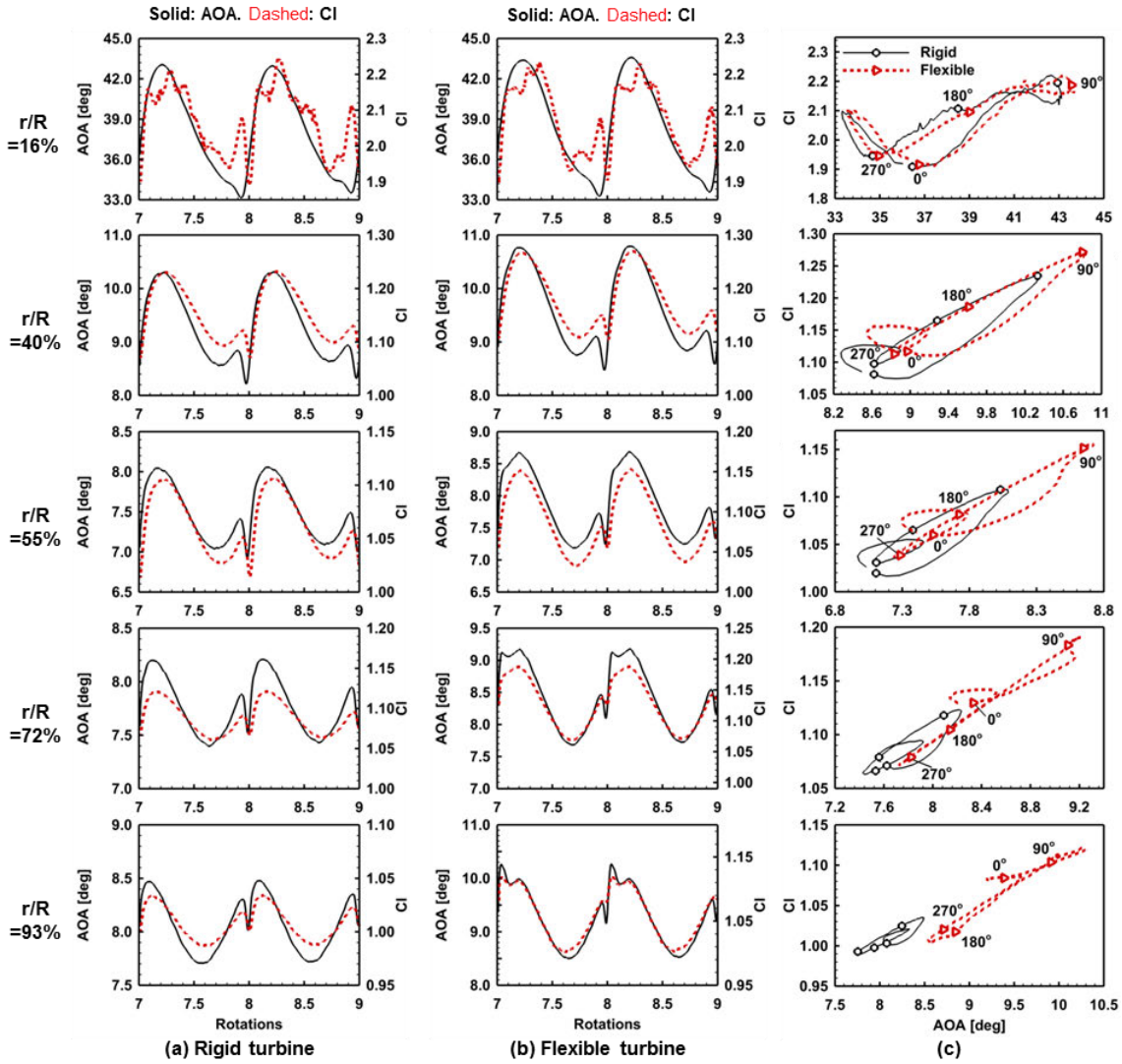

Figure 4.15 AOA and C_l for wind speed 8 m/s

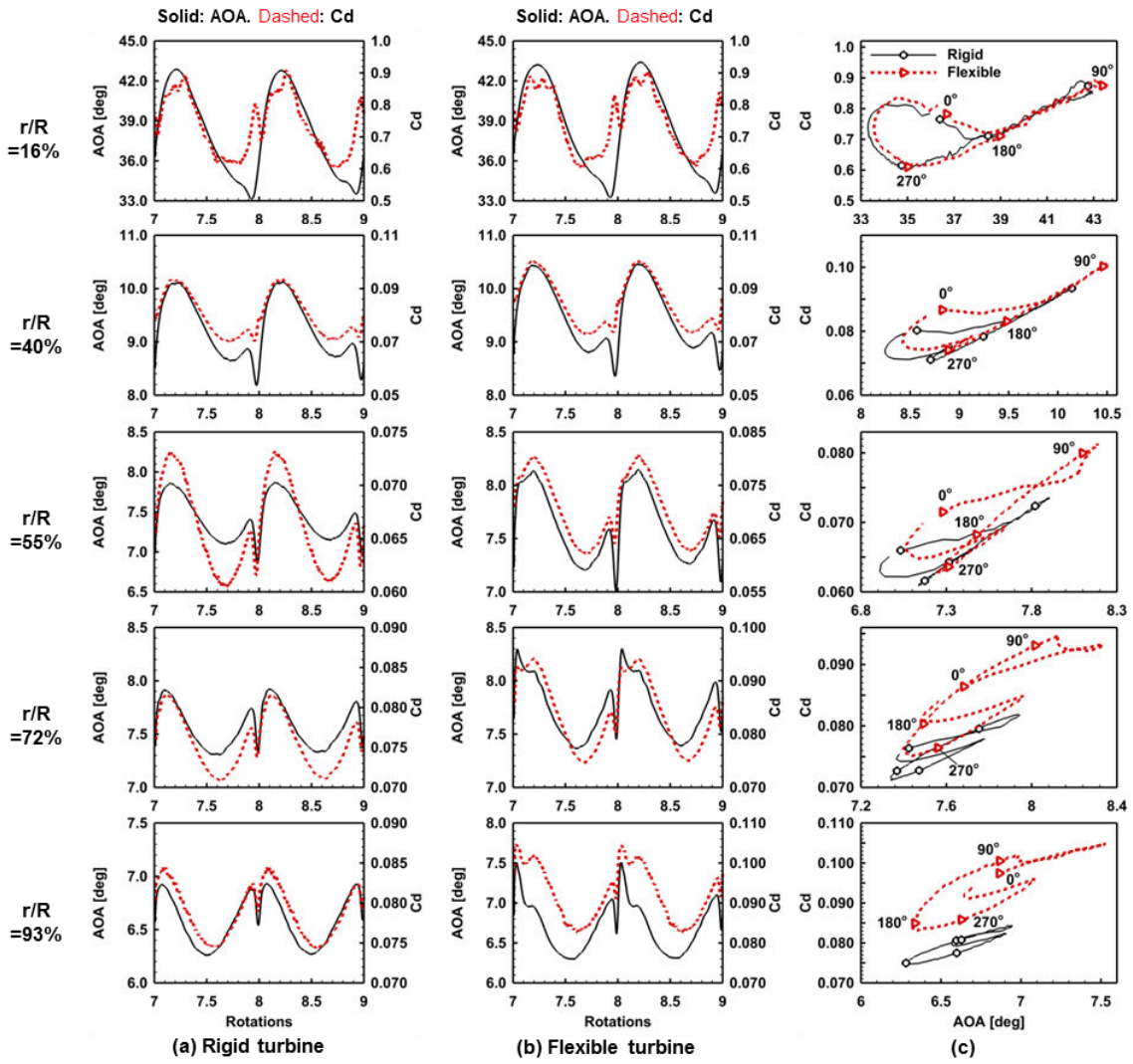

Figure 4.16 AOA and C_d for wind speed 8 m/s

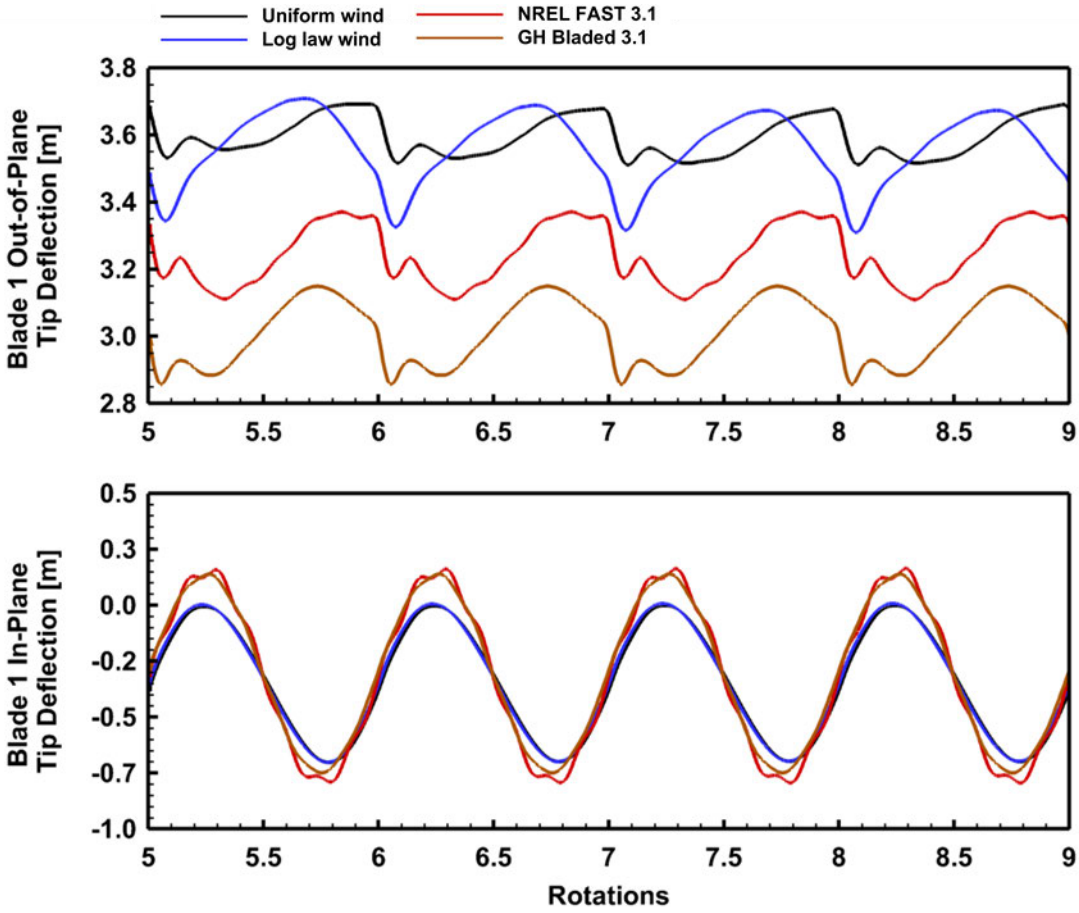

Figure 4.17 Deflections for blade 1 tip for wind speed 8 m/s

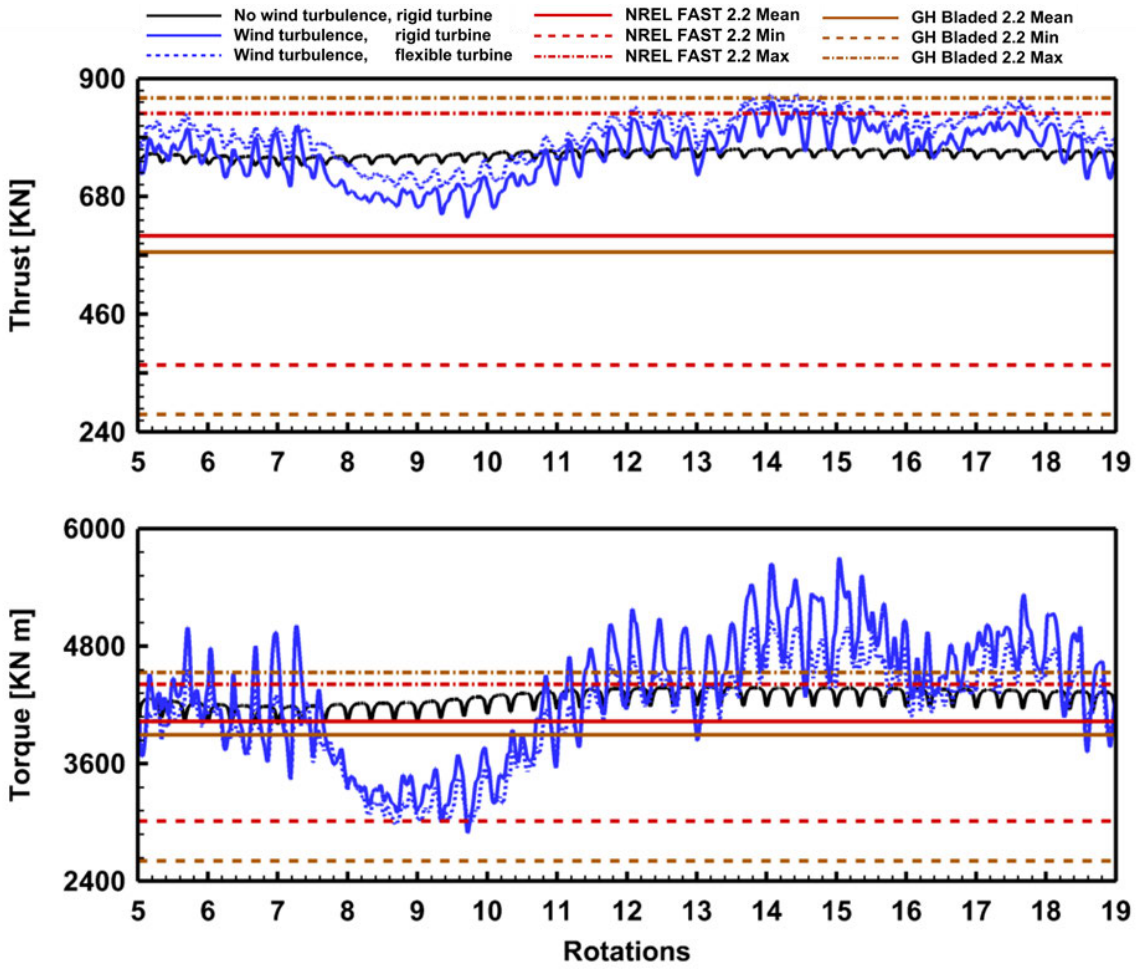

Figure 4.18 Thrust and torque for wind speed 11.4 m/s

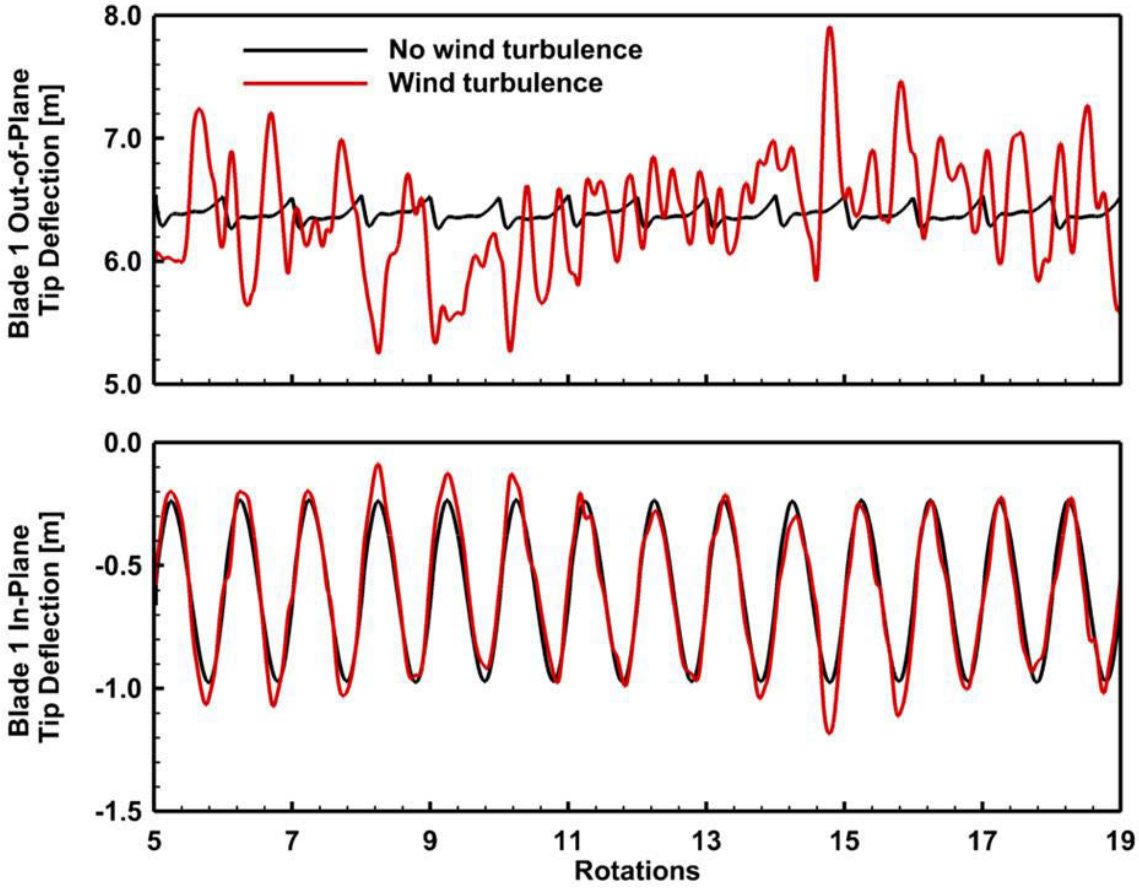

Figure 4.19 Blade tip deflections for wind speed 11.4 m/s

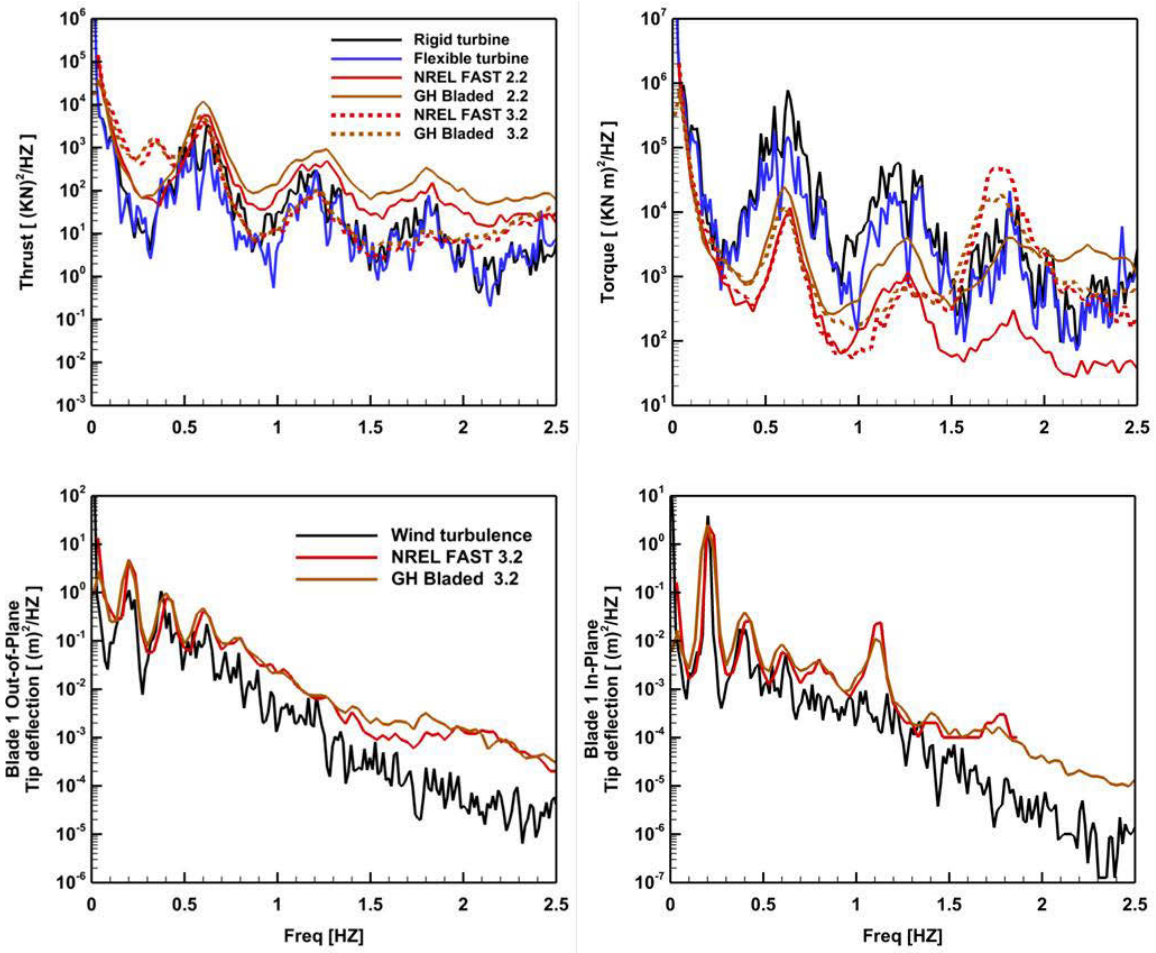

Figure 4.20 Power spectrum density of thrust, torque and blade tip deflections for wind speed 11.4 m/s

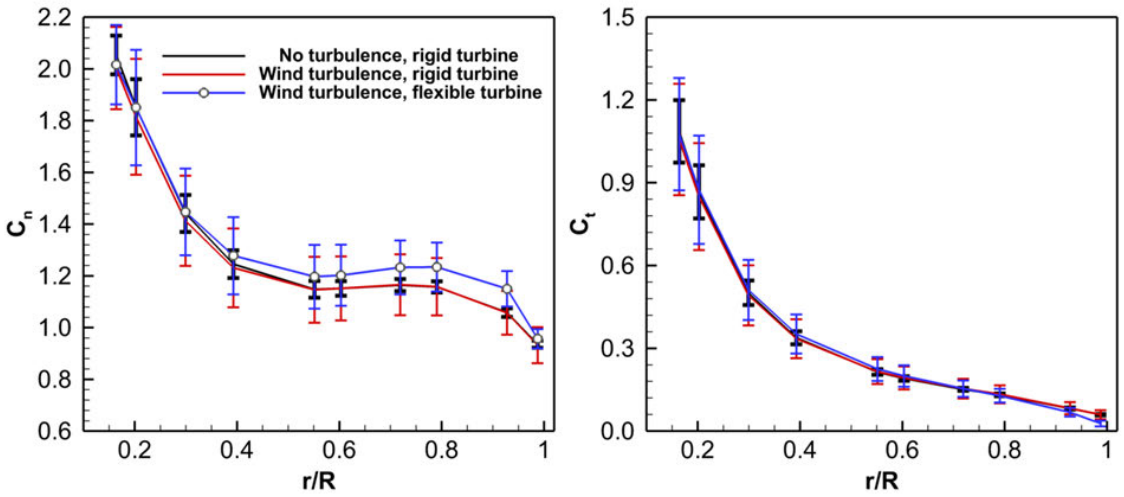

Figure 4.21 Radial distribution of Cn and Ct for wind speed 11.4 m/s

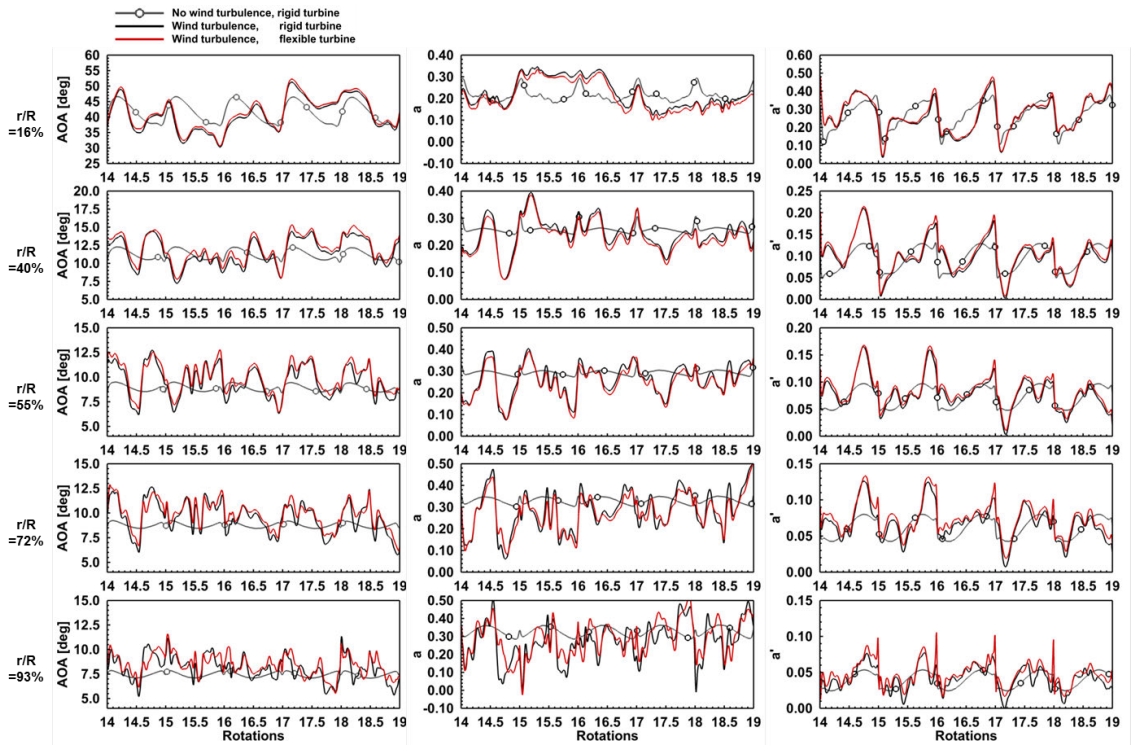

Figure 4.22 Time history of angle of attack (left), axial induction factor *a* (center) and tangential induction factor *a'* (right) at selected radial positions for blade 1 with wind speed 11.4 m/s

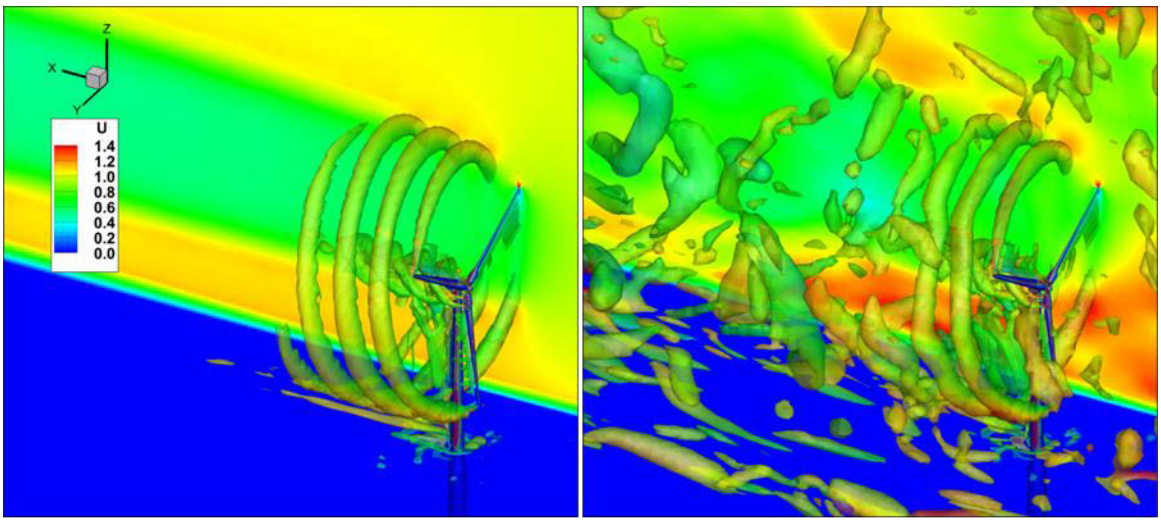

(a) No wind turbulence (b) wind turbulence

Figure 4.23 Vortical structures represented by Q=1 for cases with and without wind turbulence, for mean hub height wind speed 11.4 m/s

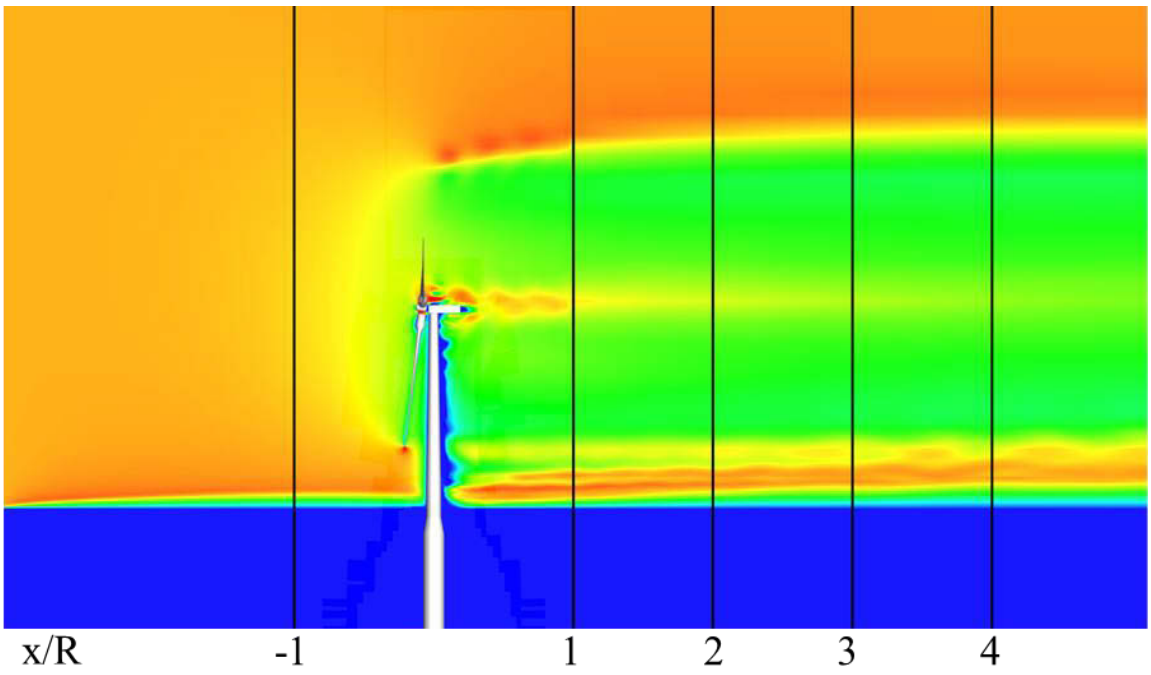

Figure 4.24 Locations of the cross sections contoured with axial velocity

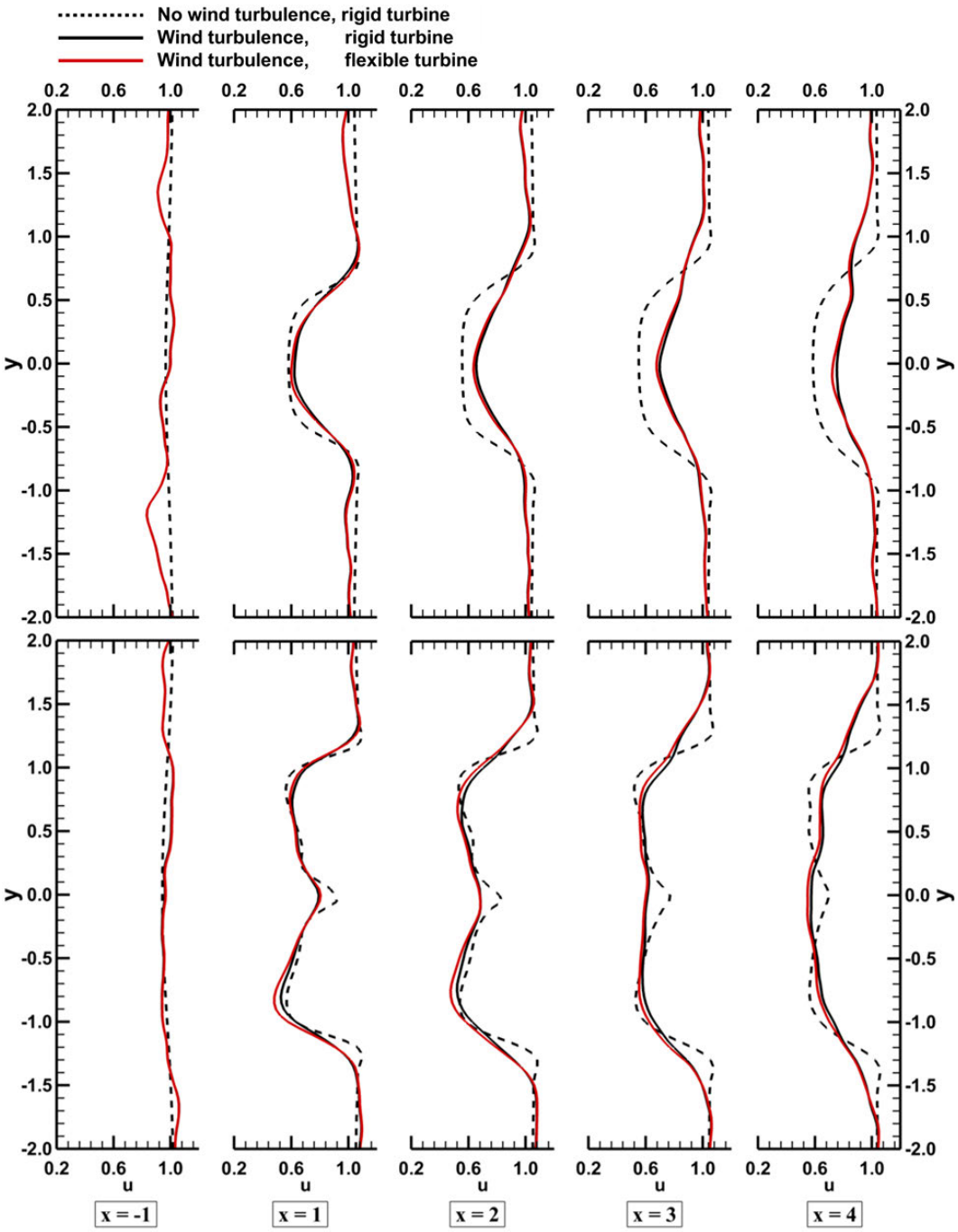

Figure 4.25 Axial velocities at different axial positions and at hub height ($z = 90\ m, z/R = 1.428$, bottom) and at top tip height ($z = 153\ m, z/R = 2.428$, top) for wind speed 11.4 m/s

CHAPTER 5

WIND TURBINE DYNAMIC MODELING WITH DRIVETRAIN

5.1 Overview

The drivetrain plays an important role in the wind turbine system, converting the mechanical power to electrical power, supporting the rotor inertial, gravitational and aerodynamic loads, and regulating the rotor transients. The resulting external low frequency and internal high frequency excitations that the drivetrain needs to withstand underscore the importance of investigating the drivetrain dynamics, including shaft-gearbox-generator interactions.

Two conventional and different approaches exist to study drivetrain dynamics. On one hand, efforts focus on detailed assessment of external operational conditions (aerodynamic loads and wind turbulence), and the drivetrain reduces to a simple representation with a few DOFs. On the other hand, detailed drivetrain models and prototypes are built to investigate dynamics of drivetrain components and gear-level loads, yet input from the rotor is usually simplified to steady torsional loads on the main shaft. A coupled approach with high-fidelity simulation of the wind loads while performing an advanced computation of the drivetrain has not yet been tried.

In this chapter, an attempt is made to improve drivetrain dynamics estimation. This is done by constructing the studied wind turbine with a drivetrain model using the coupled CFD/MBD approach. This approach enables investigation of interactions between aerodynamic loads and gearbox reaction including shaft-gearbox-generator dynamics, making it a unique tool that is capable of predicting gear-level loads resulting from realistic transient turbulent winds with flexible blades.

5.2 Simulation Design

5.2.1 Drivetrain Modeling

Figure 5.1 shows an overall configuration for the drivetrain modeling in this thesis. The model was built in an increasing level of complexity, from the simplest 2-DOFs rotor-generator torsional model to including a 3-stage gearbox with gear contact and bearing representation. Due to the limited details of the conceptual NREL 5MW offshore wind turbine drivetrain, and the unavailability of a utility-scale wind turbine drivetrain for numerical modeling, a representative 3-point suspension drivetrain configuration from the Gearbox Reliability Collaborative project (GRC) (Link et al. 2011) is adopted and tuned to match the 5MW turbine. The original GRC drivetrain has a 750 KW rating and an overall gear ratio of 1:81.491. The gearbox has one planetary stage and two parallel stages as intermediate stage and high speed stage. Three planetary gears are equally spaced around the sun gear, and supported by the planet carrier which distributes the torsional loads among the planets from the main shaft. The properties of the shafts and gearbox were then tuned to match the drivetrain properties of the OC3 turbine used in §4, as summarized in Table 5.1.

Three levels of drivetrain modeling complexity are considered, which could be adopted for different levels of simulation needs. Drivetrain components, e.g. shafts and gears, are each represented by a 6-DOFs rigid body, with appropriate kinematic constraints and dynamic force elements to describe their connections. The 2-DOFs rotor-generator torsional model is the simplest, constructing by revolute joints for shafts and kinematic constraints within gearbox for gear ratio in the multi-body model system. Bracket joints constraining relative motions were used between the connected shafts. Though simple, this model enables the implementation of the wind turbine control system discussed in detail in the following section, which requires interaction between rotor and generator. The next level of drivetrain model still focuses on the torsional DOFs, with a

3-stage gearbox model that includes gear contact force elements and is capable of estimating physical multi-tooth contact, changes in the direction of gear rotation, and gear-level loads. The most complicated model implemented in this thesis adds bearing representation with the radial bushing force element (see Fig. 5.1 for bearing locations) and enables all DOFs in the plane of rotation for shafts and gears. This allows for more realistic estimation of the drivetrain dynamics, including shaft misalignment due to wind gusts or wind turbulence, non-torque loadings due to asymmetric rotor loads, and bearing and gear-level loads.

5.2.2 Wind Turbine Control System

A conventional variable speed, variable blade pitch wind turbine control system based on the OC3 project (Jonkman et al. 2009) was implemented in the simulation tool, consisting of a generator torque controller and a full-span rotor-collective blade pitch controller operating independently at different wind turbine operational conditions.

Figure 5.2 shows a schematic of the control system. Depending on the generator speed, the wind turbine operation can be categorized in 5 different regions. The generator torque controller is used when the turbine is operated below the rated conditions (wind speed 11.4 m/s, generator speed 1173.7 RPM or rotor speed 12.1 RPM). As shown in Figs. 5.1 and 5.2(a), the controller applies torque as a function of the generator speed on the high speed shaft (HSS) of the model, which is rigidly connected to the generator, such that the rotor speed is regulated with the purpose of obtaining the best efficiency. In region 1 below cut-in wind speed, the wind power is used to accelerate the rotor for the turbine start-up, and therefore the generator torque is zero with no power extracted from the wind. Region 1½ is a linear transition between the start-up and region 2, as to place a lower limit of the generator speed to limit the wind turbine's operational speed range. Region 2 is designed for the turbine to best capture the wind power, and the generator torque is proportional to the square of the generator speed as to maintain a constant

optimal tip-speed ratio (Refer to the curve "Optimal torque" in Fig. 5.2(a)). The linear transition region 2½ is needed to limit tip speed at rated power. In region 3 beyond the rated condition, either constant power or constant torque could be applied depending on the control need, resulting in the relationship that the generator torque is inversely proportional to the generator speed or as the constant rated torque.

The blade pitch controller applies controlled torque on the revolute joints connected the individual blades to the hub when the turbine is operating beyond the rated conditions (region 3), shown in Figs. 5.1 and 5.2(b). The full-span rotor-collective blade pitch controller is constructed with a gain-scheduled proportional-integral (PI) controller on the speed error between the actual generator speed and the rated generator speed (1173.7 RPM). The change of the pitch angle is executed by applying the corresponding torque on the rotational spring-damper element of the blade revolute joint.

The relationship of the change of the pitch angle and the speed error can be written as (Jonkman et al. 2009)

$$\Delta\theta = K_P \Delta\Omega + \mathrm{K}_I \int_0^t \Delta\Omega \mathrm{dt} \tag{5.1}$$

where $\Delta\theta$ is a change of the blade pitch angle in radians, $\Delta\Omega = \Omega_{current} - \Omega_{rated}$ is the generator speed error, of which $\Omega_{rated} = 122.91\, rad/s$ is the design rated generator speed and $\Omega_{current}$ is the generator speed at current time step, K_P and K_I are the controller's proportional and integral gains, respectively.

$$K_P = K_{P,0} \times GK(\theta) \tag{5.2}$$

$$K_I = K_{I,0} \times GK(\theta) \tag{5.3}$$

$$GK(\theta) = (1 + \theta/\theta_K)^{-1} \tag{5.4}$$

where $K_{P,0} = 0.01882681\, s$, $K_{I,0} = 0.008068634$ and $\theta_K = 0.109988412\, rad$ are model constants. $GK(\theta)$ is the dimensionless gain-correction factor, and θ is the current blade pitch angle.

5.2.3 Simulation Cases

Simulation cases in this chapter were designed with an increasing level of complexity to demonstrate different aspects of the implemented wind turbine dynamic modeling with drivetrain, see Table 5.2 for a summary. Compared to the imposed condition in §4, these cases provide a more realistic scenario for prediction of turbine behavior.

Case set 1 was designed to investigate the influence of gear contact. A moderate wind condition at 8 m/s is used with controller disabled. A constant torque resistance (20.058 KN m) was needed and applied to the generator side, the value of which is equivalent to the averaged rotor torque from CFD simulation at a constant rotor speed (see Table 4.5 for the uniform rigid case). The generator torque controller was tested in case set 2 with the turbine operated below the rated condition, and the collective blade pitch controller was applied in case set 3 under a wind speed slightly above the rated condition at 12 m/s, and also a wind speed of 18 m/s, much higher than the rated wind speed. Reference cases 3.6 to 3.9 without controller were included, imposing the rated rotor speed of 12.1 RPM at zero blade pitch angle. Case set 4 was designed to include the bearing representations.

5.3 Results and Discussion

Figure 5.3 shows turbine performance and behavior for the simplest case of an imposed constant torque on the generator at a constant uniform wind speed of 8 m/s. In this case the rotor will accelerate to a constant rotational speed and a resulting constant rotor torque has to balance the generator torque, except for the effect of the tower, clearly seen in Fig. 5.3. Being a more realistic model, the 3-stage gearbox model considers the dynamic transmission error (DTE), an important parameter and main source for noise and vibration of a geared system. The dynamic transmission error along the line of action is defined as $DTE = r_{b1}\theta_1 - r_{b2}\theta_2$ for a gear pair, where θ_1 and θ_2 are the rotational angles

of the driving and driven gear, respectively. r_{b1} and r_{b2} are the base circle radii of the gears. There would be no transmission error for a gear pair in perfect contact with infinite stiffness, as in the case of the 2-DOFs rotor-generator torsional model without gear, yet in reality $DTE \neq 0$ within the drivetrain. As shown in Fig. 5.3, an average 0.256 mm transmission error exists between the ISS and HSS gear pair for the turbine with gear contact, with fluctuations contributed by the external tower shadow and internal gear stages. Transmission errors from all gear pairs within the gearbox lead to variation of the gear ratio, fluctuating within 0.02% about the design value of 97.

Though the variation due to transmission error seems small, it causes noticeable change to the turbine behavior and performance. Comparing with the HSS torque for no gear contact case which averages at the imposed generator torque, the HSS torque from gear contact case exhibits much larger fluctuation and higher mean value due to the transmission error, resulting in a lower HSS speed (-0.4%) with fluctuations in higher frequency. The rotor speed behaves similarly for the gear contact case from the rotor-gearbox-generator interaction, leading to a smaller thrust and higher rotor torque (see Table 5.3 for a quantitative summary). Compared with the case with a constant rotor speed of 9 RPM and uniform wind speed of 8 m/s in Table 4.5, the wind actually accelerates the rotor for both gear contact and no gear contact cases to a higher value about 9.4 RPM, balancing the same generator torque and achieving a similar turbine power, which then causes larger thrust.

When the turbine is operated in turbulent winds, the effect of gear contact is significantly amplified as shown in Fig. 5.4. The internal dynamics represented by gear contact forces between planet 1 and the sun gear, and intermediate stage shaft (ISS) and high speed shaft (HSS) gears show that wind turbulence introduces higher frequency excitations to the gear component with significantly larger amplitude of fluctuations, regardless of the fact that the power amplitude is not affected by the gear contact. The overall gear ratio also shows larger range of fluctuation due to wind turbulence. Slightly

different rotational speeds cause an apparent phase shift which was also observed in uniform wind. Because only torsional DOFs are allowed for the drivetrain components, the two gear contact forces show the same pattern as the torque being transmitted along the drivetrain.

The spectrum analysis in Fig. 5.5 shows quantities of interest in the frequency domain, which are important for fatigue and reliability analyses of rotor and drivetrain. All spectra exhibit peaks at around 0.45 Hz, corresponding to 1/3 of the rotor rotation and essentially showing the effect of individual blades passing by the tower. Lower frequencies have greater influence on power and thrust, as expected when considering the large rotor inertia. This indicates that the drivetrain without a servo system (controller) only has minimal influence on the turbine performance. On the other hand, these low frequency excitations have important influence on the gear loads, as shown by the peaks for the gear contact forces below 2.5 Hz. Beyond this frequency the fluctuations observed on the turbine without a drivetrain are minimal. The gear contact forces show a primary peak at 3 Hz for both uniform and turbulent winds, indicating a characteristic frequency of the drivetrain. It could be possible to trigger resonant vibrations with external loads for this relatively low frequency.

Figure 5.6 shows results with the generator torque controller enabled. The controller seeks to optimize the blade tip speed ratio and regulates an averaged rotor speed of approximately 9.2 RPM at this moderate wind of 8 m/s. The applied generator torque varies with the change of the generator speed, with values higher than the constant generator torque of 20.058 KN-m in Fig. 5.3, resulting in a larger transmission error between the ISS and HSS gear pair. The power remains at 1.9 MW in average, with slower rotor speed and thus smaller tip speed ratio. In addition, the thrust decreases due to the slower rotor speed. In Table 4.4 the simulation results of OC3 case 2.1b using generator torque controller are shown, with values consistent with those shown in Fig. 5.6. Regarding the drivetrain behavior, control of the generator torque to the HSS

introduces extra excitations at higher frequencies, as can be seen by comparing the transmission error and gear ratio in Figs. 5.3 and 5.6.

Turbulent wind dominates the turbine performance and drivetrain behavior for the turbine operated with the generator torque controller, as shown in Fig. 5.7. The trend is determined by the interaction of the wind turbulence and generator torque, which reacts to the rotor speed. The changes in rotor speed change the torque on the generator, and the transmission error and gear contact forces then change proportionally with constant mesh stiffness. Large amplitude fluctuations on gear loads due to turbulent winds can affect drivetrain reliability, as seen in the gear contact forces. On the other hand, little effects are seen on the torque transmission of the geared system, which runs in excellent contact with gear ratio close to the design value. Figure 5.8 shows the influence of the controller in the frequency response. More frequency content is present respect to the cases without controller, and thus may cause more concerns on blade fatigue by the fluctuating loads. It is also clear the important influence of the tower shadow on the rotor, with the primary peaks occurring at about 0.45 Hz and its harmonics. Comparing with the HSS spectrum in Fig. 5.5, the use of the controller amplifies high-frequency fluctuations and induces more high-frequency content. Similar to case set 1, there is a primary peak for the gear loads at 3 Hz in both uniform and turbulent winds, indicating this as a characteristic frequency of the drivetrain.

As discussed earlier, at wind speeds above the rated speed the turbine switches to constant power operation using pitch control. Figure 5.9 shows variables of interest for the turbine operated at wind speed of 18 m/s, which is way beyond the rated condition. As can be seen in Fig. 5.9 and Table 5.3, the power at this high wind averages 5.3 MW, the rated mechanical power, and the rotor speed is maintained at the rated value of 12.1 RPM. For uniform wind cases, the controller shows excellent capability of achieving its control objective with small fluctuations, while for turbulent wind in which the wind speed could be as high as the cut-out speed of 25 m/s, the controller performs fairly well

but shows high amplitude fluctuations. Note that the turbine thrust is well within 400 KN for all cases, a better performance than the moderate wind cases without the blade pitch controller (see case sets 1 and 2 in Table 5.3). This is a desirable consequence to having a blade pitch controller for both stand-alone turbines and several turbines as in a wind farm, as loads and the wake are reduced. The blade pitch controller also reduces gear-load fluctuations under turbulent winds, keeping similar amplitude with the uniform wind cases, as compared with the gear contact force between ISS and HSS gears in Figs. 5.9 and 5.7. As the blade pitch angles were dynamically regulated, the average pitch angle in uniform wind is approximately 14 degrees for the turbine with flexible blades and 14.6 degrees for the rigid blades, while the turbine with flexible blades in turbulent wind sees pitch variations between 13.5 and 15.8 degrees. Blade pitch angles exhibit periodic variations in uniform wind when tower and tilt effects are evident, increasing the pitch angle and thus decreasing the angle of attack when blade is approaching to the tower from turbine top to bottom, and decreasing the pitch angle from bottom to top when blade rotates away from the tower. Table 5.3 also shows results for wind turbine with the controller disabled at high winds. This scenario leads to much larger thrust and torque, and therefore places the turbine in a dangerous operational condition of damaging the drivetrain by the off-design torsional loads and the large rotor loads. In addition to the high wind condition, a wind speed of 12 m/s was also included for completeness, which is slightly higher than the rated condition. The blade pitch angles were regulated at about 3 degrees as to achieve the rated power of 5.3 MW for both rigid and flexible turbines, and the thrusts were smaller than the cases at wind speed of 11.4 m/s with fixed zero pitch shown in Table 4.7.

Figure 5.10 shows the frequency spectra of rotor power, blade pitch, gear contact force, rotor and HSS speed. As was the case with the moderate wind cases, the tower's shadow shows its influence on power at its corresponding frequency about 0.6 Hz and higher harmonics, but in contrast, the energy content tends to be distributed evenly for the

three main harmonics due to the blade pitch controller. Also note that blade elasticity has the effect of mitigating the gear loads as shown in Figs. 5.9 and 5.10 for the gear contact forces at HSS, but it also introduces additional frequency responses in the low frequency range. Comparing with the HSS speed spectrum without controller in Fig. 5.5 and with generator torque controller in Fig. 5.8, the blade pitch controller significantly amplifies amplitude of the peaks and induces more frequency content in the low-frequency range due to the large rotor inertia and slow rate of change of the blade pitch shown in the blade pitch spectrum.

Figure 5.11 compares the blade tip deflections for the high wind condition of 18 m/s. The tower shadow influence remains an important factor to increasing the blade-tower clearance for a turbine operating with a blade pitch controller. When the controller is enabled, as for typical utility-scale turbines, averaged OoP deflections in both uniform and turbulent winds are reduced by a factor of 4 to 1.9 m, compared with the 7.7 m deflection observed for a turbine without a controller and at constant zero pitch. Such deflections are even smaller than those in a moderate wind of 8 m/s with no controller in place (See Table 4.6), contributing to reduce risks of structural damage while producing high power. For IP deflection, the high wind further pushes it towards the leading edge as compared to the moderate and rated wind speeds shown in Figs. 4.17 and 4.19, and the blade pitch controller contributes to mitigate these trends by increasing the pitch angle and the consequent higher stiffness in the IP direction.

As previously mentioned, a beneficial consequence of an active blade pitch controller is a decreased wake, as shown in Figs. 5.12 and 5.13 for a wind speed of 18 m/s. Figure 5.12 shows an instantaneous velocity contour on a horizontal cross section at an elevation $z = 60\,m$ at the end of the 10^{th} rotation, with non-dimensional axial velocity ranging from 0.4 to 1.0. The location of the cross section corresponds to the mid-span of blade 1 at state of the turbine. When the turbine is operating in uniform wind at zero degree pitch and without controller, the momentum loss on the blades and tips are

clearly visible, with the resulting significant velocity deficit on the wake to the end of the simulation domain 5-radii (315 m) downstream. With a blade pitch controller, the blade tip deflections are dramatically reduced due to the much smaller thrust. The velocity deficit on the wake is also reduced significantly with much less influence from the rotating blades, and the main contribution is from the tower shadow. Note that tower-induced velocity deficit tends to be asymmetric, resulting from the induced angular swirl by the rotor. The pitch controller shows similar influence for the turbine operating in turbulent winds, effectively reducing blade deflections and velocity deficit of the wake. This design decreasing the power by reducing the angle of attack is beneficial to wind farm operation, as opposed to control by stalling the flow on the blades which reduces the power at the cost of increased stress and higher velocity deficit on the wake.

Figure 5.13 shows average axial velocity profiles on the wake at different axial positions at a horizontal line located at $z = 60\,m$. The velocities were obtained after averaging 5 complete consecutive rotor rotations. No-controller cases show axial velocities varying from 0.7 to 1 along the axial positions, compared to the cases with controller enabled with axial velocities ranging from 0.85 to 1. The width of the wake is similar for the cases with and without pitch controller, but the velocity deficit is a factor of 3 higher for the case without controller. As expected, the cases with turbulence show a wider wake but still the width is similar with and without active pitch control. The case without controller also shows that the tower wake has moved to starboard three times more than the pitch-controlled case, evidencing a much stronger tangential induction factor when the controller is disabled, again consistent with a higher axial induction factor reflected in a stronger wake. This analysis of wake flow is important in that it could provide valuable information for turbine placement in wind farms.

Figure 5.14 shows results of computations enabling the bearing model in Virtual.Lab for the case of a moderate wind of 8 m/s. With the regulation of the generator torque controller, the bearings have minimum influence on the general turbine

performance (see also Table 5.3 for quantitative results). The drivetrain tends to experience less fluctuations with bearing clearance, which damps the gear contact force and gear ratio significantly. The bearing clearance also reduces the amplitude and fluctuation of the transmission error, which then changes the HSS torque proportionally and leads to higher rotor speed and larger thrust. In addition, when the turbine is operating in turbulent wind, the radial displacement of the bearings is subject to larger amplitude fluctuations and higher frequency, causing potential issues for shaft alignment and gearbox stability.

5.4 Summary

In this chapter, a drivetrain model and control systems were incorporated into the simulation tool with the proposed coupled CFD/MBD approach, enabling capabilities to investigate interaction between turbulent wind, rotor aerodynamics, elastic blades, drivetrain dynamics at the gear-level and servo-control dynamics. This unique tool has the potential to provide useful insight for wind turbine design.

Extensive simulations of increasing complexity were performed to demonstrate and validate the implemented model. The effect of gear contact including dynamic transmission error was shown in a moderate wind, resulting in a decreased thrust and rotational speed on the turbine. The use of a generator torque controller helps to improve the power efficiency and reduce thrust, at the cost of inducing excitations at higher frequencies but with minimal influence on the gear loads. Wind turbulence was shown to significantly increase the gear loads, independent of the generator torque controller. The blade pitch controller efficiently regulates the turbine to maintain the constant rated power and generator speed, which also is useful in reducing thrust, a great benefit for both stand-alone turbines and wind farms. In addition, bearing clearance is found to relieve gear-level loads in both amplitude and frequency.

Table 5.1 Drivetrain properties

Drivetrain structural properties			
Rotor inertia	38759228 kg m^2		
Generator inertia about HSS	534.116 kg m^2		
Generator inertia about LSS	5025500 kg m^2		
Equivalent driveshaft torsional-spring constant	867637000 N m/rad		
Equivalent driveshaft torsional-damping constant	6215000 N m/(rad/s)		
Hub inertia about rotor axis	115926 kg m^2		
Gearbox basic properties			
Rated generator speed	1173.7 RPM		
Gear ratio	1:97		
Planetary stage			
	Ring gear	Planet gear	Sun gear
Number of teeth	97	39	21
Normal module (mm)	10	10	10
Normal pressure angle (deg)	20	20	20
Helix angle (deg)	7.495	7.495	7.495
Young's modulus (N m^2)	2e11	2e11	2e11
Intermediate stage			
	ISS gear	ISS pinion	
Number of teeth	82	23	
Normal module (mm)	8.25	8.25	
Normal pressure angle (deg)	20	20	
Helix angle (deg)	14	14	
Young's modulus (N m^2)	2e11	2e11	
High speed stage			
	HSS gear	HSS pinion	
Number of teeth	92	19	
Normal module (mm)	5	5	
Normal pressure angle (deg)	20	20	
Helix angle (deg)	14	14	
Young's modulus (N m^2)	2e11	2e11	

Table 5.2 Simulation conditions for drivetrain dynamics

Case Set		Wind Type	Wind Speed	Blade Flexibility	Gear Contact	Controller	Bearing
1	1.1	Uniform	8 m/s	Rigid	No	No	No
	1.2	Turbulent					
	1.3	Uniform			Yes		
	1.4	Turbulent					
2	2.1	Uniform	8 m/s	Rigid	No	Generator Torque	No
	2.2	Turbulent					
	2.3	Uniform			Yes		
	2.4	Turbulent					
3	3.1	Uniform	12 m/s	Rigid	Yes	Blade Pitch	No
	3.2	Uniform		Flexible			
	3.3	Uniform	18 m/s	Rigid			
	3.4	Uniform		Flexible			
	3.5	Turbulent		Flexible			
	3.6	Uniform		Rigid		No	
	3.7	Turbulent		Rigid			
	3.8	Uniform		Flexible			
	3.9	Turbulent		Flexible			
4	4.1	Uniform	8 m/s	Flexible	Yes	Generator Torque	Yes
	4.2	Turbulent		Flexible			

Table 5.3 Summary of wind turbine behavior for drivetrain dynamics

Case Set		Power [MW] Mean/σ	Thrust [KN] Mean/σ	Rotor Speed [RPM] Mean/σ	Blade Pitch [deg] Mean/σ
1	1.1	1.923/0.025	410.01/2.59	9.409/0.002	0/0
	1.2	1.864/0.238	420.31/27.85	9.932/0.192	0/0
	1.3	1.920/0.026	408.38/2.72	9.368/0.002	0/0
	1.4	1.866/0.238	417.60/27.91	9.845/0.193	0/0
2	2.1	1.920/0.026	403.81/2.74	9.225/0.005	0/0
	2.2	1.942/0.373	404.22/45.06	9.262/0.397	0/0
	2.3	1.919/0.027	402.24/2.80	9.178/0.005	0/0
	2.4	1.942/0.372	403.53/44.72	9.223/0.390	0/0
3	3.1	5.356/0.084	643.15/6.16	12.095/0.008	2.927/0.060
	3.2	5.313/0.078	653.36/6.22	12.095/0.009	3.410/0.061
	3.3	5.361/0.194	374.22/9.89	12.099/0.008	14.596/0.021
	3.4	5.331/0.162	375.75/8.50	12.099/0.006	14.098/0.018
	3.5	5.231/0.580	357.04/28.39	12.112/0.127	14.882/0.414
	3.6	14.428/0.148	1154.34/4.31	12.1/0	0/0
	3.7	14.260/0.954	1144.10/34.89	12.1/0	0/0
	3.8	11.930/0.140	1097.53/5.71	12.1/0	0/0
	3.9	11.904/0.730	1097.41/36.92	12.1/0	0/0
4	4.1	1.912/0.026	418.31/2.77	9.211/0.023	0/0
	4.2	1.910/0.331	418.27/44.15	9.245/0.365	0/0

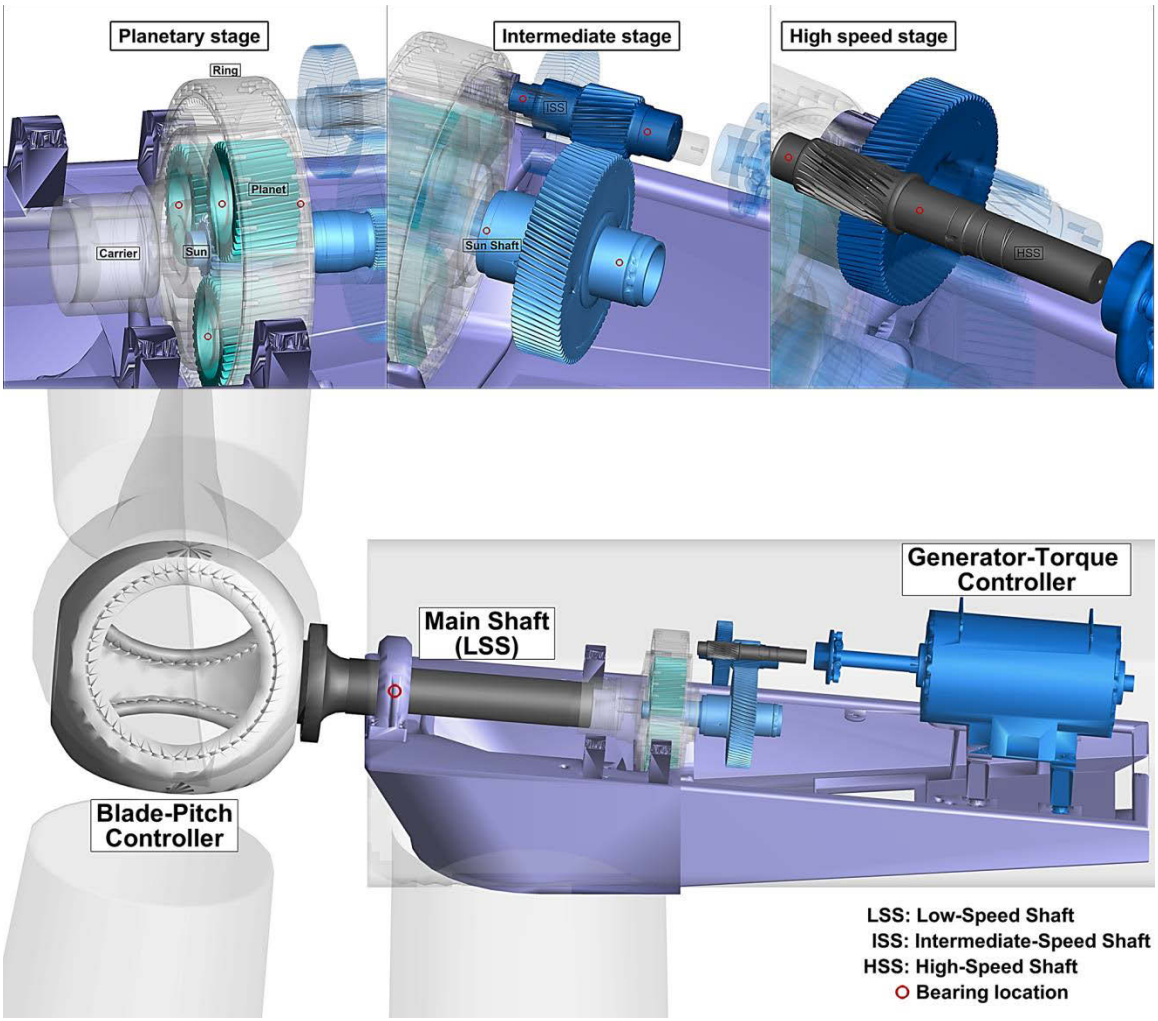

Figure 5.1 Drivetrain model configuration

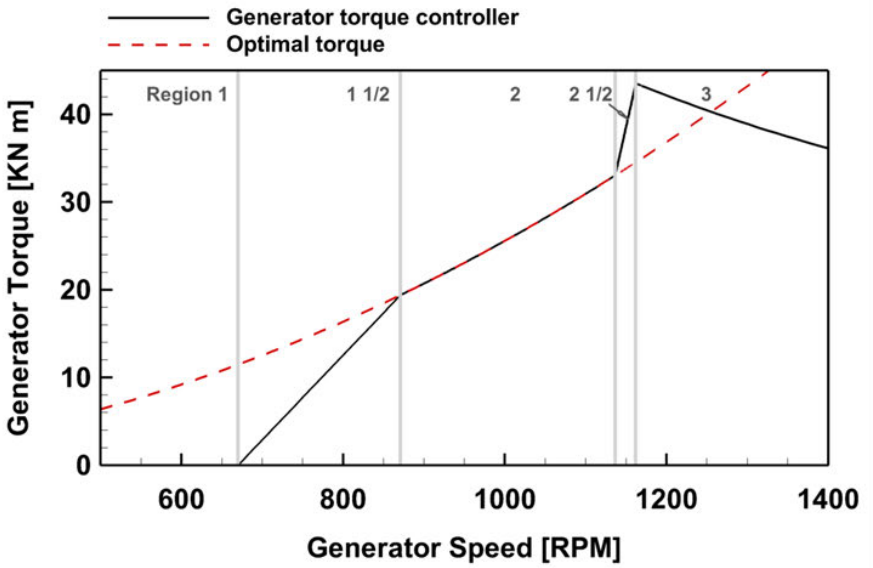

(a) Generator torque controller

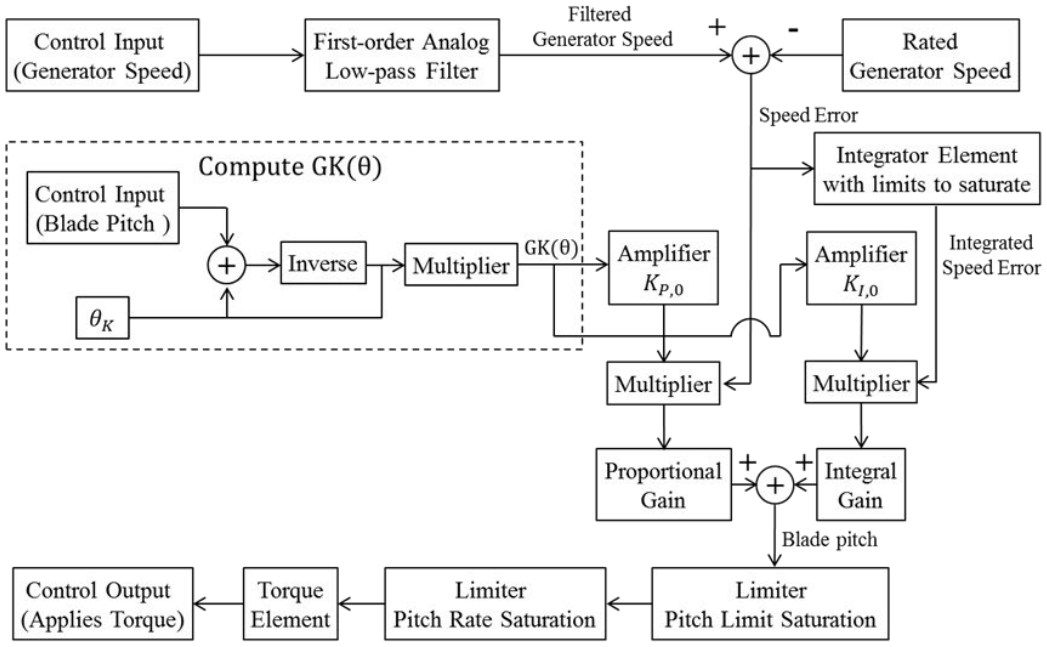

(b) Blade pitch controller

Figure 5.2 Wind turbine control system

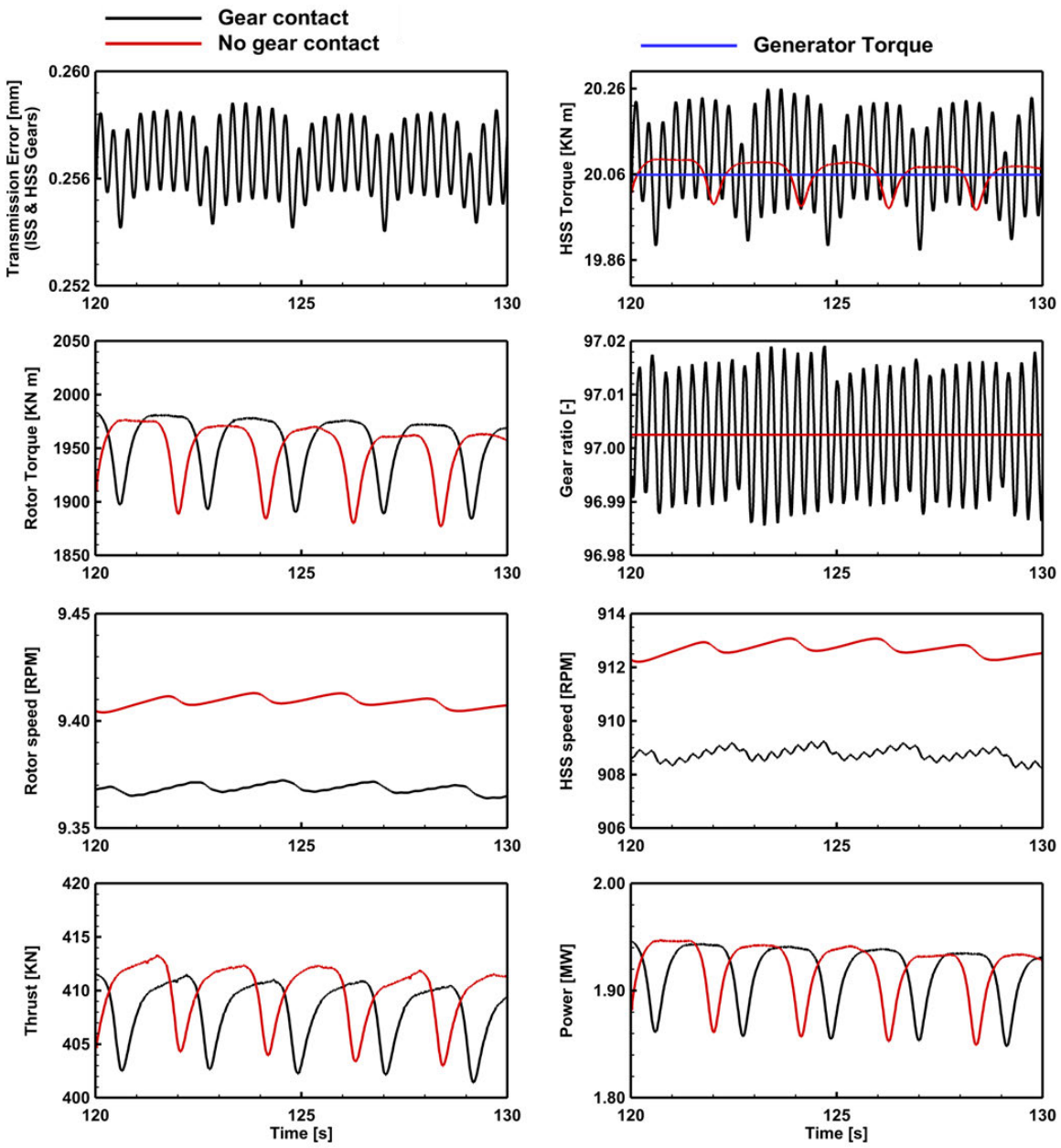

Figure 5.3 Gear contact influence at uniform wind speed 8 m/s

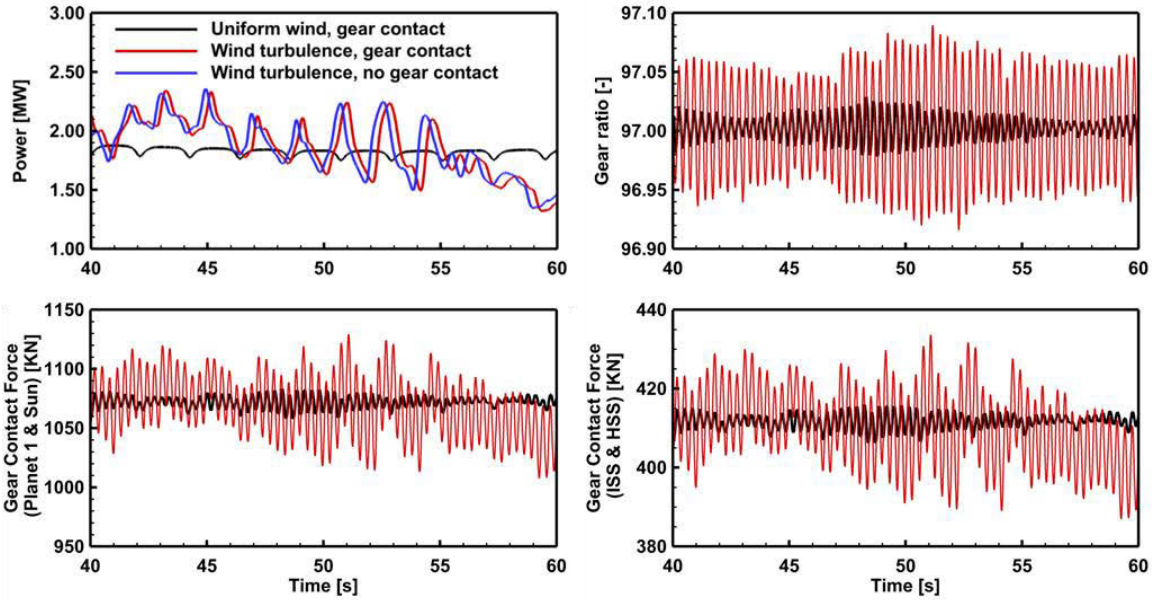

Figure 5.4 Wind turbulence influence on gear contact at wind speed 8 m/s

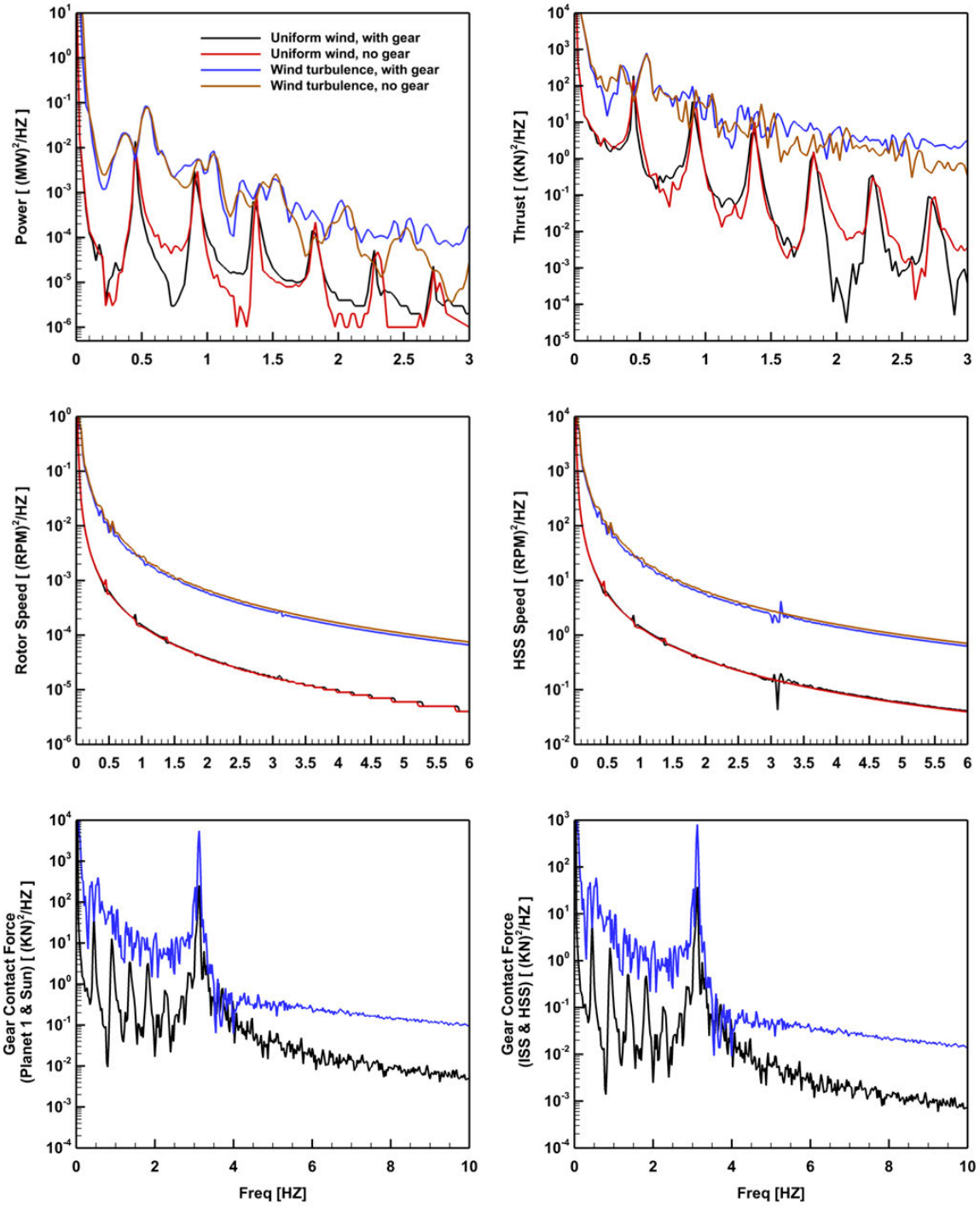

Figure 5.5 Power spectrum density at wind speed 8 m/s

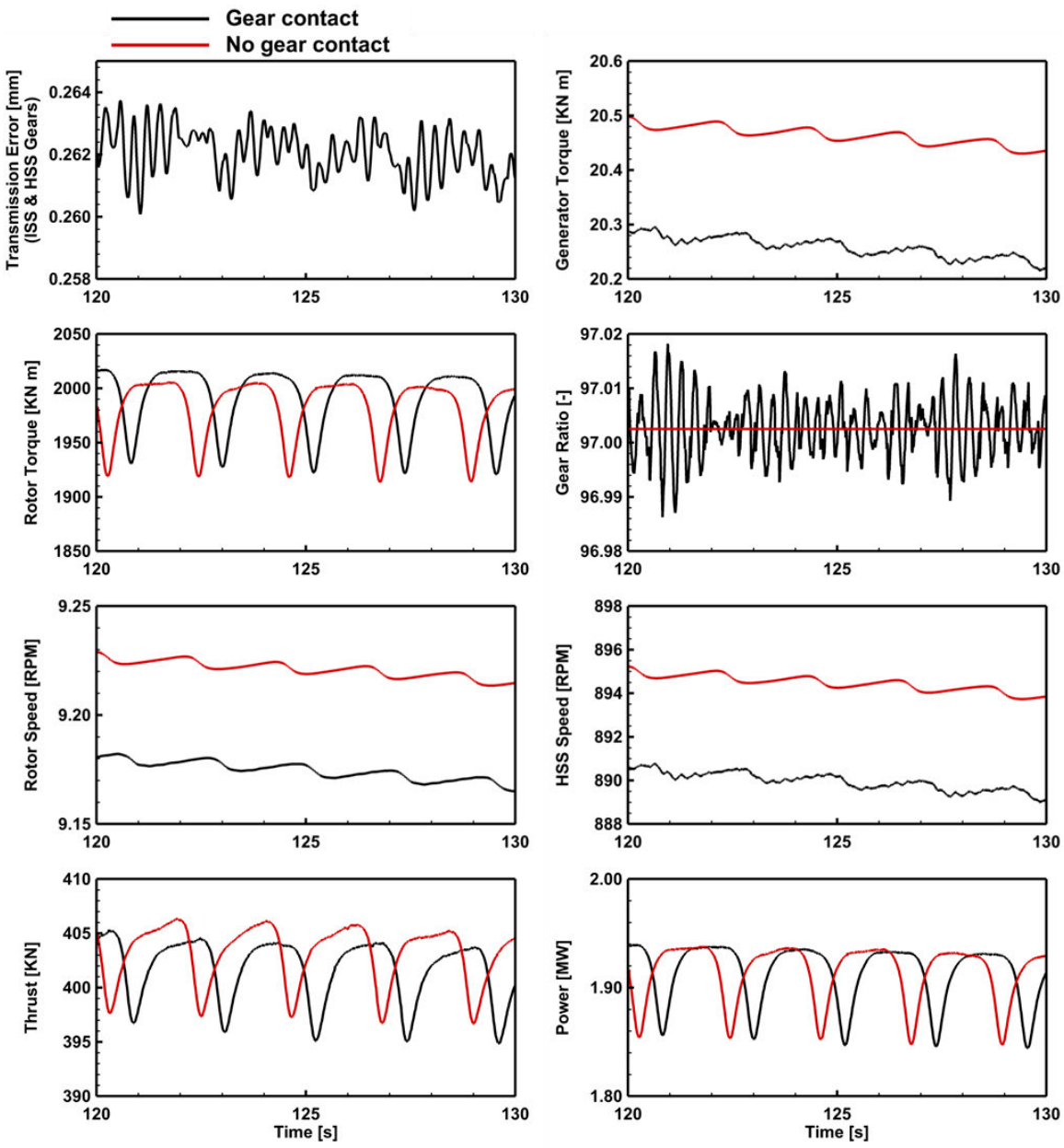

Figure 5.6 Effect of generator torque controller at wind speed 8 m/s

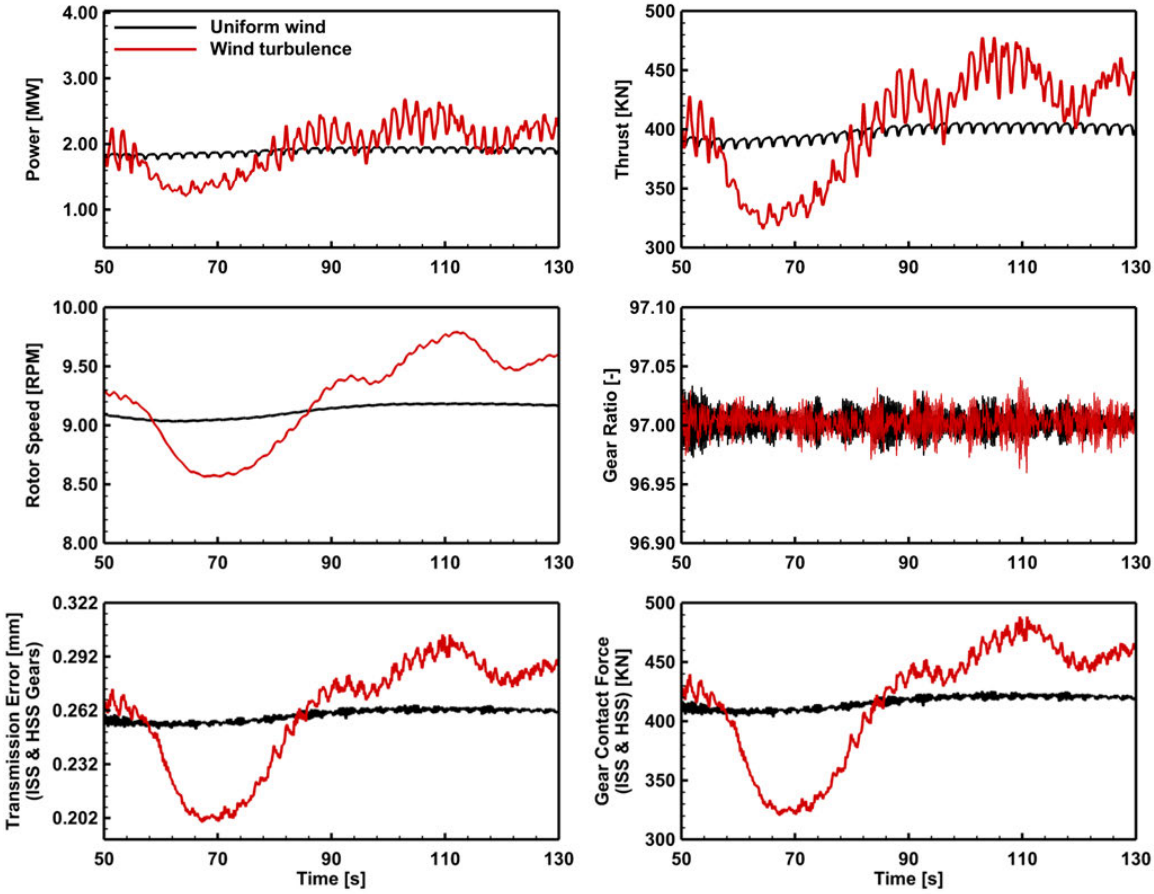

Figure 5.7 Wind turbulence influence on gear contact with controller at wind speed 8 m/s

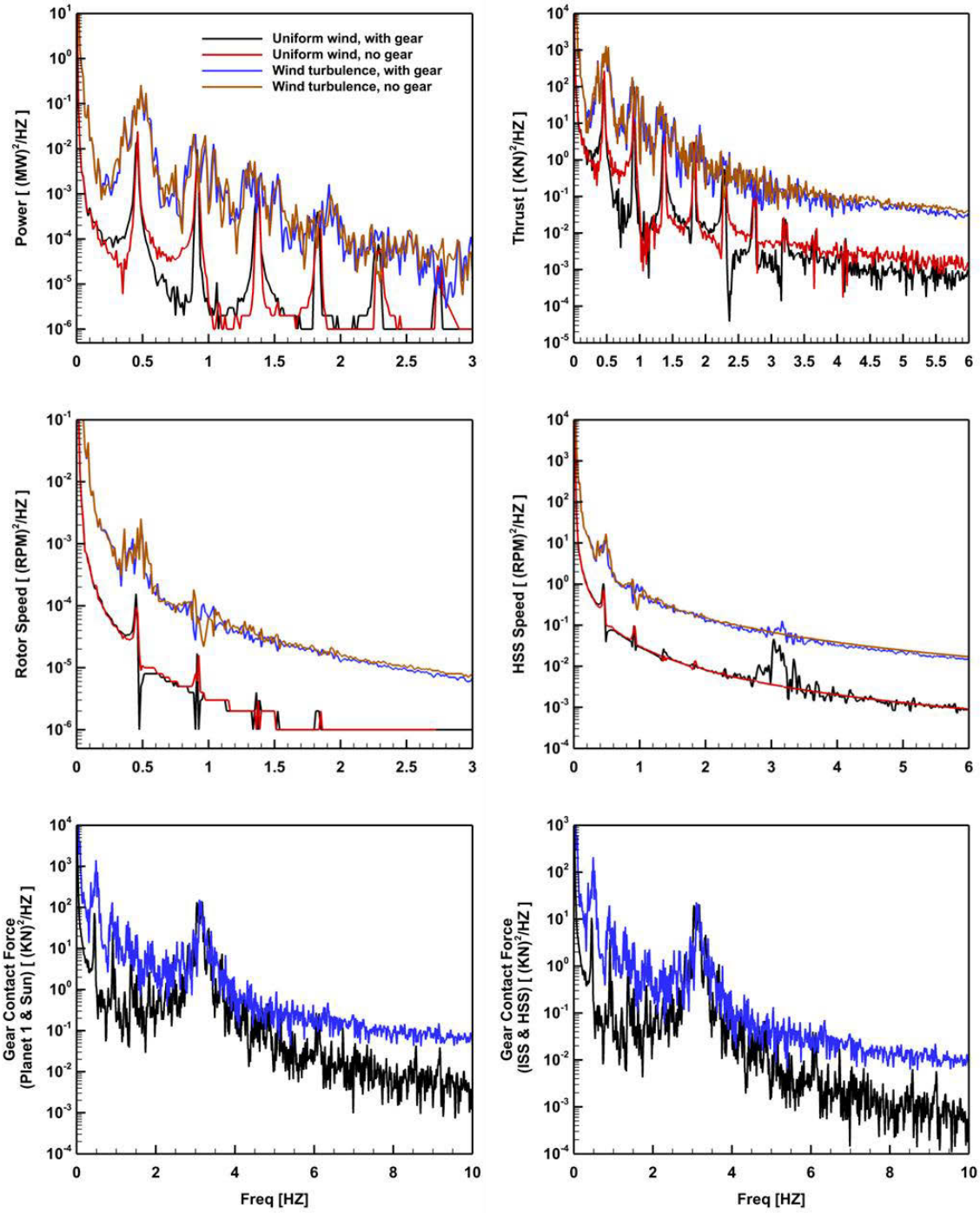

Figure 5.8 Power spectrum density with generator torque controller at wind speed 8 m/s

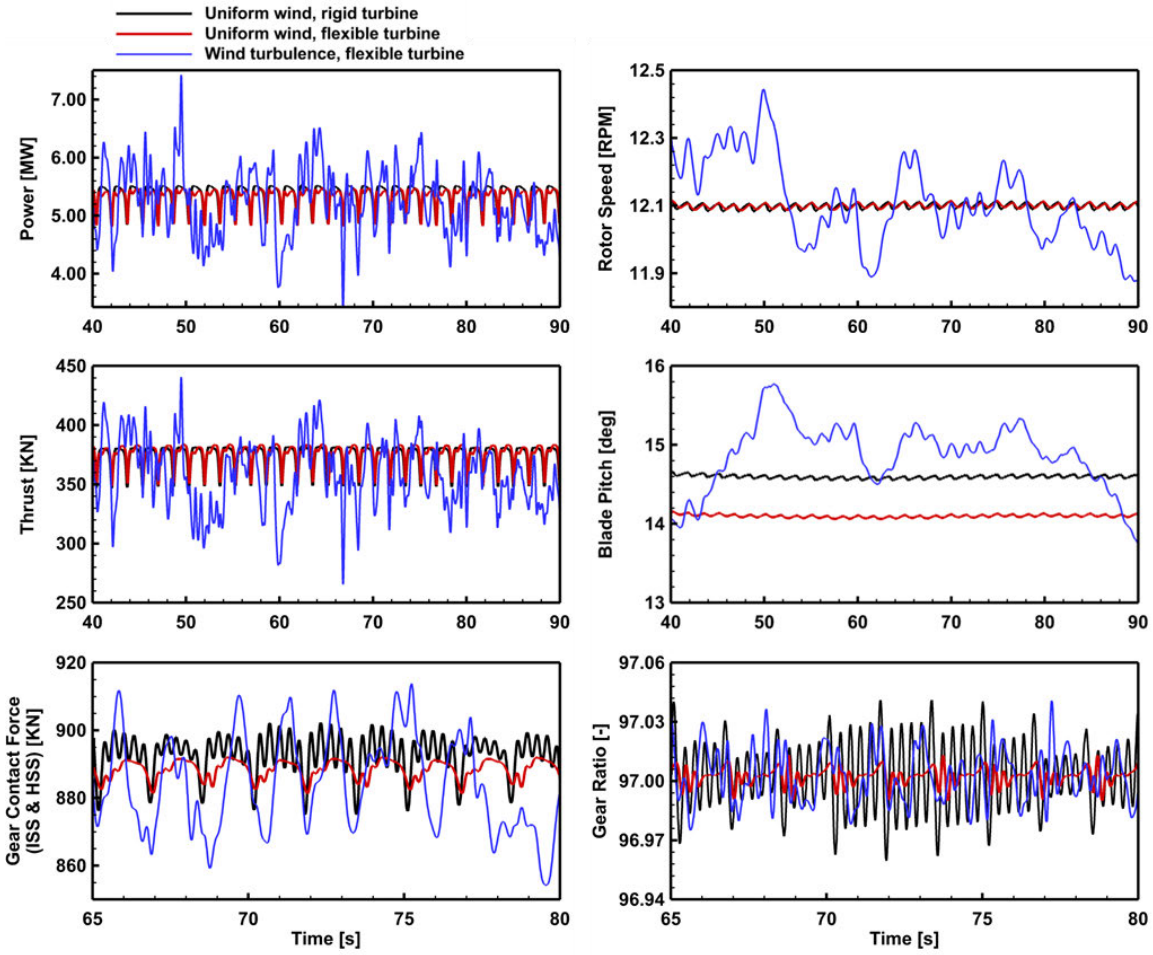

Figure 5.9 Effect of blade pitch controller at wind speed 18 m/s

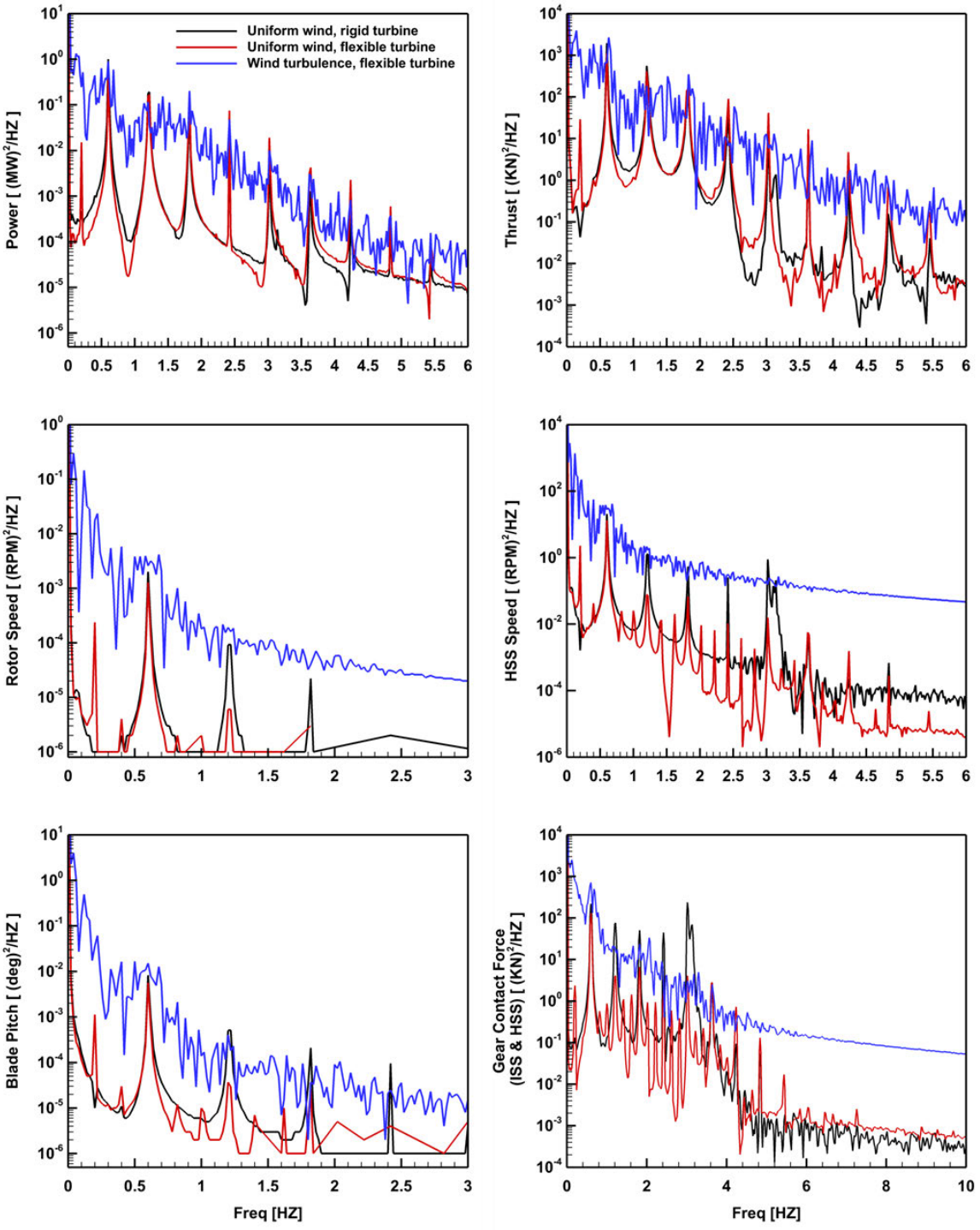

Figure 5.10 Power spectrum density with blade pitch controller at wind speed 18 m/s

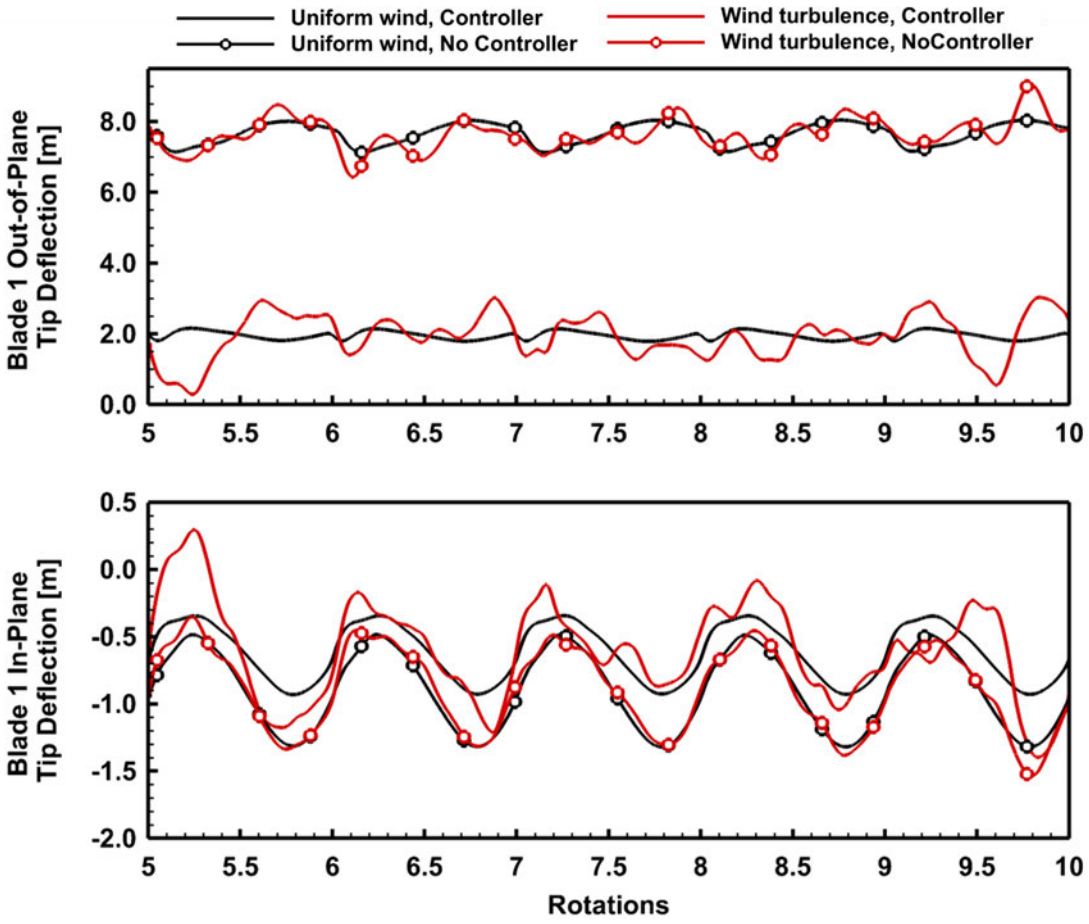

Figure 5.11 Blade tip deflections at wind speed 18 m/s

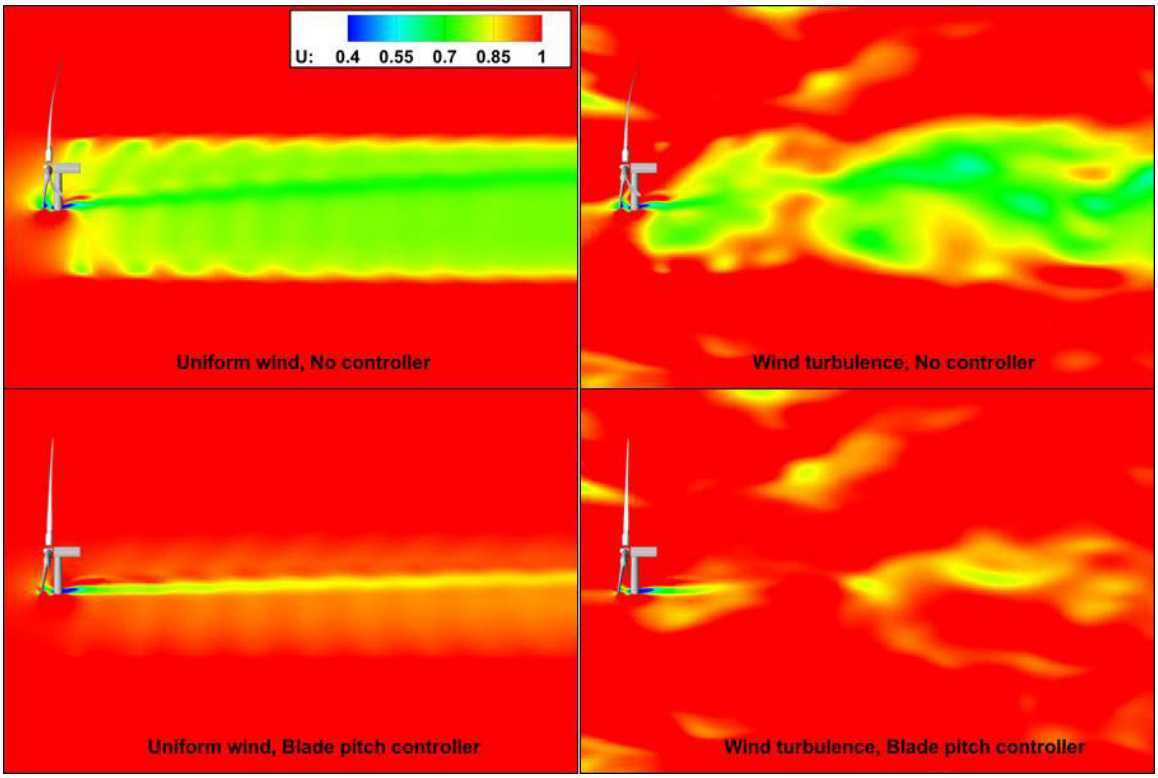

Figure 5.12 Instantaneous non-dimensional axial velocity contour at $z = 60\,m$ with flexible blades at wind speed 18 m/s

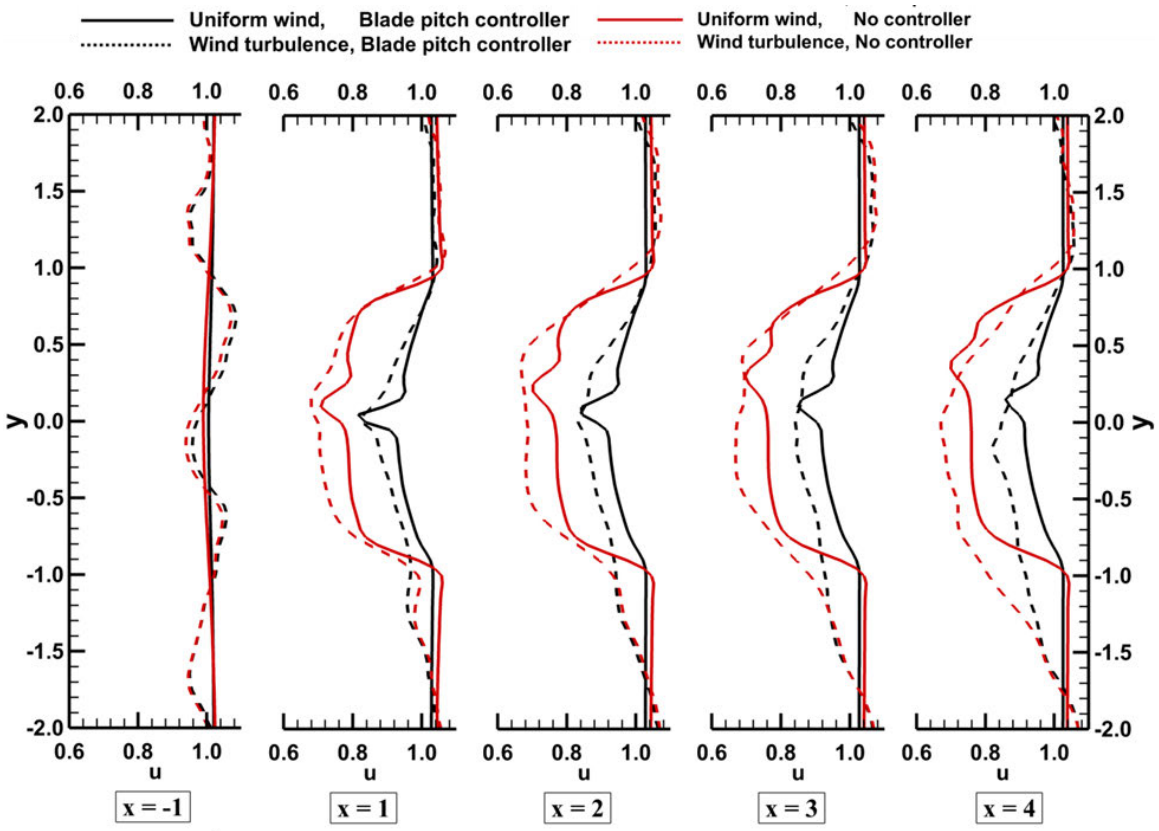

Figure 5.13 Axial velocities at different axial positions and at $z = 60\,m$ for wind speed 18 m/s

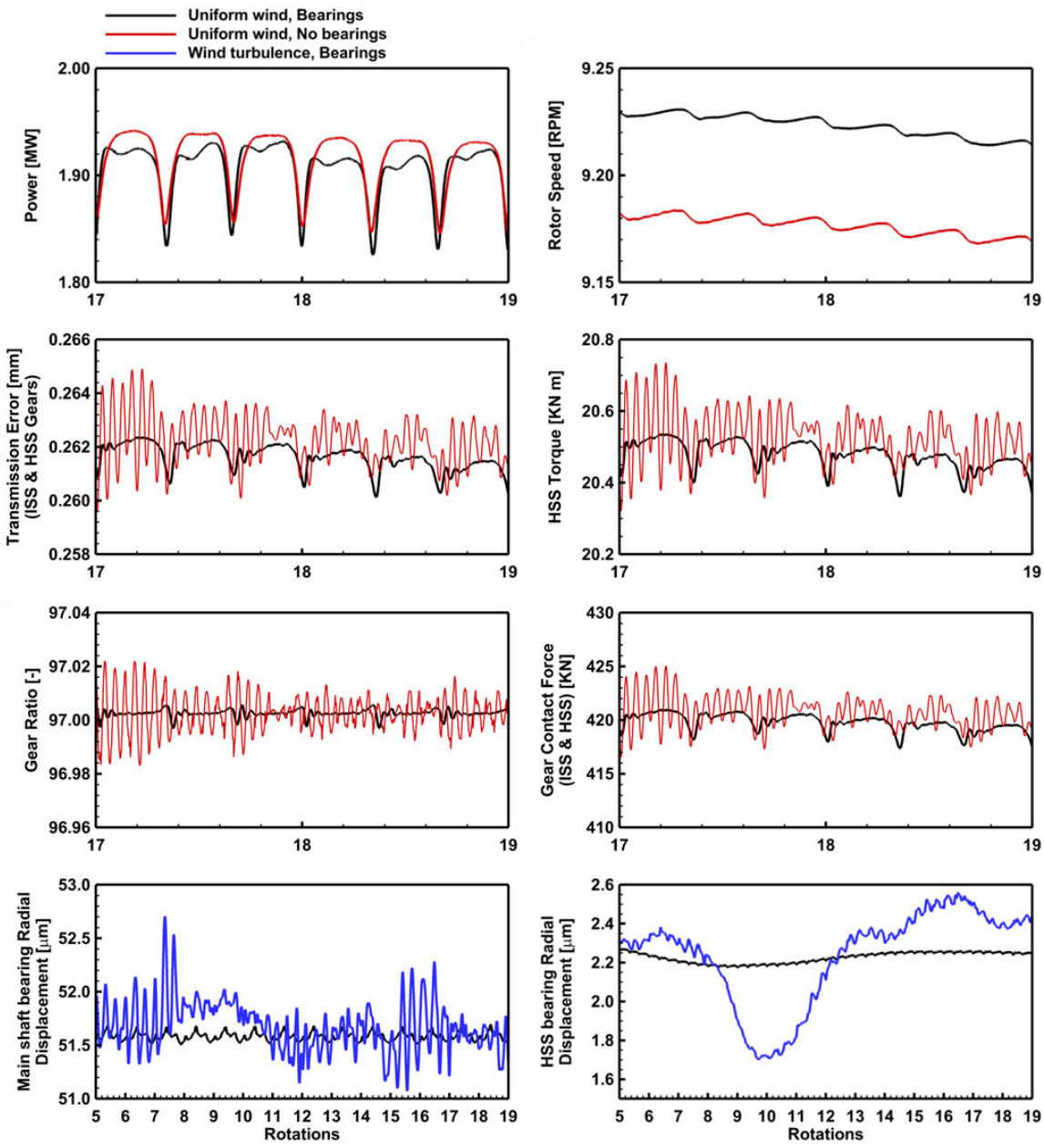

Figure 5.14 Effect of bearing at wind speed 8 m/s

CHAPTER 6

CONCLUSIONS AND FUTURE WORK

A high fidelity approach coupling CFD and MBD was presented. The approach has the potential for simulating on-shore and off-shore wind turbines under complex operational conditions including blade elasticity, drivetrain dynamics, and atmospheric wind shear and turbulence.

The performance of the CFD dynamic overset flow solver for wind turbine simulations was demonstrated by extensive comparison with the benchmark experiment UAE phase VI. In particular, operational conditions with both variable wind speed at fixed blade pitch angle and variable blade pitch angle at fixed wind speed were simulated. Simulations were performed in full scale with the exact geometry of the blades, and approximate geometries for hub, nacelle and tower. Both RANS and DES turbulence models were used in the simulations. Results show that CFD predictions match the experimental data consistently well, including the general trends for power and thrust, sectional normal force and pressure coefficients at different sections along the blade. At very large angles of attack the conditions are more demanding and the CFD results tend to slightly overpredict the thrust and underpredict the power. Evaluation of the transient pressure on the blades reveals that DES is able to predict fluctuations with similar frequencies to the experimental measurements.

In order to investigate the influence of the atmospheric wind turbulence, the wind turbulence model developed by Mann and recommended by IEC 61400-1 ed. 3 and used by OC3 project was implemented into the code as an explicit inlet boundary and initial conditions. The model was validated both theoretically and statistically by comparing the generated stationary wind turbulence field with the theoretical one-point spectrum for the three components of the velocity fluctuations, and by comparing the expected statistics

from the simulated turbulent field by CFD with the explicit wind turbulence inlet boundary from the Mann model.

Demonstrations of the proposed coupled approach were conducted for the conceptual NREL 5MW offshore wind turbine, and extensive comparisons were made against the publicly available OC3 simulations results, covering aerodynamic predictions, turbine performance and blade response for flexible turbine with and without wind turbulence, as well as detailed analysis for turbine behavior and flow field. Results compare well with those from OC3 participants in time and frequency domains.

The Gearbox Reliability Collaborative project gearbox was up-scaled in size and added to the NREL 5MW turbine with the purpose of demonstrating drivetrain dynamics. Generator torque and blade pitch controllers were implemented to simulate realistic operational conditions of commercial wind turbines. Interactions between turbulent wind, rotor aerodynamics, elastic blades, drivetrain dynamics at the gear-level and servo-control dynamics were studied. The tool and methodology developed are unique, with this thesis being the first time a complete wind turbine is simulated including CFD of the rotor/tower aerodynamics, elastic blades, gearbox dynamics and feedback control systems.

Future work will focus on the development and implementation of a farm simulation tool with scalability to hundreds of turbines, with the goal of studying farm power production optimization and drivetrain stress minimization. Improvements to the model of the drivetrain are also considered as future work.

REFERENCES

Archer, Cristina L., and Mark Z. Jacobson. 2005. "Evaluation of Global Wind Power." *Journal of Geophysical Research* 110 (D12): D12110.

Baldwin, B. S., and H. Lomax. 1978. *Thin Layer Approximation and Algebraic Model for Separated Turbulent Flows*. Vol. 257. American Institute of Aeronautics and Astronautics.

Bauchau, O. A, C. L. Bottasso, and Y. G. Nikishkov. 2001. "Modeling Rotorcraft Dynamics with Finite Element Multibody Procedures." *Mathematical and Computer Modelling* 33 (10): 1113–37.

Bauchau, O. A. 1998. "Computational Schemes for Flexible, Nonlinear Multi-Body Systems." *Multibody System Dynamics* 2 (2): 169–225.

Bauchau, O. A., and D. H. Hodges. 1999. "Analysis of Nonlinear Multibody Systems with Elastic Couplings." *Multibody System Dynamics* 3 (2): 163–88.

Bazilevs, Y., M-C. Hsu, I. Akkerman, S. Wright, K. Takizawa, B. Henicke, T. Spielman, and T. E. Tezduyar. 2011. "3D Simulation of Wind Turbine Rotors at Full Scale. Part I: Geometry Modeling and Aerodynamics." *International Journal for Numerical Methods in Fluids* 65 (1-3): 207–35. doi:10.1002/fld.2400.

Bazilevs, Y., M-C. Hsu, J. Kiendl, R. Wüchner, and K-U. Bletzinger. 2011. "3D Simulation of Wind Turbine Rotors at Full Scale. Part II: Fluid-Structure Interaction Modeling with Composite Blades." *International Journal for Numerical Methods in Fluids* 65 (1-3): 236–53. doi:10.1002/fld.2454.

Bazilevs, Y., M-C. Hsu, and M. A. Scott. 2012. "Isogeometric Fluid–structure Interaction Analysis with Emphasis on Non-Matching Discretizations, and with Application to Wind Turbines." *Computer Methods in Applied Mechanics and Engineering* 249-252 (December): 28–41. doi:10.1016/j.cma.2012.03.028.

Bechmann, A. 2006. "Large-Eddy Simulation of Atmospheric Flow over Complex Terrain." Doctoral dissertation, Roskilde, Denmark: Risø National Laboratory, Technical University of Denmark.

Biedron, R. T., and E. M. Lee-Rausch. 2008. "Rotor Airloads Prediction Using Unstructured Meshes and Loose CFD/CSD Coupling." In *26th AIAA Applied Aerodynamics Conference*. Honolulu, HI, United States.

Boger, David A., and James J. Dreyer. 2006. "Prediction of Hydrodynamic Forces and Moments for Underwater Vehicles Using Overset Grids." *AIAA Paper* 1148.

Brenan, Kathryn Eleda, Stephen La Vern Campbell, and Linda Ruth Petzold. 1989. *Numerical Solution of Initial-Value Problems in Differential-Algebraic Equations*. Vol. 14. Siam.

Buning, Pieter G., Steven J. Parks, William M. Chan, and Kevin J. Renze. 1991. "Application of the Chimera Overlapped Grid Scheme to Simulation of Space Shuttle Ascent Flows." In *the 4th International Symposium on Computational Fluid Dynamics* , 132–37. Davis, California.

Carrica, P. M., J. Huang, R. Noack, D. Kaushik, B. Smith, and F. Stern. 2010. "Large-Scale DES Computations of the Forward Speed Diffraction and Pitch and Heave Problems for a Surface Combatant." *Computers & Fluids* 39 (7): 1095–1111. doi:10.1016/j.compfluid.2010.02.002.

Carrica, P. M., R. V. Wilson, R. W. Noack, and F. Stern. 2007. "Ship Motions Using Single-Phase Level Set with Dynamic Overset Grids." *Computers & Fluids* 36 (9): 1415–33. doi:10.1016/j.compfluid.2007.01.007.

Carrica, P. M., R. V. Wilson, and F. Stern. 2007. "An Unsteady Single-Phase Level Set Method for Viscous Free Surface Flows." *International Journal for Numerical Methods in Fluids* 53 (2): 229–56. doi:10.1002/fld.1279.

Dousset, Vincent, and Alban Pothérat. 2010. "Formation Mechanism of Hairpin Vortices in the Wake of a Truncated Square Cylinder in a Duct." *Journal of Fluid Mechanics* 653: 519.

Duque, E. P., M. D. Burklund, and W. Johnson. 2003. "Navier-Stokes and Comprehensive Analysis Performance Predictions of the NREL Phase VI Experiment." *Journal of Solar Energy Engineering* 125 (4): 457–67.

Faulstich, Stefan, M. Durstewitz, B. Hahn, K. Knorr, and K. Rohrig. 2008. "Wind Energy Report Germany 2008." Institut für Solare Energieversorgungstechnik (ISET).

Fingersh, Lee Jay, Dave Simms, Maureen Hand, Dave Jager, Jason Cotrell, Mike Robinson, Scott Schreck, and Scott Larwood. 2001. "Wind Tunnel Testing of NREL's Unsteady Aerodynamics Experiment." *AIAA Paper* 35: 2001.

Frigo, M, and SG Johnson. 2005. "The Design and Implementation of FFTW3." *Proceedings of the IEEE* 93 (2): 216–31.

Fuglsang, P., I. Antoniou, C. Bak, and H. Aagaard Madsen. 1998. "Wind Tunnel Test of the RISØ-1 Airfoil." Technical Report Risø-R-999(EN). Risø National Laboratory, Roskilde.

Fuglsang, P., C. Bak, J. G. Schepers, B. Bulder, T. T. Cockerill, P. Claiden, A. Olesen, and R. van Rossen. 2002. "Site-Specific Design Optimization of Wind Turbines." *Wind Energy* 5 (4): 261–79. doi:10.1002/we.61.

Glauert, H. 1963. *Airplane Propellers*. In: W.F. Durand (Ed.) Aerodynamic Theory. New York: Dover Publications.

Global Wind Energy Council. 2013. *Global Wind Report 2012-Annual Market Update*.

Gritskevich, M. S., A. V. Garbaruk, J. Schütze, and F. R. Menter. 2011. "Development of DDES and IDDES Formulations for the K-Ω Shear Stress Transport Model." *Flow, Turbulence and Combustion* 88 (3): 431–49. doi:10.1007/s10494-011-9378-4.

Haase, W. 1997. *ECARP: European Computational Aerodynamics Research Project: Validation of CFD Codes and Assessment of Turbulence Models*. Vol. 58. Friedr Vieweg & Sohn Verlagsgesellschaft.

Hand, M.M., D.A. Simms, L.J. Fingersh, D.W. Jager, J.R. Cotrell, S. Schreck, and S.M. Larwood. 2001. "Unsteady Aerodynamics Experiment Phase VI: Wind Tunnel Test Configurations and Available Data Campaigns." Technical Report NREL/TP-500-29955. National Renewable Energy Laboratory.

Hansen, M., J. N. Sørensen, S. Voutsinas, N. Sørensen, and H. A. Madsen. 2006. "State of the Art in Wind Turbine Aerodynamics and Aeroelasticity." *Progress in Aerospace Sciences* 42 (4): 285–330.

Haug, E. J. 1989. *Computer Aided Kinematics and Dynamics of Mechanical Systems*. Vol. 1. Allyn and Bacon Boston.

Heege, Andreas, Jaume Betran, and Yvan Radovcic. 2007. "Fatigue Load Computation of Wind Turbine Gearboxes by Coupled Finite Element, Multi-Body System and Aerodynamic Analysis." *Wind Energy* 10 (5): 395–413. doi:10.1002/we.226.

Hess, John L. 1975. "Review of Integral-Equation Techniques for Solving Potential-Flow Problems with Emphasis on the Surface-Source Method." *Computer Methods in Applied Mechanics and Engineering* 5 (2): 145–96.

Hsu, M-C., I. Akkerman, and Y. Bazilevs. 2013. "Finite Element Simulation of Wind Turbine Aerodynamics: Validation Study Using NREL Phase VI Experiment." *Wind Energy*. doi:10.1002/we.1599.

Hsu, M-C., and Y. Bazilevs. 2012. "Fluid–structure Interaction Modeling of Wind Turbines: Simulating the Full Machine." *Computational Mechanics* 50 (6): 821–33. doi:10.1007/s00466-012-0772-0.

Huang, J., P. M. Carrica, and F. Stern. 2008. "Semi-Coupled Air/water Immersed Boundary Approach for Curvilinear Dynamic Overset Grids with Application to Ship Hydrodynamics." *International Journal for Numerical Methods in Fluids* 58 (6): 591–624. doi:10.1002/fld.1758.

Hunt, Julian CR, A. A. Wray, and Parviz Moin. 1988. "Eddies, Streams, and Convergence Zones in Turbulent Flows." In *Studying Turbulence Using Numerical Simulation Databases, 2*, 1:193–208.

International Electrotechnical Committee. 2005. "IEC 61400-1: Wind Turbines Part 1: Design Requirements." *International Electrotechnical Commission*.

Ivanell, S., J. N. Sørensen, and D. Henningson. 2007. *Numerical Computations of Wind Turbine Wakes*. Springer.

Johansen, J., N. N. Sørensen, J. A. Michelsen, and S. Schreck. 2002. "Detached-Eddy Simulation of Flow around the NREL Phase VI Blade." *Wind Energy* 5 (2-3): 185–97.

Jonkman, J. M. 2010. "Definition of the Floating System for Phase IV of OC3." Technical Report NREL/TP-500-47535. National Renewable Energy Laboratory.

Jonkman, J. M., and M. L. Buhl Jr. 2005. "FAST User's Guide." Technical Report NREL/EL-500-29798. Golden, Colorado: National Renewable Energy Laboratory.

Jonkman, J. M., S. Butterfield, W. Musial, and G. Scott. 2009. "Definition of a 5-MW Reference Wind Turbine for Offshore System Development." Technical Report NREL/TP-500-38060. National Renewable Energy Laboratory.

Jonkman, J., and W. Musial. 2010. "Offshore Code Comparison Collaboration (OC3) for IEA Task 23 Offshore Wind Technology and Deployment." *Contract* 303: 275–3000.

Klein, M., A. Sadiki, and J. Janicka. 2003. "A Digital Filter Based Generation of Inflow Data for Spatially Developing Direct Numerical or Large Eddy Simulations." *Journal of Computational Physics* 186 (2): 652–65.

Laino, D. J., A. C. Hansen, and J. E. Minnema. 2002. "Validation of the AeroDyn Subroutines Using NREL Unsteady Aerodynamics Experiment Data." *Wind Energy* 5 (2-3): 227–44. doi:10.1002/we.69.

Landahl, Marten T., and Valter JE Stark. 1968. "Numerical Lifting-Surface Theory-Problems and Progress." *AIAA Journal* 6 (11): 2049–60.

Larsen, T. J. 2013. "Turbulence for the IEA Annex 30 OC4 Project." Technical Report Risø-I-3206(EN). Risø DTU.

Larsen, T. J., H. A. Madsen, A. M. Hansen, and K. Thomsen. 2005. "Investigations of Stability Effects of an Offshore Wind Turbine Using the New Aeroelastic Code HAWC2." In *Proceedings of Copenhagen Offshore Wind 2005, Copenhagen, Denmark*, 25–28.

Launder, B. E., and D. B. Spalding. 1974. "The Numerical Computation of Turbulent Flows." *Computer Methods in Applied Mechanics and Engineering* 3 (2): 269–89.

Lee, Donghoon, Dewey H. Hodges, and Mayuresh J. Patil. 2002. "Multi-Flexible-Body Dynamic Analysis of Horizontal Axis Wind Turbines." *Wind Energy* 5 (4): 281–300. doi:10.1002/we.66.

Leishman, J. G., and T. S. Beddoes. 1989. "A Semi-Empirical Model for Dynamic Stall." *Journal of the American Helicopter Society* 34 (3): 3–17.

Lindenburg, C, and JG Schepers. 1996. "PHATAS-III: Aeroelastic Modelling." ECN-C96-025. Petten.

Link, H., W. LaCava, J. Van Dam, B. McNiff, S. Sheng, R. Wallen, M. McDade, S. Lambert, S. Butterfield, and F. Oyague. 2011. "Gearbox Reliability Collaborative Project Report: Findings from Phase 1 and Phase 2 Testing." Technical Report NREL/TP-5000-51885. National Renewable Energy Laboratory.

LMS International. 2013. "Virtual.Lab Online Help Manual."

Mann, J. 1994. "The Spatial Structure of Neutral Atmospheric Surface-Layer Turbulence." *Journal of Fluid Mechanics* 273 (1): 141–68.

Mann, J. 1998. "Wind Field Simulation." *Probabilistic Engineering Mechanics* 13 (4): 269–82.

Marple Jr, S. Lawrence. 1987. "Digital Spectral Analysis with Applications." *Englewood Cliffs, NJ, Prentice-Hall, Inc., 1987, 512 P.* 1.

Menter, F. R. 1994. "Two-Equation Eddy-Viscosity Turbulence Models for Engineering Applications." *AIAA Journal* 32 (8): 1598–1605. doi:10.2514/3.12149.

Mikkelsen, R. 2003. "Actuator Disc Methods Applied to Wind Turbines." Doctoral dissertation, Technical University of Denmark.

Noack, R. W. 2005. "SUGGAR: A General Capability for Moving Body Overset Grid Assembly." In American Institute of Aeronautics and Astronautics. doi:10.2514/6.2005-5117.

Øye, S. 1996. "FLEX4. Simulation of Wind Turbine Dynamics." Technical Report NEI-DK 2426; CONF-9604166. Danmarks Tekniske Univ., Lyngby, Denmark.

Passon, P., M. Kühn, S. Butterfield, J. Jonkman, T. Camp, and T. J. Larsen. 2007. "OC3—Benchmark Exercise of Aero-Elastic Offshore Wind Turbine Codes." *Journal of Physics: Conference Series* 75 (July): 012071. doi:10.1088/1742-6596/75/1/012071.

Petersen, J. T. 1996. "The Aeroelastic Code HAWC-Model and Comparisons." Technical Report NEI-DK 2426; CONF-9604166. Danmarks Tekniske Univ., Lyngby, Denmark.

Pfeiffer, F. 1996. *Multibody Dynamics with Unilateral Contacts*. Vol. 9. John Wiley & Sons.

Pope, Stephen B. 2000. *Turbulent Flows*. Cambridge university press.

Popko, W., F. Vorpahl, A. Zuga, M. Kohlmeier, J. Jonkman, A. Robertson, T. J. Larsen, A. Yde, K. Saetertro, and Knut M. Okstad. 2012. "Offshore Code Comparison Collaboration Continuation (OC4), Phase I-Results of Coupled Simulations of an Offshore Wind Turbine with Jacket Support Structure." In *22nd International Society of Offshore and Polar Engineers Conference. Rhodes, Greece*.

Potsdam, M. A., and D. J. Mavriplis. 2009. "Unstructured Mesh CFD Aerodynamic Analysis of the NREL Phase VI Rotor." In *47th AIAA Aerospace Sciences Meeting*.

Prescott, W. C. 1999. "Numerical Integration Technique for Multi-Body Dynamic System Software." In *Symposium on International Automotive Technology, Pune*.

Preuss, Robert D., Emil O. Suciu, and Luigi Morino. 1980. "Unsteady Potential Aerodynamics of Rotors with Applications to Horizontal-Axis Windmills." *AIAA Journal* 18 (4): 385–93.

Schepers, J. G., J. J. Heijdra, D. Foussekis, S. Øye, R. Rawlinson Smith, M. Belessis, K. Thomsen, T. Larsen, I. Kraan, and B. Visser. 2002. "Verification of European Wind Turbine Design Codes, VEWTDC: Final Report." Netherlands Energy Research Foundation ECN.

Schreck, Scott. 2002. "The NREL Full-Scale Wind Tunnel Experiment Introduction to the Special Issue." *Wind Energy* 5 (2-3): 77–84.

Sezer-Uzol, Nilay, and Lyle N. Long. 2006. "3-D Time-Accurate CFD Simulations of Wind Turbine Rotor Flow Fields." *AIAA Paper* 394: 2006.

Shampine, Lawrence F., and Marilyn Kay Gordon. 1975. *Computer Solution of Ordinary Differential Equations: The Initial Value Problem*. Vol. 1. Freeman San Francisco.

Shen, W., R. Mikkelsen, J. N. Sørensen, and C. Bak. 2005. "Tip Loss Corrections for Wind Turbine Computations." *Wind Energy* 8 (4): 457–75.

Shen, W., J. N. Sørensen, and J. Zhang. 2007. "Actuator Surface Model for Wind Turbine Flow Computations." In *2007 European Wind Energy Conference and Exhibition*.

Shen, W., J. Zhang, and J. N. Sørensen. 2009. "The Actuator Surface Model: A New Navier-Stokes Based Model for Rotor Computations." *Journal of Solar Energy Engineering* 131 (1).

Shur, Mikhail L., Philippe R. Spalart, Mikhail Kh Strelets, and Andrey K. Travin. 2008. "A Hybrid RANS-LES Approach with Delayed-DES and Wall-Modelled LES Capabilities." *International Journal of Heat and Fluid Flow* 29 (6): 1638–49.

Simms, David A., S. Schreck, M. Hand, and L. J. Fingersh. 2001. "NREL Unsteady Aerodynamics Experiment in the NASA-Ames Wind Tunnel: A Comparison of Predictions to Measurements." Technical Report NREL/TP-500-29494. National Renewable Energy Laboratory.

Smirnov, A., S. Shi, and I. Celik. 2001. "Random Flow Generation Technique for Large Eddy Simulations and Particle-Dynamics Modeling." *Transactions of the ASME-I-Journal of Fluids Engineering* 123 (2): 359–71.

Snel, H., and J. G. Schepers. 1993. *Investigation and Modelling of Dynamic Inflow Effects*. Netherlands Energy Research Foundation ECN.

Sørensen, J. N., R. Mikkelsen, and N. Troldborg. 2007. "Simulation and Modelling of Turbulence in Wind Farms." *Proceedings EWEC 2007*.

Sørensen, J. N., and W. Shen. 2002. "Numerical Modeling of Wind Turbine Wakes." *Journal of Fluids Engineering* 124 (2): 393. doi:10.1115/1.1471361.

Sørensen, J. N., W. Shen, and X. Munduate. 1998. "Analysis of Wake States by a Full-Field Actuator Disc Model." *Wind Energy* 1 (2): 73–88.

Sørensen, N. N., J. A. Michelsen, and S. Schreck. 2002. "Navier–Stokes Predictions of the NREL Phase VI Rotor in the NASA Ames 80 Ft × 120 Ft Wind Tunnel." *Wind Energy* 5 (2-3): 151–69.

Spinato, F., P. J. Tavner, G. J. W. van Bussel, and E. Koutoulakos. 2009. "Reliability of Wind Turbine Subassemblies." *IET Renewable Power Generation* 3(4): 387-401.

Thompson, Joe F., Zahir UA Warsi, and C. Wayne Mastin. 1985. *Numerical Grid Generation: Foundations and Applications*. Vol. 38. North-holland Amsterdam.

Troldborg, N., J. N. Sørensen, and R. Mikkelsen. 2007. "Actuator Line Simulation of Wake of Wind Turbine Operating in Turbulent Inflow." *Journal of Physics: Conference Series* 75 (July): 012063. doi:10.1088/1742-6596/75/1/012063.

Veers, Paul S. 1988. "Three-Dimensional Wind Simulation." Technical Report No. SAND-88-0152C; CONF-890102-9. Sandia National Labs, Albuquerque, NM.

Whale, J., C. J. Fisichella, and M. S. Selig. 1999. "Correcting Inflow Measurements from HAWTs Using a Lifting-Surface Code." *Urbana* 51: 61801.